Phase Transformations and Entropy of Non-Equilibrium Materials

Thesis by

Hillary L. Smith

In Partial Fulfillment of the Requirements

for the Degree of

Doctor of Philosophy

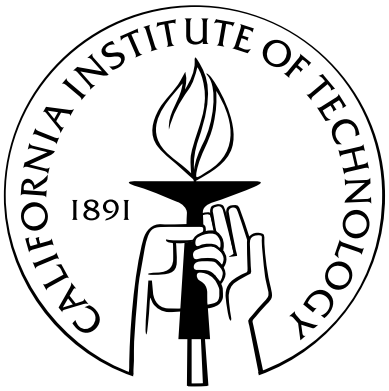

California Institute of Technology

Pasadena, California

2014

(Defended May 29, 2014)

To my parents

Abstract

The importance of vibrational entropy to solid-state phase transformations has become well established over the past decade. Considerable experimental and theoretical work has gone into investigating the vibrational entropy of phase transformations in metallic alloys. This thesis examines phase transitions in three unique systems, unified in the experimental tools used to probe the nature of these transitions.

Time-resolved vibrational spectra through the glass transition in the bulk metallic glass CuZr were acquired with inelastic neutron scattering. Vibrational density of states (DOS) in ranges as small as 4K were extracted from continuous heating through the glass transition. For each temperature interval, the vibrational entropy is calculated from the DOS. This provides a detailed characterization of how the vibrational entropy contributes to the large jump in heat capacity that characterizes the glass transition in amorphous materials. This change in heat capacity has been attributed to combinations of configurational and vibrational entropy. However, the role of vibrational entropy in this transition has never been demonstrated for all vibrational modes in an amorphous material. This work provides the first experimental measurement of the change in vibrational entropy through the glass transition. We find the unique contributions of both the vibrational and configurational entropy, and find that the change in vibrational entropy can be bound at less than 0.01 k_{B} per atom. By elimination, this means that the configurational entropy is dominant, putting to rest a controversial debate over the role of entropy through the glass transition.

The changes in vibrational entropy during the early stages of chemical unmixing were studied in a nanocrystalline fcc solid solution of 6%-Fe in Cu. Material prepared by high-energy ball milling was annealed at temperatures from 200 to 360°C to induce chemical unmixing. Nuclear resonant

inelastic x-ray scattering spectra yield the phonon partial density of states (pDOS) of ^{57}Fe. The pDOS of the as-prepared material is that of an fcc crystal. In the earliest stages of unmixing, the features of the pDOS broaden, with only small changes in average phonon frequencies, until the bcc phase begins to form. The chemical state of the material was characterized by three-dimensional atom probe microscopy, Mössbauer spectrometry, and x-ray powder diffractometry. The unmixing was heterogeneous, with iron atoms forming iron-rich zones that thicken with further annealing. The vibrational entropy calculated from the pDOS underwent little change during the early stage of unmixing, but decreased rapidly when the bcc phase formed in the material.

Electrochemical cycling of lithium ion batteries causes fundamental structural changes and the formation of new phases in cathode materials. The reversibility of these transitions is often critical to the viability of cathode materials for long-term performance. The cycle lives for cathodes of nanocrystalline iron trifluoride (FeF_3) were measured in rechargeable lithium batteries at different depths of discharge. When the discharge was limited to less than one Li^+ ion per FeF_3, both the cycle life and energy efficiency were considerably greater than when converting FeF_3 into Fe and LiF in deep discharge. An in situ X-ray diffractometry (XRD) study of the FeF_3 cathode during its initial discharge to $LiFeF_3$ showed a continuous change of the FeF_3 diffraction pattern, indicating Li^+ insertion into the rhombohedral FeF_3 causing distortion of its lattice parameters. Electrochemical cycling is most reversible when this mechanism occurs in the absence of other changes in the crystal structure.

Acknowledgements

I would like to express my gratitude to my advisor, Professor Brent Fultz. I am indebted to his patience, motivation, and immense knowledge for making me into a scientist. When I have the opportunity to mentor my own students, I will pay him the greatest compliment by passing along many of the things that he has taught me to a new generation of scientists.

My thesis committee members deserve my appreciation and acknowledgement. Bill Johnson and Marios Demetriou introduced me to metallic glasses and were always available for helpful conversation and practical advice. Julia Greer and Jennifer Jackson provided insightful comments on all of my thesis work. Caltech scientists Channing Ahn and Jiao Lin played important roles: Channing Ahn introduced me to many experimental tools and provided continued good humor in my endeavors. Jiao Lin made possible the neutron simulation work and shared his considerable computational knowledge.

The work presented here would not have been possible without the generous support of my fellow Caltech students. Chen Li guided my introduction to inelastic neutron scattering and served as a mentor, Lisa Mauger showed me the ropes in the Fultz group and was a valued consultant, and Hongjin Tan passed along his considerable electrochemical expertise and a working Mössbauer spectrometer. Dennis Kim supported me as a beamtime partner, Matt Lucas provided mentorship, and Sally Tracy shared her experimental expertise. Many other students generously provided their support including David Abrecht, Olivier Delaire, Connie Hsueh, Laura Kim, Tian Lan, Max Murialdo, Jorge Munoz, Nick Parker, Justin Purewal, Nick Stadie, and Mike Winterrose. Bill Johnson's graduate students including Glenn Garrett, Andrew Hoff, Georg Kaltenboeck, Scott Roberts, and Joseph Schramm made this work possible through their kind sharing of knowledge and equipment.

Pam Albertson deserves recognition for her constant encouragement; Mike Vondrus for his help and kind words.

My graduate work relied on the support of many experts outside of Caltech. Thank you to Doug Abernathy, Garrett Granroth, Mark Hagen, Mark Loguillo, Bekki Mills, Jennifer Niedziela, and Matt Stone at Oak Ridge National Lab. Thank you to Chad Hornbuckle and Greg Thompson at University of Alabama, Birmingham. Thank you to Ercan Alp, Michael Hu, Jiyong Zhao, and Yuming Ziao at Argonne National Lab.

I would also like to thank those whose guidance led me to pursue my graduate studies. Jaroslaw Majewski introduced me to neutron scattering and entrusted me with his instrument to learn and make mistakes. Jarek and many others at the Lujan Center set me on the path towards neutron science including Jim Browning, Alan Hurd, Anna Llobet, and Thomas Proffen. Dvora Perahia offers her continued mentorship.

My undergraduate mentors Peter Beckmann, Michelle Francl, Jonas Goldsmith, Elizabeth McCormack, Karen Tidmarsh, and many wonderful professors at Bryn Mawr College supported my interests and fortified my passion for science with confidence and fearlessness.

My family is a constant source of love and support. My parents, Roger and Debbie, laid the strongest possible foundation for my success. My brother and sister, Mitchell and Robin, are always there to cheer me on and help me keep perspective. My husband, Derek, is my cherished partner and I am deeply grateful for his love and support.

Contents

List of Figures

Part 1: Experimental Techniques

Chapter 1

Inelastic Neutron Scattering

1.1 Introduction

Inelastic neutron scattering is a powerful tool for studying the atomic and molecular motions in materials. Scattering experiments can provide the phonon density of states, a key function in understanding the vibrational properties of materials including thermal expansion, heat capacity, thermal conductivity and vibrational entropy. This section provides a short overview of neutron scattering and the basic tools and concepts necessary to interpret phonon densities of states acquired on a time-of-flight direct geometry chopper spectrometer. There are many accounts of neutron scattering theory and experiments that provide the details not covered here. Pynn's short illustrated primer gives a broad overview to neutron scattering, experiments, and instrumentation[1]. Books by Squires[8] and Fultz[3] give in-depth accounts of neutron scattering theory. Presentations and slides from annual neutron schools are also excellent introductory resources available on the web.

1.2 Neutrons and the Nobel Prize

Neutrons are baryons with no charge, so they penetrate deeply into most materials. This makes it possible to probe bulk properties with neutrons. The neutron wavelength, calculated from its mass, is 1.8 Å for thermal neutrons, which is on the order of the interatomic spacing in many materials. Changing the temperature of the neutrons provides access to an energy spectrum from 0.1 meV to 100 meV, so a wavelength range can be selected to suit the measurement technique.

Neutrons have a magnetic moment of -1.913 μN. This allows them to interact with the unpaired electrons of magnetic atoms, providing information about the magnetic structure and spin dynamics of magnetic materials. Using polarized neutrons can enhance the information acquired. Neutrons from reactor and spallation sources are unpolarized, but neutrons can be polarized relatively easily. Doing so, however, considerably limits the available flux of the polarized neutron beams, necessitating large samples for reasonable measurement times.

Unlike x-rays, neutrons can penetrate matter far better than charged particles, and neutrons interact with atoms via nuclear forces rather than electrical forces. However, neutrons scatter only weakly once they penetrate the sample, and detection of an uncharged particle is more complicated than detecting a charged particle. Available fluxes at neutron sources are usually lower than x-ray fluxes, causing neutron scattering to sometimes be considered a "signal-limited technique." The brilliance of available x-ray sources at synchrotron radiation facilities is on the order of 10^{18} photons per second per mm^2. Even the brightest neutron source trails by fourteen orders of magnitude, producing 10^4 neutrons per second per mm^2. However, unlike the scattering power from x-rays, which scales with the number of electrons, neutron scattering power has no direct correlation to the size of the nucleus. This allows neutrons to probe elements such as H and Li, which are virtually invisible to x-rays. The neutron scattering cross section is discussed in greater detail in Sec. 1.3.

Bertram Brockhouse and Clifford Shull were awarded the Nobel Prize in Physics "for pioneering contributions to the development of neutron scattering techniques for condensed matter studies [9]." The end of the second World War gave researchers access to nuclear reactors capable of delivering enough neutron flux for elastic and inelastic scattering experiments. Working at Oak Ridge National Lab in the US, Shull developed neutron scattering techniques for diffraction of elastically scattered neutrons. Shull monochromatised neutrons from the reactor source by using the Bragg condition to select neutrons reflected in a certain direction with a specific wavelength. The neutrons that are incident on the sample with a given energy, and leave with the same energy, are elastically scattered. By counting the neutrons at a range of angles with a rotatable detector, he was able to obtain a diffraction pattern that gives the relative positions of atoms in the sample.

At the same time, Brockhouse worked at the Chalk River reactor in Canada on inelastic scattering, designing a triple-axis spectrometer for studying the energy spectrum of scattered neutrons. The principle of the triple-axis spectrometer is that the monochromatized neutrons can be turned about an axis and then penetrate the sample, which rotates on the second axis, at which point they are detected by a detector moving on a third axis. Brockhouse configured the instrument to analyze the energy of neutrons that have either gained or lost energy to the sample. The exchange of energy with the sample excites phonons in the sample, and the analysis of the final energy at the detector can be used to map the phonon excitations in the sample.

1.3 Basic Theory

Scattering experiments are quite simple, in principle. An incident particle or wave of known properties interacts with a scattering center, and the outgoing properties are measured. When the relative phase relationship between the incident and scattered waves is preserved, the scattering is said to be coherent. Incoherent scattering occurs when the phase relationship between the incident and scattered waves is not preserved. In addition to being coherent or incoherent, all scattering is either elastic of inelastic. During elastic processes, there is no energy transfer to the scattering center, while in an inelastic process, the neutron gains or loses energy to the scattering center.

Coherent elastic scattering is required for diffraction when the phase differences between outgoing waves interfere constructively or destructively at different angles around the sample, giving Bragg diffraction peaks. Incoherent elastic scattering is also common, but instead of the sharp diffractions associated with crystalline periodicities seen in coherent elastic scattering, phase relationships are disrupted by disorder in the material, and the scattering intensity has a broad angular dependence. Incoherent inelastic scattering is used in spectroscopies measuring intensity versus energy. Of primary concern here is coherent inelastic scattering that is used to study excitations in materials such as phonons and magnons. For example, in some phonon studies, the incident particle (a neutron) loses energy when creating a photon, so the process is inelastic, but the scattering amplitude depends on the phases of the atom movements in the phonon with respect to the incident neutron, so the

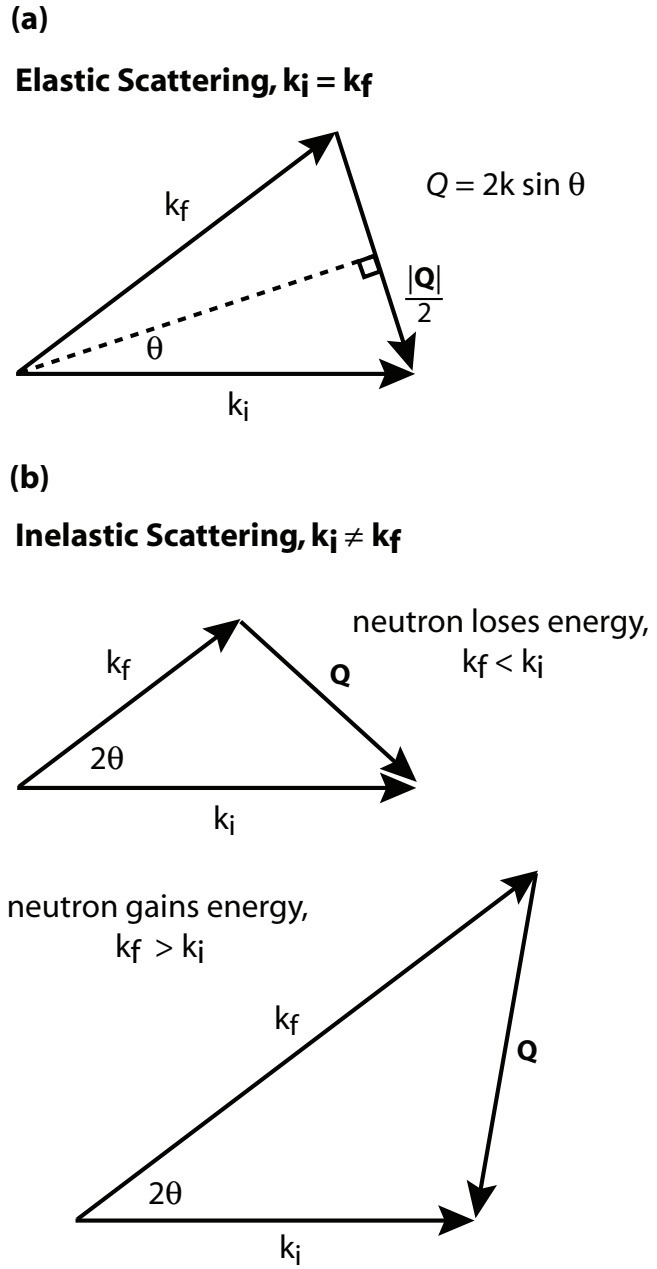

Figure 1.1: (a) Elastic scattering events have incident and outgoing wave vectors equal. (b) Inelastic scattering events conserve momentum, but the incident neutrons gain or lose energy to the sample. Adapted from [1].

process is also coherent.

A more detailed understanding of the difference between coherent and incoherent scattering can come from considering the behavior of a simple harmonic oscillator. A wave is incident on an oscillator, and the wave is then re-radiated from the oscillator. In a coherent scattering process, all of the details of how the coordinates of the oscillator will respond to the incident wave are known. In this case it is possible to know the exact relationship of the phase of outgoing wave relative to the phase of the incoming wave. In an incoherent scattering process, the oscillator is now coupled to another system within the material, such as another oscillator. If there is freedom in how the oscillator can interact with this coupled system, then different amounts of energy may be transferred between the oscillator and its coupled system. Since this process of energy transfer to the coupled system is not deterministic (it occurs via a quantum mechanical process), then the phase of the outgoing wave will differ between scattering events, depending on the amount of energy transferred.

Scattering of neutrons by matter can alter both the momentum and energy of the neutrons and matter. Of course, total momentum and energy must still be conserved, so the scattering event is governed by the scattering vector

$$\mathbf{Q} = \mathbf{k_i} - \mathbf{k_f} \tag{1.1}$$

where $\mathbf{Q}$ is the momentum transfer, $\mathbf{k_i}$ is the wave vector of incident neutrons, and $\mathbf{k_f}$ is the wave vector of scattered neutrons. Fig. 1.1 shows the two types of scattering processes. Elastic scattering in Fig. 1.1(a) can occur for a rigidly fixed nucleus in which the neutron is deflected during the scattering event through the angle 2θ, but does not gain or lose energy so $\mathbf{k_i}$=$\mathbf{k_f}$. Trigonometery thus gives the relation

$$Q = 2\,k\,\sin\,\theta = \frac{4\,\pi\,\sin\,\theta}{\lambda} \tag{1.2}$$

Table 1.1: Coherent and incoherent neutron scattering cross section for some notable elements. Values are in units of barns, where 1 barn $= 10^{-24}$ cm^2.

Nuclide	σ_{coh}	σ_{inc}
^{1}H	1.8	80.2
^{2}H	5.6	2.0
C	5.6	0.0
O	4.2	0.0
Al	1.5	0.0
Nb	6.3	0.0
V	.02	5.0
^{14}N	11.01	0.5
^{15}N	5.21	~ 0.0
Cu	7.5	0.5
^{36}Ar	24.9	0.0

because the neutron wave vector $\mathbf{k}$ has magnitude $k{=}2\pi/\lambda$.

Figure 1.1(b) depicts inelastic scattering events that occur when a nucleus recoils during collision with a neutron or is in motion when the neutron arrives, imparting or absorbing energy. In inelastic scattering events $\mathbf{k_i} \neq \mathbf{k_f}$, but Eq. 1.1 still holds. If $\mathbf{k_i} > \mathbf{k_f}$, then the neutron loses energy to the sample, and if $\mathbf{k_i} < \mathbf{k_f}$, the neutron gains energy.

Neutron scattering power varies from element to element and isotope to isotope in a seemingly random way. The scattering cross section σ is an area related to the probability that a neutron will interact with a nucleus in a particular way; that is, by either scattering or absorption. In effect, the scattering cross section is equivalent to the effective area presented by the nucleus to the incoming neutron. The scattering cross section is different for coherent scattering and incoherent scattering because the fundamental interaction between incoming wave and the nucleus is different. There is also variation in scattering cross section by isotope because the neutrons are interacting with the atom nucleus, and therefore, different numbers of neutrons in the nucleus change the effective area of the nucleus.

Table 1.1 gives values for a handful of notable elements and isotopes in units of barns (1

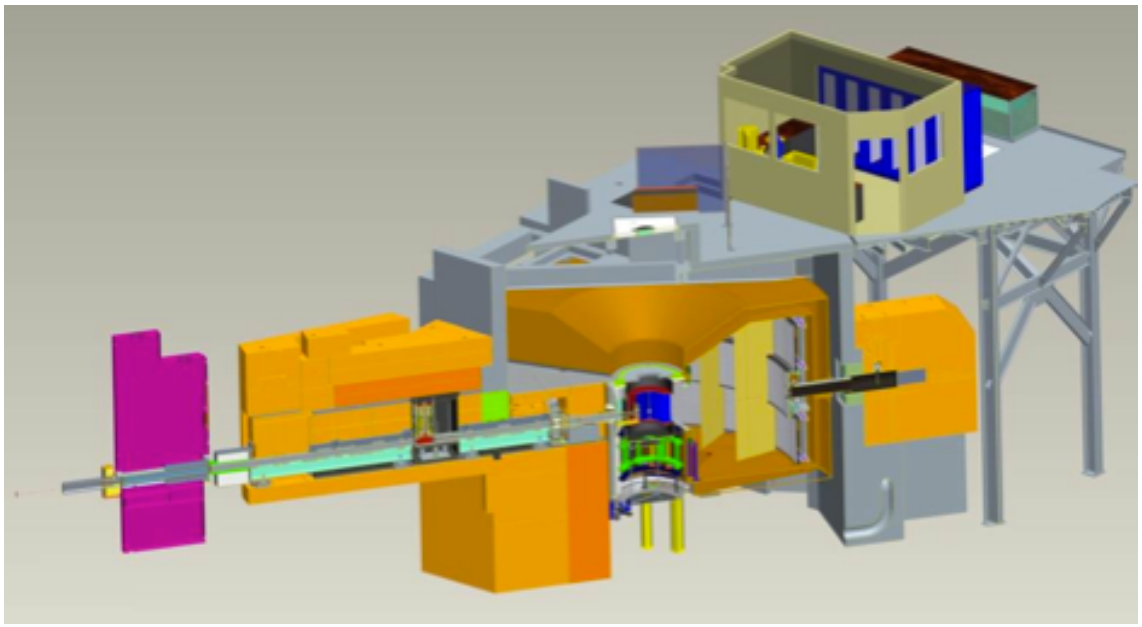

Figure 1.2: Schematic of the Wide Angular-Range Chopper Spectrometer (ARCS) at the Spallation Neutron Source (SNS).

barn $= 10^{-24}$ cm^2). In cases where two isotopes of the same element have very different scattering cross sections, there are opportunities to use isotopic enrichment to change or enhance scattering from a particular element. Hydrogen and deuterium are a common pair for contrast variation studies in soft matter experiments, because hydrogen has an incoherent scattering cross section more than an order of magnitude greater than deuterium. Aluminum has a small coherent cross section and does not scatter incoherently, so it is a common choice for windows and sample environment components. When higher temperatures are necessary, niobium is also chosen for this purpose, although it has a slightly larger coherent scattering cross section than aluminum. Vanadium has virtually no coherent scattering, and is a typical choice for sample containers in diffraction experiments because it will give no Bragg peaks. Vanadium is also useful for calibration of instrument energy resolution. The National Institute of Standards maintains a web interface for thermal neutron cross sections where these values were obtained [10].

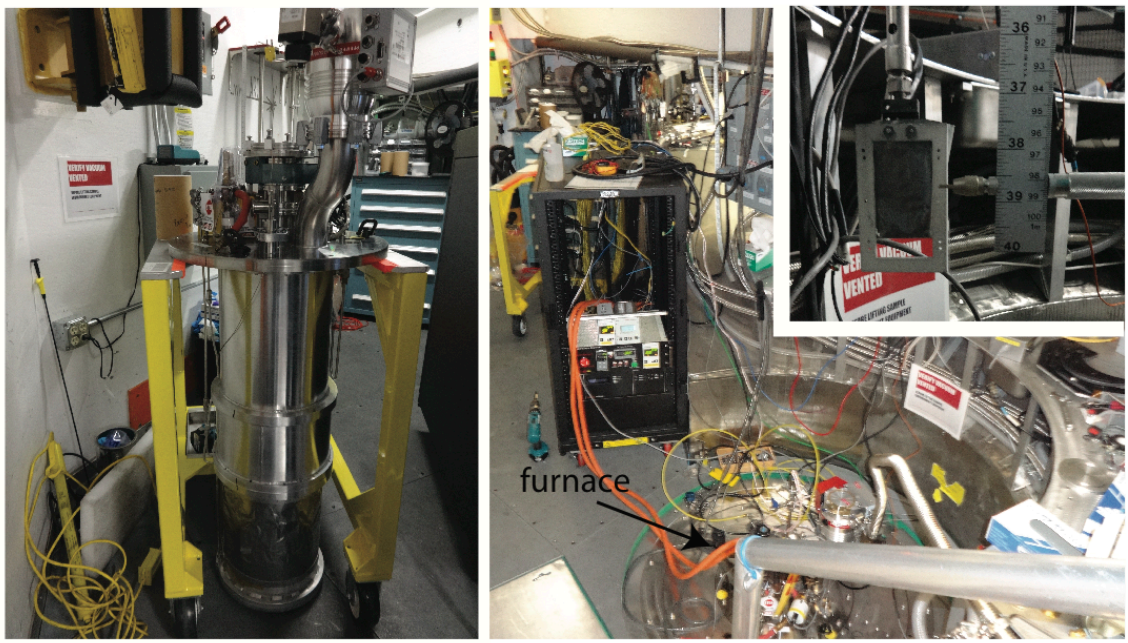

Figure 1.3: (Left) High-temperature radiative vacuum furnace employed for measurements up to 1500K. (Right) The furnace in place inside the ARCS sample chamber, with connections for heating and water cooling emerging from the top of the furnace. The inset shows a powder sample mounted and ready for insertion into the top-loading furnace.

1.4 Wide Angular-Range Chopper Spectrometer

The Wide Angular-Range Chopper Spectrometer (ARCS) at the Spallation Neutron Source (SNS) at the Oak Ridge National Lab was used for all inelastic neutron scattering results presented here. ARCS is a time-of-flight direct geometry chopper spectrometer located on an ambient water moderator to provide incident neutrons in the energy range 20 to 1500 meV. The moderator to sample distance of 13.6 m is among the shortest of instruments at the SNS, providing ARCS with a large neutron flux and yielding an energy resolution of 2-5%. The sample-to-detector distance is between 3 and 3.4 m, and the angular detector coverage for which ARCS gets its name is -28 to 135°. Three banks of detectors give a vertical coverage of -27 to 26°. A schematic of the ARCS instrument is given in Fig. 1.2.

Each neutron pulse leaves the moderator at a known time. Neutrons pass through two choppers, which are fast-rotating cylinders with slits that can be adjusted to allow neutrons to pass through

in desired timing sequences. The T0 chopper is timed to block gamma-rays and fast neutrons that were not sufficiently slowed by the moderator. The Fermi chopper allows only a particular neutron energy to pass, selected by its rotation speed. The two-chopper design is a commonly used method to block slow neutrons that linger from the preceding proton pulse and confuse the precise timing of neutrons traversing from the moderator to the sample and into the detector. It also allows better energy resolution by having multiple rotations of the Fermi chopper for each proton pulse. Once the neutrons reach the sample chamber, the majority will pass through the sample unscattered and be absorbed by a beam stop. Neutrons that scatter from the sample will have their arrival time and position precisely recorded by the detector array. The detector array is three banks of detector tubes covering 28° to the incident neutron in one horizontal direction, and 135° in the other horizontal direction. Detector tubes are filled with ^{3}He that reacts with the arriving neutron to form tritium and protium, which are detected by creating a charge cloud at the exact location of the neutron event. Fig. 1.4 shows a photo of the detector array viewed from inside the instrument, and a histogram of data on the detector tubes. The square in the middle detector bank is a blank spot with no detectors where the direct beam passes into the beam stop [2].

The final energies and wave vectors of the scattered neutrons are thus determined from the equation

$$E_f = \frac{m_n}{2}\frac{L^2}{\tau^2} \tag{1.3}$$

where the final energy of the neutron E_f is known in addition to the initial neutron energy when the distance L from the sample to the detector and arrival time τ of the neutron is recorded for a neutron of mass m_n. Here τ=0 for elastic scattering.

In standard data-collection mode, neutrons reaching a particular detector pixel at a given time are binned into histograms over a time period of the experimenter's choosing. The SNS has modernized this data collection method, and now records the exact time, position, and energy of every neutron

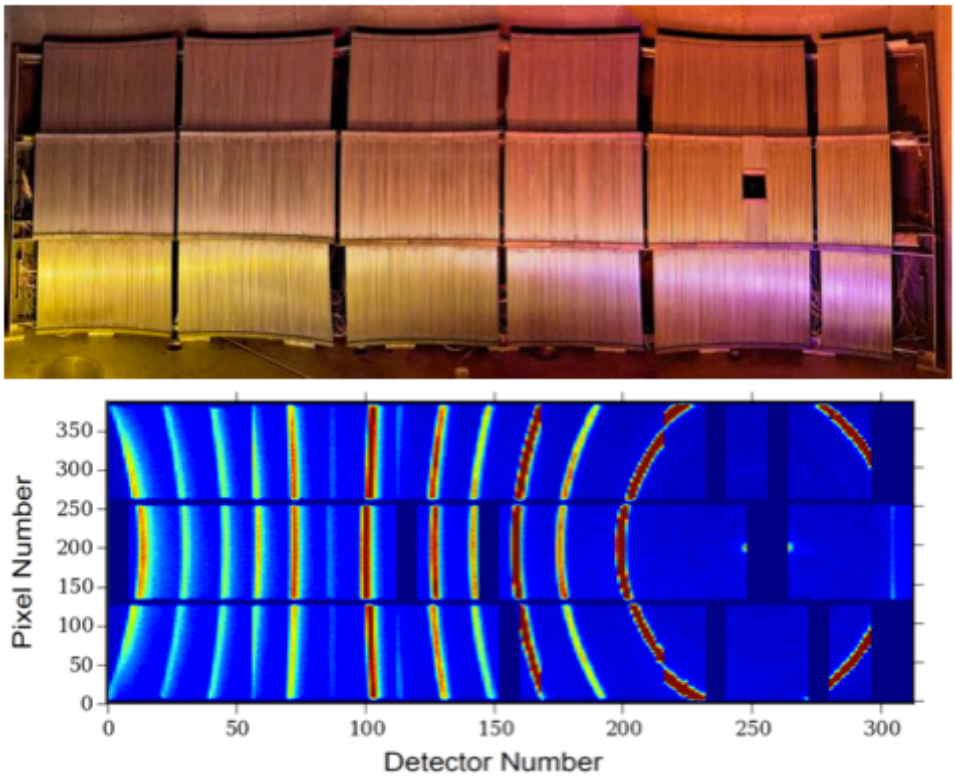

Figure 1.4: (Top) Panoramic view of the detector banks at ARCS, viewed from inside the detector tank. (Bottom) Data histogrammed onto the detector tubes. The square in the middle detector bank is a blank spot with no detectors where the direct beam passes into the beam stop. Reproduced from [2]

.

individually. This data acquisition method, referred to as 'event-mode' data collection requires significantly more hard-drive space for data collection, but provides the experimenter with the flexibility to bin data post-measurement[1]. These capabilities were exploited in the measurement of phonon DOS through the glass transition in CuZr. The significant advantages provided by event-mode data collection are discussed in Chapter 5.

Sample environments currently available on ARCS provide a large range of accessible temperatures. Fig. 1.3 depicts one sample environment: a radiative vacuum furnace referred to as the MICAS furnace, which is capable of measurements up to 1900K[2]. The portion of the MICAS furnace that is in the neutron beam is made entirely of Nb. This is the lowest part of the furnace, shown covered in foil in the left photo in Fig. 1.3. The furnace is lowered into the sample space with a crane, and the sample is loaded into the chamber on a stick from the top. The photo inset shows a powder sample prepared in a Nb foil packet, attached to the sample stick. It is aligned in a BN neutron-absorbing frame, ready for insertion in the sample environment at the precise height for incident neutrons.

The addition of a radial collimator to the ARCS instrument has made a significant improvement in reducing the unwanted scattering intensity from complicated sample environments. The collimator is located inside the sample space at a radial distance of ∼40 cm from the sample, and consists of radially-oriented septa made of a neutron-absorbing material. By geometrically defining the beam with absorbing material, the collimator reduces beam divergence. The collimator oscillates slowly during the measurement to average over the effect of shadowing by the finite thickness of the collimator blades. Fig. 1.5 shows the collimator as viewed from above the sample space, as a sample would see the collimator. The furnace fits inside this sample space.

The impact of the collimator on the background scattering intensity is shown in Fig. 1.6. The empty furnace was measured with and without the collimator for an identical amount of proton charge. The $S(Q,E)$ plots in Fig. 1.6 have the same intensity scale and demonstrate the remarkable decrease in coherent elastic scattering from the sample environment as well as a virtual elimination

[1] In our typical 5-6 days of data collection, we acquire 70-90 GB of data.

[2] Measurements by our group have been performed up to 1500K, and this may be close to a limit for use on ARCS because of concerns about the outer furnace jacket reaching temperatures of 600K during *ex situ* testing.

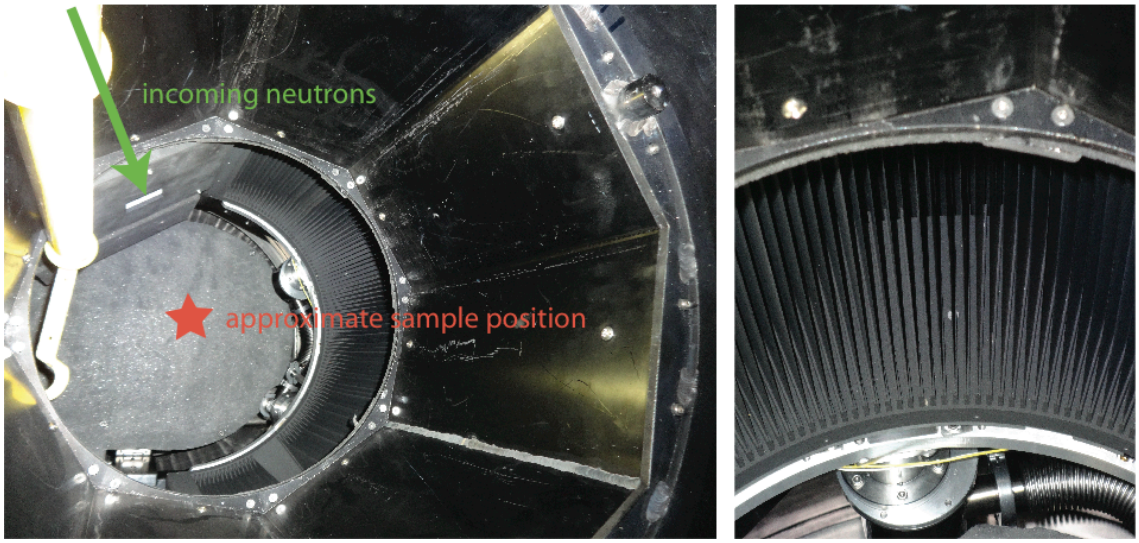

Figure 1.5: Radial collimator as viewed from above the sample space. (Left) The incoming beam port is visible in the upper left of the sample space, and the approximate position of the sample is indicated. (Right) A closer view of the thin collimator blades as the sample sees them.

of inelastic scattering. Also plotted is the scattering with and without the collimator integrated over all momentum transfers as a function of energy transfer. This indicates that the collimator suppresses the background due to the furnace by a factor of ten.

1.5 Data Reduction

To make an inelastic neutron scattering data set useful, it is necessary to follow a series of procedures to reduce the raw data and convert it into physically meaningful units of energy and momentum transfer. This "reduction" is a critical step in the path to achieving scientifically meaningful results. A theoretical description of the reduction procedure is available [3]. Practical details are best obtained from the instrument scientists at the time of an experiment, as routines change as new capabilities are added. A notable exception is the final reduction of $S(Q,E)$ to the phonon density of states. Code for this critical step, *DrChops*, is maintained at Caltech, and has yet to be incorporated into facility-maintained routines[3]. Detailed considerations for data reduction are given in a digital

[3] As of this writing, reduction to density of states is not included in facility-maintained code. It most likely will be at some point, but the author advises that this part of the process needs to be understood fully by the experimenter, more so than any other part of the data reduction process

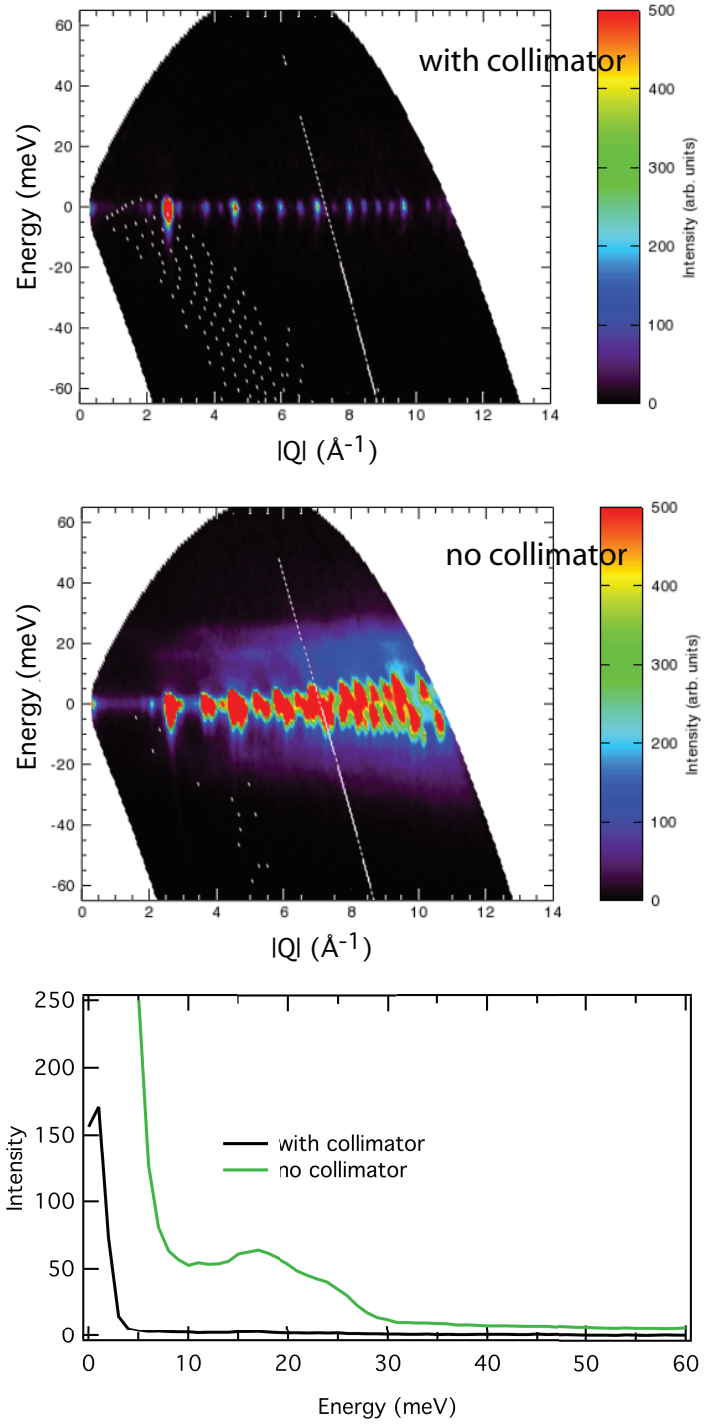

Figure 1.6: $S(Q,E)$ plots acquired under identical conditions with and without the radial collimator indicate the considerable reduction in background intensity achieved with the collimator. The integrated intensity summed over Q and plotted as a function of energy shows quantitatively the approximate ten-times reduction in background intensity.

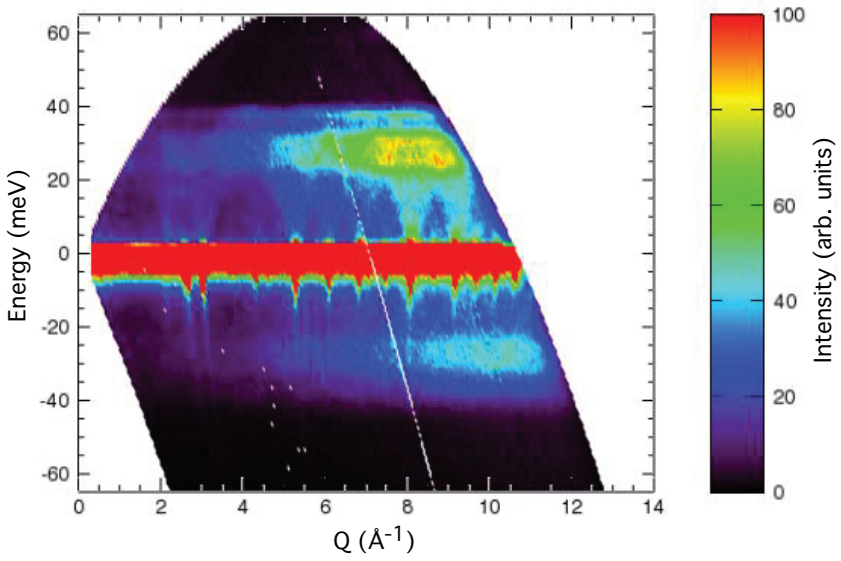

Figure 1.7: $S(Q,E)$ plots are a translation of the raw data into energy as a function of momentum transfer over the range in scattering angle of the instrument.

book by Fultz et al. [3]. Particular aspects of the *DrChops* code are also available [11]. A brief description of the reduction to phonon density of states (DOS) is given here.

Initial reduction converts raw data into a plot of $S(Q,E)$, such as the one shown in Fig. 1.7 for chromium powder measured at room temperature. Positive energy corresponds to phonon creation, negative energy to phonon annihilation. Phonon annihilation is typically disregarded in the final reduction to DOS because its energy resolution is poor. The detectors at different scattering angles ϕ provide energy spectra $S_\phi(E)$, where Q varies with E across the spectrum. For a particular incident energy E_i and scattering angle ϕ, the relation between maximum momentum transfer Q and energy transfer is

$$Q = 0.6947\sqrt{2\,E_i - E - 2\sqrt{E_i\,(E_i - E)}\,\cos\,\phi} \tag{1.4}$$

in which Q is in Å^{-1}, and energy is in meV. This establishes the kinematic limit for a given scattering angle. Fig. 1.8 shows the kinematic limit for several values of scattering angle spanning the

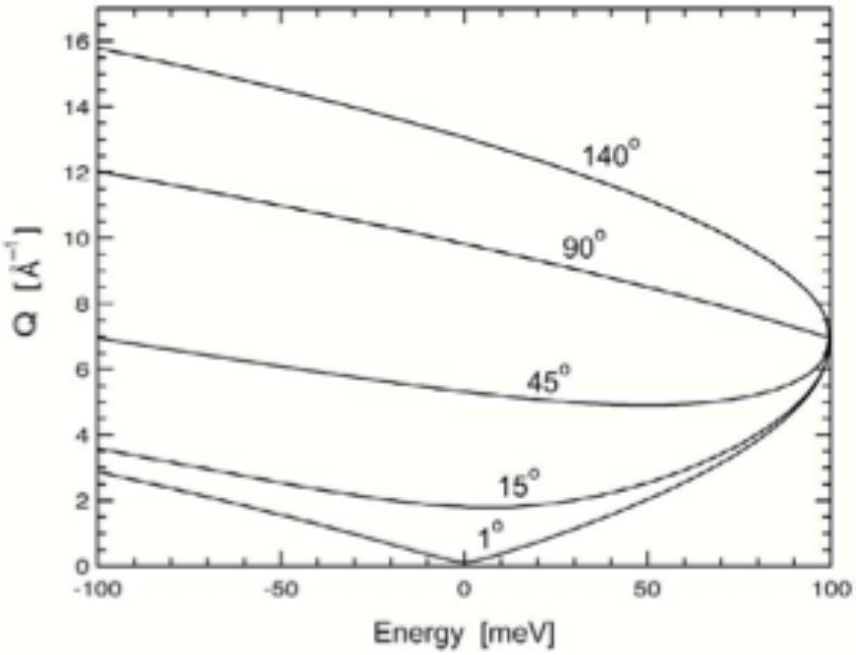

Figure 1.8: Kinematic limit calculated using Eqn. 1.4 for five values of scattering angle ϕ with an incident energy $E_i = 100$ meV. From [3].

approximate coverage of ARCS for an $E_i = 100$ meV calculated using Eqn. 1.4. To obtain high-quality phonon spectra, it is important to optimize the choice of incident energy and maximum momentum transfer for a particular sample. Using higher incident energies or measuring phonons at larger scattering angles gives large momentum transfer, but degrades the energy resolution. Also, at high momentum transfer, contributions from multiphonon scattering and multiple scattering are greater, making it more difficult to extract a one-phonon DOS.

Scattering experiments on ARCS provide not only inelastically scattered neutrons, but elastically scattered neutrons as well. This is visible as the high-intensity region around 0 meV in Fig. 1.7. Diffraction patterns of reasonable quality can be obtained by summing over a narrow energy range around 0 meV. This is very useful as an *in situ* check of the phase of the material. ARCS performs so well as an elastic scattering instrument that reduction procedures are being developed by instrument scientists to extract pair distribution functions from ARCS data. For the data reduction to a phonon DOS, however, the elastic peak is disregarded, and must be removed below a certain energy transfer and replaced by a function of energy determined from the inelastic scattering just past the elastic

peak [11]. This procedure renders information below a certain energy transfer, typically 4-5 meV, unreliable.

Multiphonon and multiple scattering corrections must next be performed to reduce the integrated intensity to the one-phonon DOS. Multiple scattering events occur when one neutron is scattered multiple times by the sample, sample holder, sample environment, or other instrument components. Multiphonon scattering results from the simultaneous creation or annihilation of multiple phonons by one neutron scattering event. The Fourier-log method is commonly used for multiphonon corrections and works well for instruments with a simple resolution function, as for the nuclear resonant inelastic x-ray scattering experiments described in Chapter 3, where multiple scattering events are virtually non-existent.

For the ARCS instrument, multiphonon and multiple scattering events can both make a sizable contribution to the integrated intensity, especially in experiments performed at high temperatures with considerable contributions from a sample environment. As there is no way to decouple these contributions in the experimental data, an iterative method is currently employed to perform a simultaneous correction. This approach assumes a single constant that relates the multiple scattering to the multiphonon scattering, C_{ms} [3]. The value of C_{ms} is not known *a-priori*, and instead, a series of phonon DOS is generated from a list of possible values. These DOSs, along with the result of a minimizing penalty function constructed to choose the DOS that produced the 'best' $S(E)$, are presented to the experimenter. A selection is made, typically to maintain a consistent C_{ms} value over a range of temperatures; the validity of this selection criteria is discussed in Appendix A.

For samples made of multiple chemical elements, different scattering cross sections of these elements give different weight to these atoms in the experimental intensities. The modes corresponding to the vibrational amplitudes of some of the elements are overemphasized, while the others are underemphasized. In this sense, the measured phonon density of states should be called a"neutron-weighted phonon density of states." Correcting for neutron weighting to obtain a true phonon DOS requires knowledge of the phonon partial DOS from each constituent element. In some cases, this may be achieved by computation. Nuclear resonant inelastic x-ray scattering experiments may also

be performed to obtain the Fe partial DOS for alloys containing iron. This technique is discussed in Chapter 3. With this additional information, a neutron weight correction can be applied that gives the partial DOS of all constituent elements and the true total phonon DOS, normalized by each elemental scattering contribution.

1.6 Simulation of High-Temperature Sample Environment

The Virtual Neutron Facility (VNF) is a tool for the simulation of neutron scattering experiments developed during the DANSE Software Development project [3]. The two primary components of the VNF are the same as those in real scattering experiments: instrumentation and samples. The capability of VNF to successfully simulate real scattering experiments has been demonstrated for two direct geometry chopper spectrometer instruments at the SNS[12]. Lin et al. simulated scattering experiments of uranium nitride on ARCS and SEQUOIA, accurately modeling the total scattering response observed in single crystal measurements on these instruments.

Tremendous potential exists for the VNF to model complex neutron scattering spectra and elucidate contributions from different types of scattering events that cannot be extracted from experimental data. Expanding the capabilities of VNF to account for changes to the instrumentation (such as the addition of the radial collimator to ARCS) as well as introducing sample environments is the next step. Sample environments greatly complicate the scattering at the sample position, because the interaction of the sample with many additional layers of scatterers must be considered.

Simulation of the high-temperature MICAS furnace was undertaken with Jiao Lin in an attempt to model the considerable background that this sample environment provides during scattering experiments. The goal of this work is to obtain a detailed characterization of the furnace as means to sensibly identify and eliminate this contribution from measured data. Appendix A describes some of the results of this ongoing work including the basic concepts of the MCViNE simulation framework, simulations of aluminum and vanadium, the design of the high-temperature sample environment template, and a comparison of experimental and simulated chromium data in the furnace.

Chapter 2

Mössbauer spectrometery

2.1 Introduction

Mössbauer spectrometry offers a unique probe of the resonant nucleus for specific Mössbauer-active isotopes, most commonly ^{57}Fe. Quantitative information on hyperfine interactions are obtained by measuring small changes in energy between the nucleus and its neighboring electrons. Hyperfine interactions have proved a powerful tool for studying the structural, electronic, and magnetic properties of materials. This section provides a short overview of the Mössbauer effect and most of the basic tools and concepts necessary to understand the Mössbauer spectra that are presented in coming chapters. Many excellent references exist that can provide a more detailed summary [13] or a in-depth examination of the technique and its many applications [14].

2.2 Mössbauer Effect

It was presumed for many years that nuclear resonant absorption and fluorescence may be possible when radioactive nuclei decay from an excited state, emitting γ-rays that would excite other stable nuclei of the same isotope. Initial attempts to observe these resonant processes were largely unsuccessful, because energy is lost to nuclear recoil during the emission and absorption of γ-rays in a free nucleus. As a result of this nuclear recoil, the energy of the emitted gamma ray is less than the energy difference between the two nuclear levels. If resonant absorption is to occur, the energy of the incoming gamma ray needs to be greater than this energy difference. Thus, for free nuclei, the

recoil energy prevents resonant absorption of γ-rays under normal circumstances.

In 1957, Caltech scientist Rudolf Mössbauer discovered that a nucleus in a solid can sometimes emit and absorb gamma rays without recoil, a critical requirement being that the nucleus is embedded in a soild matrix, fixed within the lattice, and no longer isolated. This effect is elegantly described by the expression for the kinetic energy in the recoil, E_{recoil}:

$$E_{\text{recoil}} = \frac{p_\gamma^2}{2m} = \frac{E_\gamma^2}{mc^2}, \tag{2.1}$$

where the momentum $p_\gamma = E_\gamma/\text{c}$, E_γ is the energy of the γ-ray, and c is the speed of light. The conservation of momentum requires the magnitudes of the γ-ray momentum and recoil momentum to be the same. If the mass used in Eq. 2.1 is the mass of a single nucleus, the recoil energy ($\sim 10^{-3}$ eV) is many orders of magnitude larger than the energy precision required by the absorption condition for the second nucleus ($\sim 10^{-9}$ eV). However, if the nucleus is fixed in a lattice, the mass in Eq. 2.1 can be considered equal to the mass of the entire crystal, giving a recoil energy below the nano-eV precision for the transition energy between nuclear states.

An analogy to describe the Mössbauer effect is that of a boy jumping from a boat on the water to land. The boy measures, on land, the furthest distance he can possibly jump. Then, the boy takes his boat out to sea, and positions his boat at the distance of his greatest jump. He jumps from the boat, but fails to land on the shore. This is because of the energy deficiency rising from the recoil of the boat. Likewise, a gamma ray emitted from a free nucleus would not be absorbed by another nucleus due to a recoil reaction in emission. However, if the boy takes his boat to the same position and waits for the lake to freeze over, he can perform the same jump and easily land on the shore. Likewise, in solids, emission and absorption of nuclear gamma rays can occur recoil-free.

Mössbauer made the first observation of recoil-free resonant absorption of gamma rays in ^{191}Ir. Since then, the Mössbauer effect has been detected in over one hundred different isotopes [14]. However, most of the practical applications of Mössbauer spectroscopy have been with a small number of isotopes, most notably among them ^{57}Fe. Observing a significant number of γ-ray emissions is

contingent on the recoil energy of the nucleus being smaller than, or on the order of, short wavelength phonons in the solid. The phonon energies, estimated from Debye or Einstein temperatures of the solid, are in the range of tens of meV. It is also useful for the energy of the gamma ray to be relatively low, 14.4 keV in the case of ^{57}Fe, as this permits smaller recoil energies (as seen from the relation in Eq. 2.1) and more abundant low-lying excited states. An additional requirement is the selection of a suitable source of γ-rays. Typically, a radioactive parent has a sufficiently-long half-life to be useful, but a half-life short enough to provide an abundant number of decays. ^{57}Co is often used as a laboratory source for ^{57}Fe, as it has a reasonable half-life of 271 days.

2.3 Hyperfine Interactions

The recoil-free processes arising from the Mössbauer effect permit resonant absorption with an extremely high energy resolution. Energy levels of a nucleus in a solid are modified by the local environment of the nucleus. Very small energy changes that result from the hyperfine interactions between the nucleus and its surrounding electrons can be detected by measuring the energy dependence of the resonant absorption of Mössbauer γ-rays by nuclei. The Mössbauer spectrum is thus characterized by features including the number, shape, position, and relative intensity of various absorption lines that result from the the nature of hyperfine interactions and their time dependence.

2.3.1 Isomer Shift

The isomer shift is proportional to the electron density at the nucleus, with effects from its neighbors. The electronegativity, covalency, bond strength, and electronic screening of the neighboring atoms can influence the charge density at the iron nucleus. As a result, the isomer shift provides a direct probe of the valence state of the Mössbauer active isotope.

Isomer shift of absorption lines results from the Coulomb interaction between the nuclear charge distribution over the nuclear volume and the electronic charge density over this volume. Excitation from ground state to excited state causes an increase in the nuclear volume, and the difference between electronic densities at the nucleus is different depending on the chemical environment. If

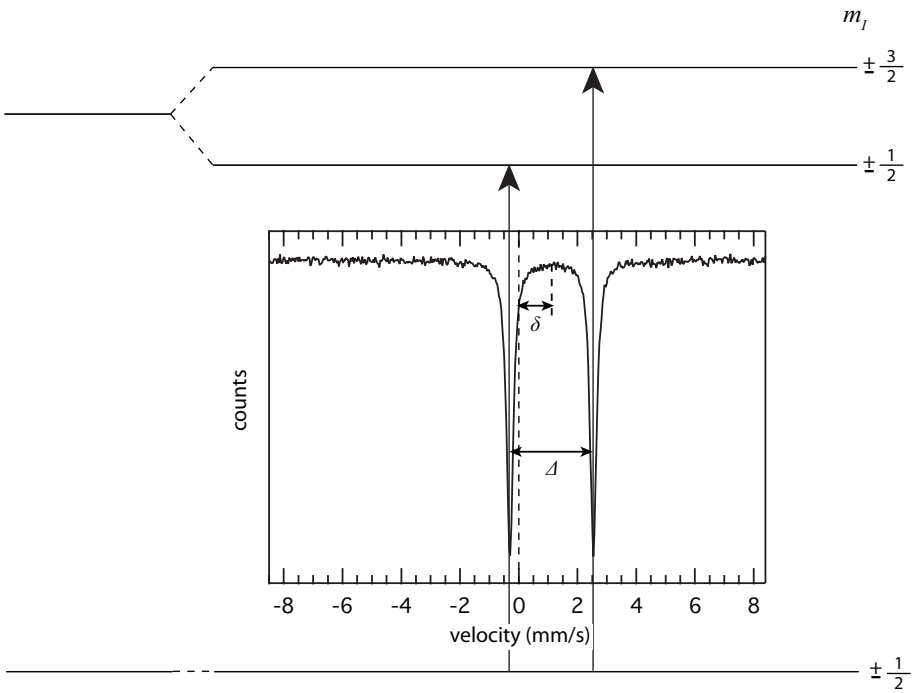

Figure 2.1: The nuclear energy levels of ^{57}Fe in a non-zero electric field gradient demonstrate the quadrupole splitting, Δ, that results from the splitting of the excited state into two substates, and the isomer shift, δ, that results from the difference in energy levels between the source and absorber.

the Coulomb interaction were the only hyperfine interaction affecting nuclear energy levels, the ground state and excited states would be unsplit, but the separation between the states would be different in the source and absorber. This causes a shift in the absorption line, δ, that is the isomer shift.

An example of the role of isomer shift is in distinguishing Fe^{2+} and Fe^{3+}. The valence states of Fe^{2+}, $1s^2 2s^2 2p^6 3s^2 3p^6 3d^6$, and Fe^{3+}, $1s^2 2s^2 2p^6 3s^2 3p^6 3d^5$ differ only by a d-electron. The $3s$-electron spends a fraction of time further from the nucleus than the $3d$-electrons. The electrostatic potential experience by the d-electrons depends on the screening effects of the inner electrons. By adding a d-electron, the attractive Coulomb potential is reduced, allowing the wave function of the $3s$ electrons to expand, reducing its charge density at the nucleus. As a result, removal of the 6th $3d$-electron in going from Fe^{2+} to Fe^{3+} increases the charge density at the nucleus and produces a sizable isomer shift.

2.3.2 Electric Quadrupole Splitting

The nuclear charge distribution was assumed spherical in the discussion of the Coulomb interaction and the resulting isomer shift. However, nuclei have non-spherical charge distributions when their nuclear angular momentum quantum number is $I>\frac{1}{2}$, causing a nuclear quadrupole moment. A quadrupole moment interacts with an electric field gradient caused by an asymmetric electronic charge distribution. When the nuclear quadrupole moment experiences the asymmetric electric field, an electric quadrupole interaction causes the nuclear energy levels to split. This split occurs in correspondence with the different alignments of the quadrupole moment with respect to the principal axis of the electric field gradient. In the simple case of ^{57}Fe in the presence of a non-zero electric field gradient, the excited state has $I=\frac{3}{2}$, which splits into the two substates $m_I=\pm\frac{1}{2}$ and $m_I=\pm\frac{3}{2}$. This results in a two-line absorption spectrum separated by the quadrupole splitting, Δ. Fig. 2.1 shows the effect of the isomer shift and quadrupole splitting on the Mössbauer absorption spectrum for ^{57}Fe in an electric field gradient.

2.3.3 Hyperfine Magnetic Field Splitting

Hyperfine magnetic field splitting occurs in ferromagnetic, ferrimagnetic, and antiferromagnetic materials. When a nucleus is placed in a magnetic field, there is an interaction between the spin of the nuclear states and the magnetic field. The spins can be oriented with different projections along the magnetic field, modifying the energies of nuclear transitions. The energy perturbations that result from the hyperfine magnetic splitting are referred to as the nuclear Zeeman effect.

For states with a nuclear angular momentum quantum number greater than $I>0$, this lifts the degeneracy and causes splitting into $2I+1$ substates. For ^{57}Fe, which is ferromagnetic at room temperature, the ground state has $I=\frac{1}{2}$, which splits into two substates, and the excited state has $I=\frac{3}{2}$, which splits into four substates. Given the selection rule, $\Delta m_I=0, \pm1$, this gives six allowed transitions, and results in a six-line absorption spectrum. Fig. 2.2 shows the Mössbauer spectrum that results from the effect of magnetic splitting in bcc Fe at 300K. The overall splitting of the absorption lines is proportional to the total magnetic field at the nucleus, and the transition

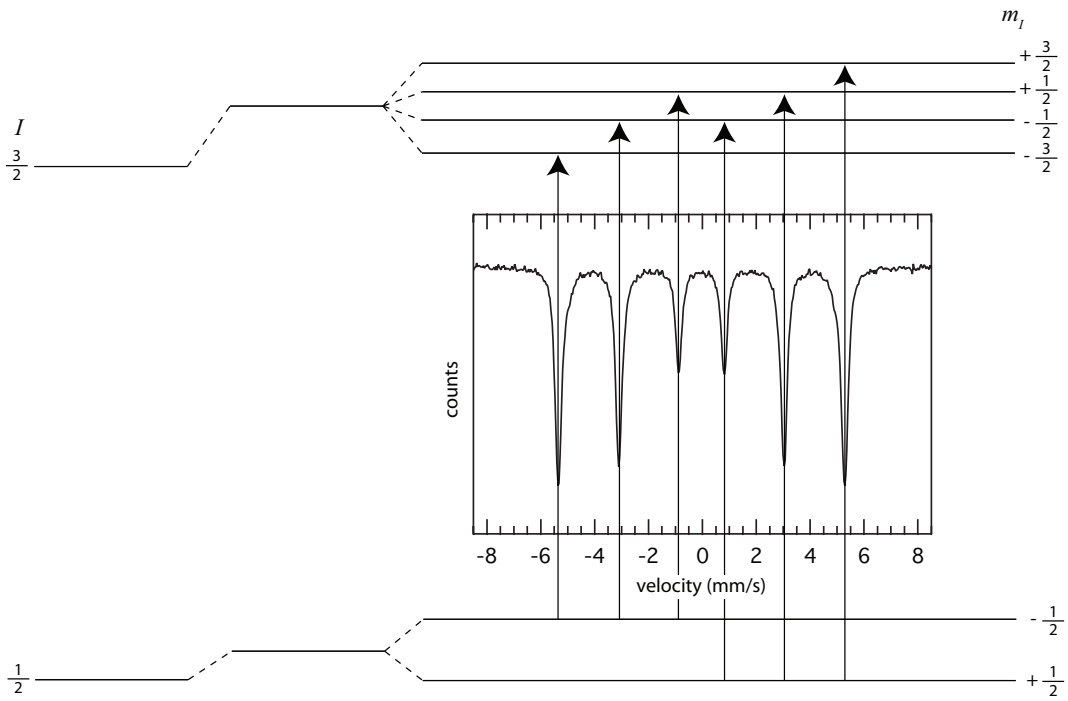

Figure 2.2: The effect of magnetic splitting on the nuclear energy levels of ^{57}Fe is demonstrated for bcc Fe at 300K.

probabilities between the nuclear substates determine the intensities of the lines. The Mössbauer spectrum can therefore give information on the relative orientation of the magnetic field at the nucleus with respect to the direction of the incident γ-ray.

The biggest contribution to the hyperfine magnetic field at the nucleus results from the coupling of the nucleus and its electrons. This coupling is called the Fermi contact interaction. The Fermi contact interaction between a nucleus and an s-electron can be written as follows:

$$H_s = -\frac{16\pi}{3}\beta \left\langle \sum (s\uparrow - s\downarrow) \right\rangle \tag{2.2}$$

where the $s\uparrow$ and $s\downarrow$ are the spin up and spin down s-electron densities at the nucleus and β is the Bohr magneton. The charge densities of the spin up and spin down s-electrons may be different even in filled s-shells if the atoms contains another partially filled magnetic shell, such as the $3d$-shell. The exchange interaction between the spin up s-electron and spin up polarized d-shell is attractive,

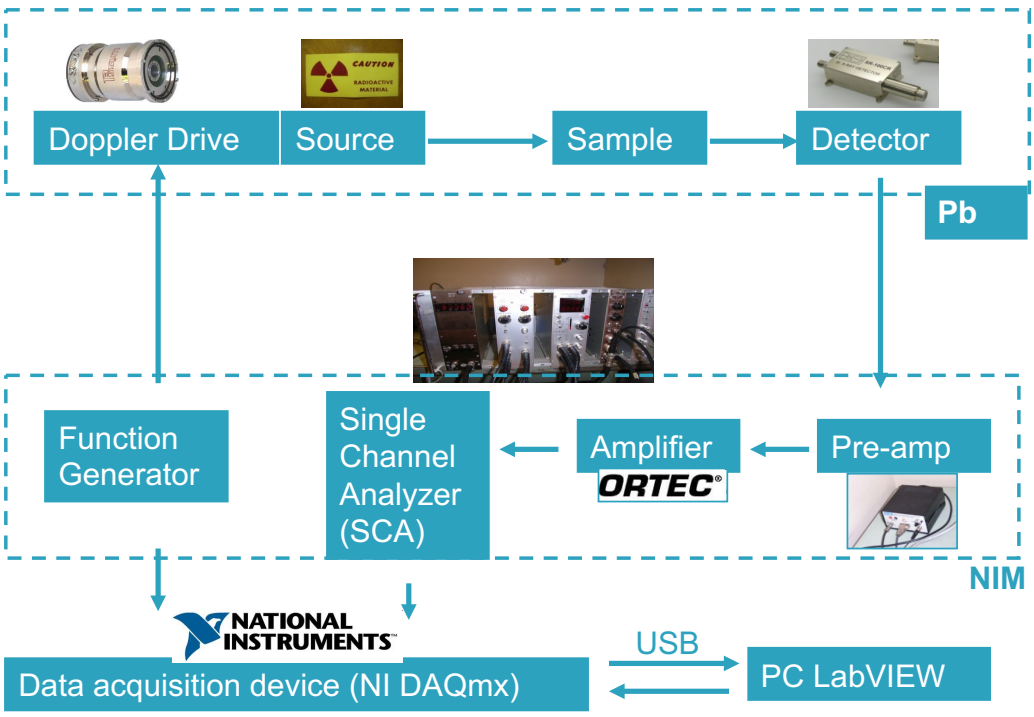

Figure 2.3: Schematic of the Mössbauer spectrometer in use at Caltech. The spectrometer is arranged in transmission geometry and shielded by lead bricks. The signal from the detector is outputted to a series of electronics for pulse shaping, amplification, and selection. The detector signal and the timing of the doppler drive interface with a National Instruments data acquisition card. This card converts the analog signal to TTL pulses that are read by Labview software. Reproduced from [4].

but the interaction between the spin down s-electron and d-shell is repulsive. Thus, the spin density terms in Eq. 2.2 do no cancel, resulting in a Fermi contact interaction field.

2.4 Experimental Setup

The Mössbauer spectrometer currently in use at Caltech follows a traditional setup for conventional constant acceleration systems. The radioactive source emits γ-rays that are directed at the absorber (sample), with a detector placed in transmission geometry to collect transmitted photons.

The radiation source is ^{57}Co embedded in a Rh matrix. The ^{57}Co undergoes a spontaneous electron capture transition to give a metastable state of ^{57}Fe via 122-keV γ-emission. This state in turn decays 141 ns later to the ground state via a γ-ray cascade, which includes the 14.41-keV γ-ray. Measuring the hyperfine structure of the energy levels of the Mössbauer nucleus in the absorber

requires tuning the energy of the γ-rays emitted by the source so that they can have the correct energy for resonant absorption. This is accomplished by moving the source relative to the stationary sample by a mechanical Doppler drive to give the γ-rays an energy shift $\Delta E = 14.41$-keV. The source motion is oscillatory with constant acceleration and deceleration in both directions, providing an energy scan.

Resonant absorption occurs when the energy of the γ-ray incident on the sample just matches the nuclear transition energy for a Mössbauer nucleus in the sample. Over time, the accumulated resonant absorption results in a spectrum of γ-ray counts against the velocity of the source with respect to the absorber, measured in mm/s. Practically, the counts are accumulated in 1024 channels, where channels 1-512 accumulate counts in the translation of the source in one direction, and channels 513-1024 in the opposite direction. In this manner, the data can be folded about the median channel to combine the data accumulated for the same magnitude of velocity.

Figure 2.3 shows a schematic of the Mössbauer spectrometer in use at Caltech. The source sits on a doppler drive and is arranged linearly in transmission geometry with the sample and detector. These components are contained inside lead bricks to provide shielding from radiation. The doppler drive receives its signal from a function generator, which also outputs the timing to a National Instruments data acquisition card. The signal from the detector is sent to a pre-amplifier where the pulse is shaped, and then an amplifier. In the single channel analyzer, the amplified analog signal is selected and converted to TTL pulses, then outputted to the data acquisition card. This signal, combined with timing information sent from the function generator, interfaces with a PC-based Labview program.

Calibration of the velocity of the source is performed by measuring a room-temperature α-Fe spectrum. Figure 2.4 shows the measurement of α-Fe as a function of channel number (top axis) in black. The spectrum has been fit with six independent Lorentzian functions with unconstrained centers, widths, and depths in red. The M1 and M6 peaks used in converting channel number to velocity are identified. The difference in the M1 and M6 peak centers is Δ_{M1-M6}. The separation between beaks M1 and M6 is assumed to be 10.62 mm/s. To determine the mm/s per channel:

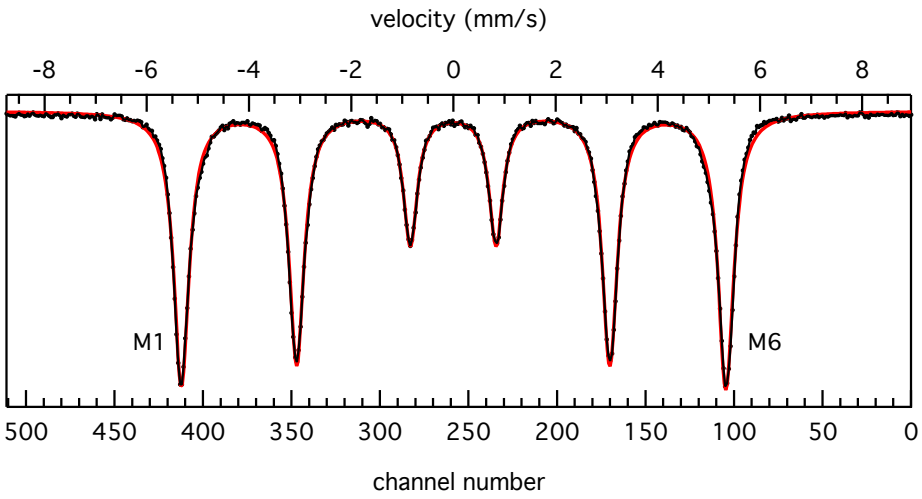

Figure 2.4: To convert channel number to velocity, α-Fe is measured as a function of channel number (top axis) in black. The spectrum has been fit with six independent Lorentzian functions with unconstrained centers, widths, and depths in red. The M1 and M6 peaks used in converting channel number to velocity are identified.

$$\text{mm/s per channel} = \frac{10.62\,\text{mm/s}}{\Delta_{\text{M1}-\text{M6}}}. \tag{2.3}$$

The centroid position is also calculated from the peak centers of M1 and M6:

$$\text{centroid position} = \frac{\text{M1} + \text{M6}}{2}. \tag{2.4}$$

The centroid channel is assigned zero velocity. Channel number can then be converted to velocity using the expression in 2.3. Assignment of channel 1 to a positive or negative velocity value depends on the direction of the drive translation. In the case where the drive moves in the negative direction for channels 1-512 and in the positive direction for channels 513-1024 (as is the case with spectrometer at Caltech), channel 1 should be assigned a positive velocity value.

Chapter 3

Nuclear Resonant Inelastic X-ray Scattering

With the traditional lab Mössbauer spectroscopy technique described in Chapter 2, resonant absorption with an extremely precise energy range is used to probe the local environment of the nucleus. Information about the hyperfine interactions between the nucleus and its electrons is obtained by measuring energy changes in the range of neV that result from these interactions.

By replacing the radioactive source in a typical Mössbauer experiment with synchrotron radiation, new experimental probes become available owing to the high spectral brilliance of available radiation and the time structure of the synchrotron. Nuclear resonant inelastic x-ray scattering (NRIXS) is an incoherent inelastic γ-ray scattering technique based on the Mössbauer effect. By measuring nuclear absorption at energies detuned from resonance by several meV, the typical energies of phonons, the phonon density of states can be obtained. In effect, while traditional Mössbauer spectroscopy is recoilless, NRIXS measures the recoil energy of the nucleus off-resonance where γ-ray absorptions are accompanied by the creation or annihilation of a phonon.

3.1 Background

Mössbauer's discovery generated considerable investigation into other ways that nuclear resonant absorption could be used. In 1960, Singwi and Sjölander provided a framework for how γ-ray absorption by nuclei could influence lattice dynamics [15]. The same year, Visscher outlined an

experiment to determine the frequency distribution of crystal lattice vibrations based on the Debye model [16].

Two major limitations prevented Visscher's experiment from being fully realized for several decades. First, tuning the energy of the incident energy to the order of phonon energies in a traditional Mössbauer set-up requires Doppler velocities on the order of hundreds of m/s[1]. Second, the finite lifetime of vibrational excitations causes the resonance line to broaden, and reduces the peak absorption cross-section by several orders of magnitude in comparison to the elastic peak. These obstacles are overcome with use of synchrotron radiation, as is discussed in the next section.

The first phonon spectra recorded by NRIXS were reported in 1995 using undulator radiation at three difference synchrotrons, and achieved energy resolution around 6 meV [18, 19, 20]. Current measurements can now achieve sub-meV energy resolution.

3.2 Experimental

Nuclear resonant inelastic x-ray scattering (NRIXS) experiments are possible at third-generation synchrotrons, where beam flux optics and high-resolution monochromators can tune the incident x-ray beam to a few meV. Beamlines are most commonly configured for the ^{57}Fe isotope, but monochromators are available for some other Mössbauer isotopes [5]. The incident beam is focused using Kirkpatrick-Baez mirrors to a spot size of 30 x 50 μm, which makes it possible to measure very small samples. The work described in this thesis was performed at beamlines 3-ID-B and 16-ID-D at the Advanced Photon Source of the Argonne National Laboratory [21, 18, 19].

When the sample is irradiated with γ-rays matching the nuclear transition energy, both nuclear and electronic excitations occur. Scattering of x-rays by electronic processes is very fast, less than 1 ps. However, the natural lifetime of the ^{57}Fe nucleus is $\tau=\hbar/\Gamma=141$ ns. This creates a scattering intensity profile shown schematically in Fig. 3.1. A pulse of radiation arrives at time=0, and intense electronic scattering occurs almost immediately, while the decay of resonant nuclei from the excited

[1] While limiting, this was what was done prior to Mössbauer's discovery of recoil-free absorption and emission in a solid. The first experiment measuring the phonon spectrum of TbO_x was performed in 1979 by rotating a radioactive source at high speeds to produce Doppler shifts up to 30 meV for the 58 keV radiation of the ^{159}Tb isotope [17].

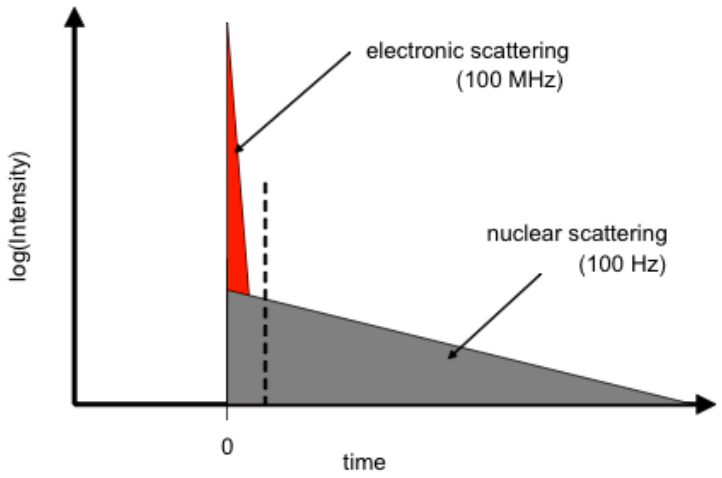

Figure 3.1: Scattered intensity versus time demonstrates the convenient discrimination possible between electronic scattering, which occurs immediately after arrival of the synchrotron pulse at time=0, and nuclear scattering, which has a longer lifetime. The detector is programmed with 'dead time' between time =0 and the dashed line to ignore electronic scattering. Figure adapted from [5].

state is delayed. Thus, the nuclear and electronic scattering can be separated using time discrimination. Avalanche photodiode detectors with a time resolution on the order of 1 ns are used to measure decay products, and are gated for 20 ns of 'dead time' to ignore electronic scattering [5]. Effective time discrimination also requires that the pulses of incident radiation be spaced far enough apart to allow de-excitation from the excited state and measurement of decay products before the next pulse re-excites the nuclei. The standard time structure at the Advanced Photon Source is 150 ns between bunches (groups of electrons) and a 70 ps duration for each pulse, making it well-suited for these measurements.

As with traditional Mössbauer spectroscopy, resonance excitation occurs if the energy of the incident photon exactly matches the resonance energy of the nucleus. When the incident energy is is greater or less than the resonant energy, an additional amount of energy must be absorbed or emitted to achieve the exact resonance energy for nuclear excitation. This compensating energy can come from the creation or annihilation of phonons. As shown schematically in Fig. 3.2, if the incident γ-ray is lower than the resonance energy, a phonon must be annihilated for the nucleus to absorb the photon, and if the incident γ-ray has an energy higher than the resonance energy, a phonon is created to reduce the energy of the incident photon and permit absorption.

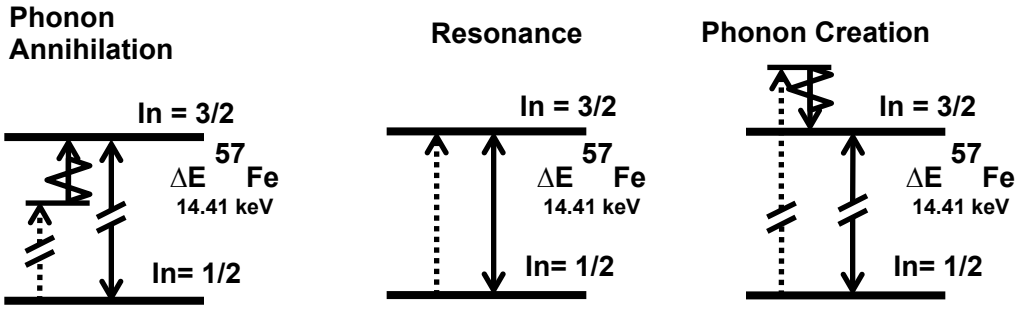

Figure 3.2: Incident photons may not always have the exact energy necessary for nuclear excitation (middle), in which case the creation or annihilation of a phonon can compensate for incident photons with too much or not enough energy for resonance excitation. Diagram courtesy of Lisa Mauger.

Thus, by sweeping the incident x-ray energy with steps of 0.5 meV and ranges of typically ±120 meV, the phonon density of states is built as a histogram of phonons created or annihilated at each energy. The strength of the vibrational transition is determined by the number of phonon states at a given energy and their thermal occupation number.

The observed phonon spectra have three main features. An elastic peak for resonance excitation occurs at E=0 (this is the Mössbauer effect). The excitation probability of an Einstein solid predicts that the elastic line will dominate, followed by one phonon processes, two phonon processes, etc. Inelastic side bands result from the creation or annihilation of one phonon or multiple phonons. The positive energy side features phonons created by photons incident with too much energy to excite the nuclear resonance. The negative energy side features the phonons annihilated by incident photons with not enough to excite the nuclear resonance. A phonon spectrum demonstrating these features is shown in Fig. 3.3 for a bcc Fe foil measured at room temperature.

An additional intrinsic feature of the phonon spectrum is the imbalance between excitation probability densities for phonon creation, $S(E)$, and phonon annihilation $S(-E)$. This imbalance is known as 'detailed balance.' Relating these excitation probability densities using the Botlzmann factor, $S(-E)=S(E)\exp(-E/k_BT)$ allows determination of the temperature T at which the spectrum was recorded [22].

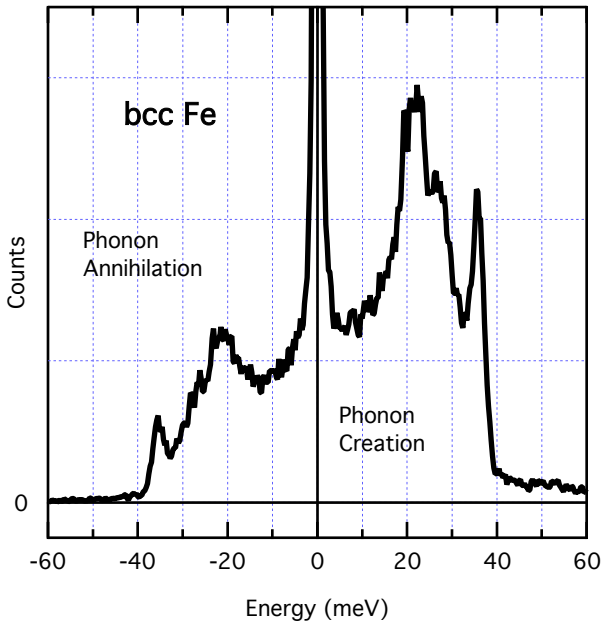

Figure 3.3: A phonon spectrum for bcc Fe at room temperature, measured with NRIXS. Typical features are the elastic scattering at E=0, and inelastic sidebands resulting from photon creation and annihilation from incident photon energies detuned from the nuclear resonance energy.

3.3 Data Analysis

Reduction of the measured data to the phonon density of states is relatively straightforward. Data presented here were reduced using the program PHOENIX [23]. First, the elastic peak is removed. This can be done either by specifying the resolution function of the monochromator (from an experimental measurement), or by choosing a set of parameters that simulate a Gaussian-like function internally. The spectrum is then renormalized, and several moments of the spectrum are calculated, including the average kinetic energy of the atom (second moment) and average force constant for the atom (third moment).

Next, the one-phonon scattering spectrum is isolated by removing the elastic contribution and scattering from multiple phonons. An iterative process called the Fourier-log method extracts 1-, 2-, and 3-phonon terms [24]. The resulting spectrum is the phonon DOS from one-phonon scattering for the ^{57}Fe atoms in the sample. Thus, when the sample being studied contains additional elements, the spectrum is often referred to as the partial DOS, or pDOS.

Absent from the standard data reduction procedure is the generation of error bars on the measured intensities. The PHOENIX program provides error margins that are obtained by propagating the statistical uncertainties of the measured data. For NRIXS, this is not as much of a shortcoming as it may seem. The technique is inherently low background, as shown in Fig. 3.3.

Part 2: Entropy and Phase Transformations

Chapter 4

Vibrational entropy of nanostructured fcc Cu–6% Fe

4.1 Introduction

The chemical entropy of mixing has the well-known configurational contribution

$$S_{\rm cfg} = -k_{\rm B}\left[(1-c)\ln(1-c) + c\ln c\right] \ , \tag{4.1}$$

which can be obtained from the statistics of a random solid solution. (Here, c is the mole fraction of solute in a binary mixture, and is the mole fraction of iron in the present work.) It is best understood when the solid solution is referenced to pure elements, for which $S_{\rm cfg} = 0$. When unmixing occurs on a small spatial scale, however, there may be a substantial volume fraction of material of intermediate compositions, and these compositional inhomogeneities evolve during an unmixing transformation.

The vibrational entropy $S_{\rm vib}$ also evolves during unmixing [25], and for a binary alloy it is

$$\begin{aligned} S_{\rm vib}(T) &= 3k_{\rm B}\int_0^\infty \left[\,(1-c)g_{\rm Cu}(\varepsilon) + c\,g_{\rm Fe}(\varepsilon)\,\right] \\ &\times \left[(1+n_\varepsilon)\ln(1+n_\varepsilon) - n_\varepsilon \ln n_\varepsilon\right]\ {\rm d}\varepsilon \ , \end{aligned} \tag{4.2}$$

where $n_\varepsilon(T) = (\exp(\varepsilon/(k_{\rm B}T)) - 1)^{-1}$ is the Planck occupancy factor at the temperature T. In the present study, $g_{\rm Cu}(\varepsilon)$ and $g_{\rm Fe}(\varepsilon)$ are phonon partial densities of states (pDOS) for copper and iron atoms normalized to 1, and the mole fraction of iron is c. Here, the interface is assumed to make

no contribution to S_{vib}, but this can be checked experimentally. There has been some work on the change of vibrational entropy of unmixing [25], but very little work on how it might depend on small-scale compositional inhomogeneities in the material.

The present investigation on iron unmixing from an fcc copper matrix was performed to measure the iron phonon partial DOS $g_{\mathrm{Fe}}(\varepsilon)$, from which we obtain the contribution of iron atoms to the vibrational entropy with Eq. 4.2. A previous study on dilute ^{57}Fe in fcc Cu used a similar method to identify the vibrational spectrum of fcc Fe [26]; however, in the present work, we examine carefully a series of samples annealed from as-prepared material, studying the state of chemical unmixing by three-dimensional atom probe tomography, the crystal structure by x-ray diffractometry, the magnetic state by Mössbauer spectrometry, and correlate these changes in the phonon spectrum to chemical and structural changes of the nanostructure. Our goal is to better understand how the vibrational entropy changes with chemical unmixing, for which we find the dominant effect to be the formation of regions of bcc Fe.

4.2 Vibrations in Nanocrystals

Vibrations of small crystals have been studied for many years. Calculations for both isolated nanocrystals [27, 28] and nanocrystals with rigid constraints [29] established the characteristic enhancement in the number of modes at low energies that has been observed in all subsequent experiments and calculations of the DOS for nanomaterials. This trend implies that the extra spectral weight at low energies originates from degrees of freedom in the microstructure, which may include vibrations that tend to localize at grain boundary regions or propagate along them, motion of the nanocrystals with respect to each other, or some combinations of these degrees of freedom. Investigation into the exact nature of these additional modes at low energies, including their dimensionality and origin, has been the subject of frequent study over the last 15 years.

The establishment of the NRIXS technique has lent considerable experimental weight to the quantitative understanding of these spectral enhancements owing to its inherent low background[30, 31, 32, 33, 34, 35, 36, 37, 38, 39, 40]. Refinement of theoretical tools, namely molecular dynamics

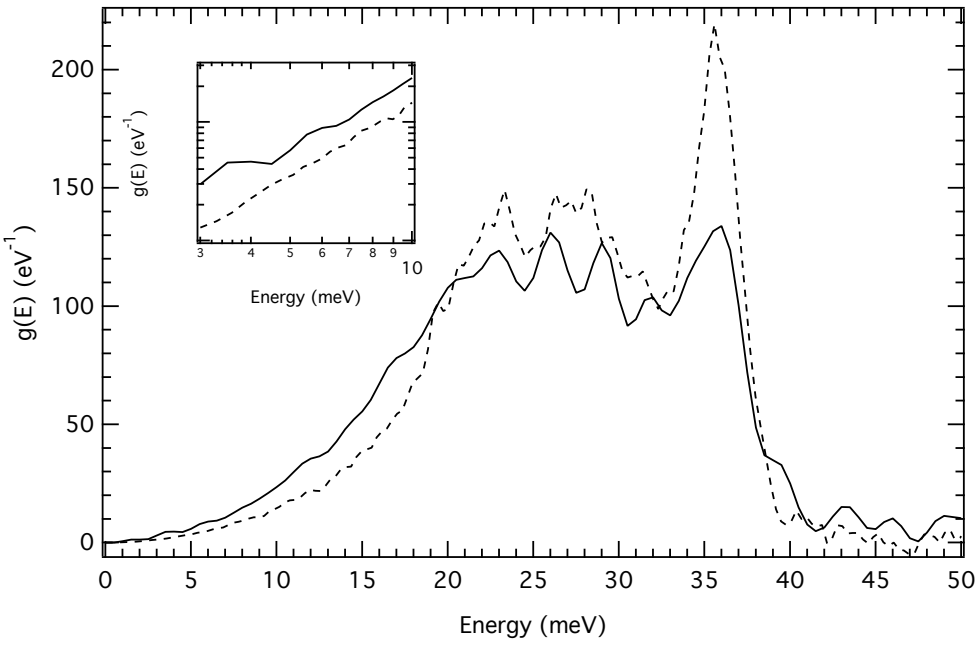

Figure 4.1: Bulk bcc Fe (solid line) and Cu-5.6 at.% ^{57}Fe with ∼28 nm iron crystallites. The characteristic enhancement of the phonon DOS at low energies and broadening of spectral features is evident from comparison of these two spectra.

simulations and techniques to define symmetry within a particle, has also led to the continual development of this field.

The earliest experimental reports of changes to the phonon DOS for nanocrystalline materials were from three independent inelastic neutron scattering measurements performed in 1995. Suzuki and Sumiyama reported hints that the high-frequency components of phonon spectra are altered in nanocrystalline Ta [41], but described no general trends. The large enhancement of the phonon DOS at low energies was reported for Ni_3Al with a 7 nm crystallite size, although it was suggested at the time of the report that this enhancement could have been caused by quasielastic scattering by hydrogen in the material. A study of nanocrystalline Ni also showed a strong enhancement in the DOS below 15 meV for compacted nanoparticles when compared to polycrystalline Ni. [42] A subsequent inelastic neutron scattering measurement the following year corroborated the Ni_3Al result [43]. Measurement of 12 nm and 28 nm nanocrystalline Fe, which is not expected to absorb a significant amount of hydrogen, definitively established the enhanced DOS at energies below 15

meV for nanophase materials, confirming that the changes to the DOS observed for Ni_3All were likely not from quasielastic scattering of hydrogen.

The characteristic enhancement of the phonon DOS at low energies, and broadening of spectral features, is shown in Fig. 4.1 for bulk bcc iron in comparison with results for the Cu-5.6 at.% ^{57}Fe presented in Section 4.3. The nanomaterial here is for Fe crystallites ∼28 nm in size embedded in a Cu matrix.

The distortions of the phonon DOS are larger for materials with smaller crystals. In particular, the enhancement of of phonon DOS at low energies increases with the inverse of the crystallite size. This size-dependency was demonstrated for inelastic neutron scattering measurements of nanocrystalline fcc Ni_3Fe, with sizes ranging from 6 to 50 nm. [32] Nanocrystalline nickel-iron powders were synthesized by mechanical alloying and subjected to heat treatments to alter their crystallite sizes and internal strains. It was determined that the enhancement of the phonon DOS at low energies decreased with crystallite size d as d^{-1}. The coefficient α, obtained from a fit of the DOS below 15 meV to the Debye law

$$g(\varepsilon) = \alpha\varepsilon^2 \tag{4.3}$$

plotted against inverse grain size shows a linear relationship. This relationship suggests that the phenomena at low energies is related to the surfaces of the crystallites, such as surface modes; however, the authors caution against over-extrapolating these results, as the frequency spectrum of surface modes should depend on the nature of the contacts between crystallites, and these contacts probably change during the annealing process used to alter particle size.

This same size effect was also reported for bcc iron nanoparticles prepared by inert gas condensation and measured in nuclear resonant inelastic x-ray scattering [34], This work speculates that oxidation, in addition to interface vibrational modes, plays a role in the enhancement of low-energy modes, but affirms the increase in low-energy modes with decreasing particle size. A plot of the coefficient α, calculated from the fit of the DOS to Eq. 4.3 in the 1.5 -10 meV range, against a calculated

fraction of iron particles that are pure bcc (obtained by subtracting the fraction of oxidized atoms from one) shows a strong correlation between the coefficient α and fraction of pure iron particles, though it is not quantitatively linear. The authors note that the decrease in particle size tends to raise α solely by increasing the fraction of interfacial sites, speculating that the DOS is thus a sum of a partial DOS of interfacial atoms that depends on particle size and a partial DOS of crystalline atoms that is independent of particle size.

For consolidated nanocrystals, the enhancement in the phonon DOS at low energies does not extend to arbitrarily low energies and arbitrarily long wavelengths. Measurements of phonons in the micro eV energy range performed found the phonon DOS of nanocrystalline bcc Fe and fcc Ni_3Fe to be enhanced at micro eV energies compared to bulk samples, but the enhancement was markedly greater at meV energies [31]. The enhancement in the DOS at micro eV energies is more characteristic of long waves in a homogeneous medium resulting from a reduction in sound velocity. This suggests that the enhancement in the meV energy range originates with features of the nanostructure, while the long-wavelengths of the micro eV energies are involved in the cooperative motions of many nanocrystals. The compact microstructure of nanocrystals forms a coupled dynamical system, but surface modes are still expected when the grain boundaries have altered densities of force constants. The change in enhancement between the two energy ranges is the characteristic behavior of a 'confinement effect' where there are no phonon modes below a long-wavelength low-energy cutoff. The cutoff of surface modes at long wavelengths is qualitatively consistent with the smaller enhancement of the DOS at micro eV energies.

Many experiments have sought to gain further insight into whether these low-energy excitations of nanocrystalline materials show characteristics of reduced dimensionality. In the continuum limit, all sound waves have linear dispersions with $\varepsilon/\hbar{=}\omega{\propto}k$, so in three dimensions, $g(\varepsilon) \propto \varepsilon^2$. Fitting to $g(\varepsilon)$ to obtain the exponent n of $g(\varepsilon) \propto \varepsilon^n$ is the common method for establishing dimensionality.

In this context, the physical nature of the low-E excess modes in nanocrystalline materials has been reported to be linear [44], nonlinear [45, 46, 47], and Debye-like quadratic [48, 42, 43, 30, 32, 33, 34, 31, 49]. Theoretical work investigating the origin of low-energy modes in nanoparticles has

sought to separate the atoms of nanoparticles and their corresponding DOS into groups according to the degree of symmetry. Molecular-dynamics calculations of 100 grains of Ni or Cu atoms with grain sizes between 5 and 12 nm were performed, and the DOS curve separated for contributions from three types of atoms determined by topological short-range analysis.[46] These calculations determined low-energy enhancement to be caused mainly by the grain boundaries, with internal surfaces playing only a minor role, and atoms inside the grains retaining the DOS of bulk material.

Experimental investigation attempting to distinguish the vibrational properties of the interiors of nanocrystalline materials and their interfaces with other particles were performed for NRIXS measurements of $Fe_{90}Zr_7B_3$ with particle sizes between 2 and 15 nm.[49] The relative fractions of interfaces and interiors were determined by conversion electron Mossbauer spectroscopy in which the spectra were decomposed into contributions from atoms located in nanoparticle interiors, at the surfaces of the interior, and at grain boundaries. This work assumed that the DOS could be decomposed into contributions from each of these regions, the relative weights of which were determined from the Mossbauer spectra. This experiment corroborated the previous theoretical work, finding that the anomalous enhancement of the DOS at low energies originates from the DOS of the interfaces and grain boundaries, with the DOS from the nanoparticle interiors resembling that of the bulk. Further, it was determined that the enhancement of the DOS at low and high energies scales linearly to the atomic fraction of interface atoms.

The origin of the low-energy mode enhancement in nanoparticles has remained an open question for which numerous experiments have been undertaken to identify the specific origins of the unique phonon spectra of nanocrystals, and to decouple competing effects including the nature of surface atoms, low-coordinated interfacial atoms, and oxide surfaces [39, 35, 40]. The most recent experimental work to address this question was performed on supported, isolated, size-selected nanoparticles that were capped with a Ti layer to prevent oxidation, representing the most thorough attempt to decouple competing effects including the nature of surface atoms, low-coordinated interfacial atoms, and oxide surfaces[50]. The surprising result was found that 3D-Debye behavior was observed for nanoparticles with an average height of less than 2 nm, but non-Debye behavior, n=1.4, was found

for slightly *larger* nanoparticles ranging from 2.6-6 nm in height. The authors conclude that this result can be explained by considering the larger nanoparticles to be polycrystalline, thus containing grain boundaries in their interior, while the smaller nanoparticles have a single grain structure. Thus, the reduced effective dimensionality in the larger particles is due to low-energy vibrational modes at grain boundaries.

4.3 Experimental

Powders of Cu and 5.6 at.% ^{57}Fe were mixed with 5 wt.% stearic acid, and sealed in a steel vial in a high-purity argon atmosphere. Ball milling was performed with a Fritsch Planetary Mono Mill for 92 hours at 400 rpm using a steel ball-to-powder weight ratio of 92:1. After milling, the material was sonicated in isopropyl alcohol, centrifuged, and decanted to remove the stearic acid. The materials were sealed in a quartz ampoule under vacuum, and annealed by ramping to temperature over 30 minutes, heating constantly for 1 hour at $\pm 4^{\circ}$C, and immediately cooling. The samples were then enclosed in Kapton sample holders for x-ray diffraction (XRD), Mössbauer spectrometry, and nuclear resonant inelastic scattering (NRIXS) measurements. The same material was used for atom probe tomography (APT).

X-ray diffraction (XRD) patterns were collected for all samples using Cu Kα radiation. Rietveld analyses was used to determine lattice parameters, crystal size, and root-mean-squared strain and corresponding errors. The Cu powder used for sample synthesis was also characterized by XRD at room temperature, and analyzed in the same manner. Mössbauer spectrometry was performed at room temperature with a conventional constant acceleration system with a radiation source of ^{57}Co in a Rh matrix. Velocity and isomer shift calibrations were performed with reference to the room-temperature α-Fe spectrum.

Atom probe tomography (APT) analysis was performed on specimens from three different annealing temperatures and the as-prepared material using a Cameca Local Electrode Atom Probe (LEAP ®) 3000XSi. Specimens were prepared using a dual electron beam-focused ion beam (FIB) site-specific extraction technique [51]. The lifted-out specimen wedge was attached to 2 μm $\times$ 2 μm

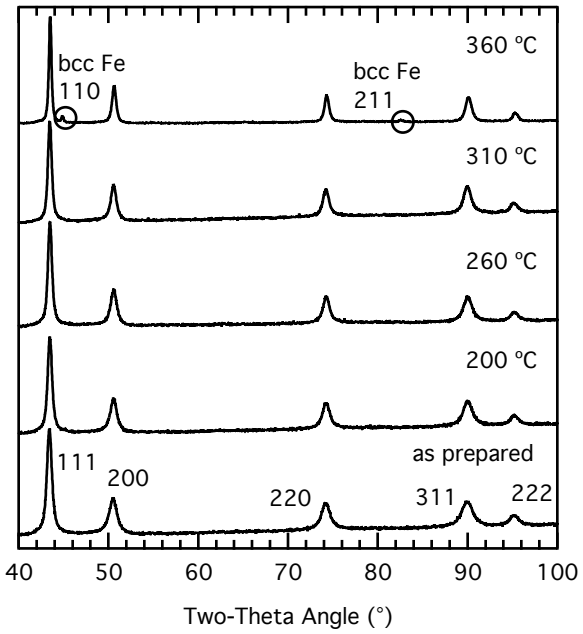

Figure 4.2: XRD pattern from Cu-6%Fe in as-prepared state, and after annealing for 1 h at 200°C, 260°C, 310°C and 360°C. The main peaks are from the fcc Cu matrix.

$\times$ 100 μm Si mounting pillars for handling, and then subsequently annular-ion-milled to form the required needle shape geometry. In the final milling step, the accelerating voltage of the FIB was reduced to 5 keV to limit the Ga ion implantation and surface damage while sculpting the specimen tip radius to approximately 100 nm [52]. The sculpted tips were then placed into the LEAP analysis chamber at a base pressure of $< 10^{-10}$ Torr. All specimens were run at 30 K using laser-assisted field evaporation pulse energies of 0.3 nJ, a pulse rate of 250 kHz, and a target evaporation of 0.5%.

The datasets were reconstructed using standard software. For the as-prepared and 260°C annealed samples, a core methodology, commonly called an 'envelope clustering method', was performed [53]. In this method, the data sets of atoms are statistically determined to be either spatially random or nonrandom. If the distribution is nonrandom, a maximum separation distance, $d_{\max}$, is defined to capture a minimum number of solute atoms, and is used to search for clusters in the dataset. We used a $d_{\max}$ of 0.61 to 0.65 nm, with a minimum number of 33 Fe atoms, to define a cluster. For the 310°C and 360°C samples, the chemical partitioning was significant, and did not require the envelope clustering analysis. Instead, isoconcentration surfaces were used to delineate

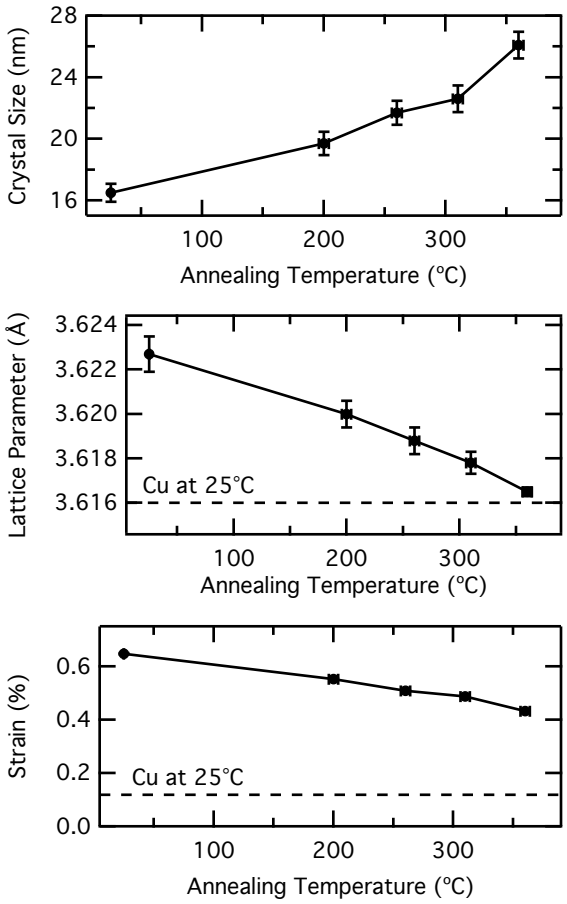

Figure 4.3: Crystal size, lattice parameter, and lattice strain are determined from fitting to the XRD patterns shown in Figure 4.2 from Cu-6%Fe in as-prepared state, and after annealing for 1 h at 200°C, 260°C, 310°C, and 360°C. Parameters of Cu powder at 25°C are shown for reference as dashed lines.

the segregation. The isoconcentration surface value was determined by finding the cross-over composition value between the Fe-enriched and Fe-depleted portions of the interdiffusion compositional curve. Hence, the isoconcentration surface created by this value determined the composition within the surface (cluster) and outside the surface (matrix).

Nuclear resonant inelastic scattering (NRIXS) was performed at beamlines 3-ID-B and 16-ID-D at the Advanced Photon Source of the Argonne National Laboratory [21, 18, 19]. The incident photon energy was tuned to 14.4125 keV, the nuclear resonance energy of ^{57}Fe, and data were collected in scans of incident photon energy from –80 to +80 meV around the elastic peak. All measurements were performed at room temperature. The monochromator resolution function was measured *in-situ* using a single avalanche photodiode detector in the forward direction. The full-width-at-half-maximum was approximately 1.0 meV for all samples measured at 3-ID-B, and 2.3 meV for the sample annealed at the highest temperature and measured at 16-ID-D. The software package PHOENIX[23] was used to extract the pDOS $g_{\mathrm{Fe}}(\varepsilon)$ from the NRIXS data.

4.4 Results

The XRD patterns of Fig. 4.2 are dominated by the fcc phase. At the highest annealing temperature of 360°C, the emergence of the (110) peak for bcc Fe is visible at the base of the (111) fcc Cu peak. Figure 4.3 shows that annealing induces some grain growth and strain relief, even at the lowest annealing temperature of 200°C.

The APT measurements produce three-dimensional chemical maps of particles of each sample. Fig. 4.4 shows images flattened from three dimensions. These include a composite of both iron and copper atoms together, and two separate images showing only iron atoms and only copper atoms. They show only small composition heterogeneities in the sample annealed at 260°C, and the formation of iron-rich regions after annealing at higher temperatures.

Analyses of the APT measurements are summarized in Table 4.1. Cluster analysis on the as-prepared and 260°C samples yielded 34 clusters in each case. These results indicate a small enrichment of Fe atoms in the clusters of the as-prepared samples, and further heterogeneity of Fe after

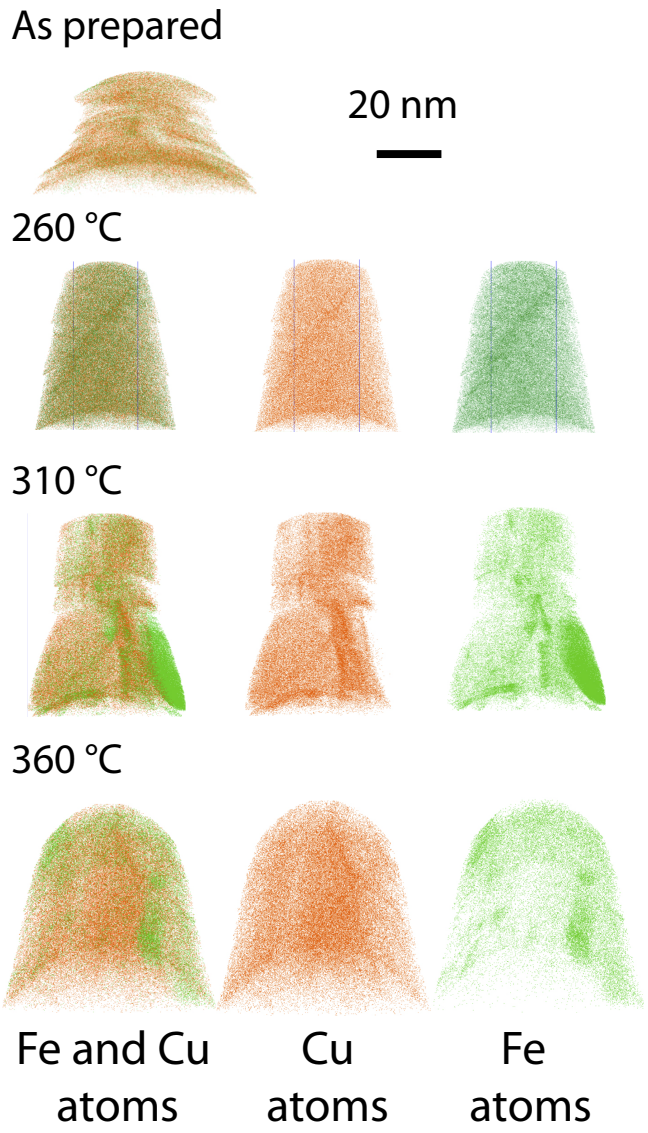

Figure 4.4: Atom probe tomography measurements from Cu-6% Fe after annealing for 1 h at 260°C, 310°C and 360°C. The left column shows the atom positions from both iron and copper, the middle column shows only copper atoms, and the right column shows only iron atoms.

Table 4.1: Matrix and cluster compositions result from analysis of the APT data using cluster analysis for the as-prepared and 260°C samples and isoconcentration surfaces in the 310°C, and 360°C samples.

	Clusters		Matrix		Composition
	% Cu	% Fe	%Cu	%Fe	Difference
as-prepared	94.40 ± 0.06	5.60 ± 0.06	96.50 ± 0.08	3.50 ± 0.05	2.10 ± 0.11
260°C	91.97 ± 0.03	8.03 ± 0.03	95.06 ± 0.07	4.94 ± 0.07	3.12 ± 0.10
310°C	89.32 ± 4.29	10.58 ± 4.18	94.57 ± 0.74	5.43 ± 0.74	5.15 ± 4.92
360°C	93.15 ± 2.12	6.85 ± 2.12	98.27 ± 0.20	1.73 ± 0.21	5.12 ± 2.33

annealing at 260°C. Nineteen isoconcentration surfaces at 2.72% Fe and seventeen isoconcentration surfaces at 1.29% Fe were defined in the 310°C and 360°C samples, respectively. The composition difference, which is the difference in the amount of iron contained in the clusters and matrix for each sample, indicates that the clusters are becoming increasingly iron-rich with increasing annealing temperature. While these values provide a useful quantification of the compositional changes in the samples, the results are dependent on the region of the sample selected for measurement, and thus subjected to the broader, natural composition fluctuations throughout the sample. In particular, the randomly-selected region measured in the sample annealed at 360°C contains a much lower percentage of iron than in other samples measured.

Figure 4.5 shows that the Mössbauer spectrum for the as-prepared material is paramagnetic, as expected for iron atoms in a nonmagnetic fcc Cu matrix. After annealing at the highest temperatures, the ferromagnetic sextet of peaks from bcc Fe appears. It is visible to a limited extent at 310°C, before dominating at 360°C, along with some paramagnetic iron.

For comparison with our measured pDOS curves, an fcc Cu DOS was obtained from a Born-von Kármán calculation that used interatomic force constants from the results in the literature [54]. The fcc phase of iron is not stable at room temperature, but two curves for fcc Fe are presented in Fig. 4.6 for comparison. One is from a measurement on fcc Fe at 6 GPa and 920 K with NRIXS by Shen, et al [7]. Although there is a phonon softening caused by thermal expansion and a phonon stiffening under pressure, from the thermal expansion and the bulk modulus we find that these two effects on the lattice constants almost cancel. Also shown is the ^{57}Fe pDOS from an fcc $Fe_{0.70}Ni_{0.30}$

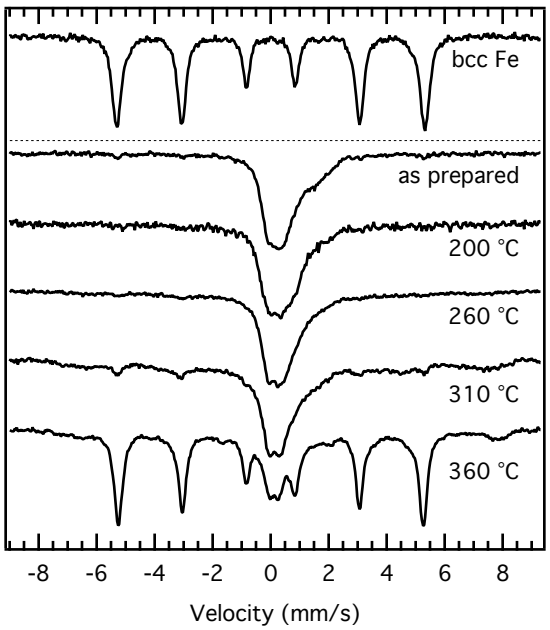

Figure 4.5: Mössbauer spectra from Cu-6% Fe in as-prepared state, and after annealing for 1 h at 200°C, 260°C, 310°C, and 360°C.

alloy measured by Lucas et al. [6], which is similar in features and energies. The bcc Fe DOS was obtained by NRIXS measurements on an ^{57}Fe foil.

The partial phonon density of states (pDOS) curve of the as-prepared material in black in Fig. 4.6 shows features reminiscent of a nanocrystalline material. Compared to the DOS of pure bcc Fe or fcc Fe, there is an enhancement of the DOS at energies below 15 meV. There is also some broadening of spectral features (in particular the longitudinal peak at 36 meV), and additional intensity above the peak of the longitudinal modes. The enhancement of the low energy modes is significant, and is highlighted in Fig. 4.7 with a log scale to show the deviation from the bcc bulk behavior (dashed line). After annealing at 360°C, a peak at 36 meV has clearly emerged, characteristic of the longitudinal peak from bcc Fe. At intermediate annealing temperatures, there is a decrease in the intensity of modes at low energies. This trend is well-documented in studies of compacted nanocrystals [42, 43, 55, 32, 30, 33]. The iron contribution to the vibrational entropy of Eq. 4.2 changes with annealing, as calculated from the pDOS curves of Fig. 4.6 using Eq. 4.2, and plotted in Fig. 4.8.

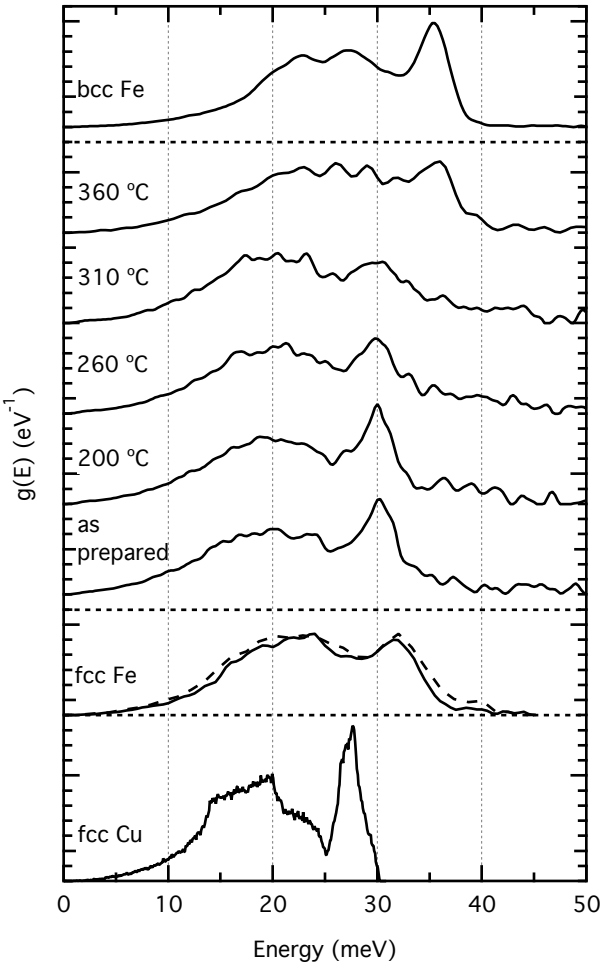

Figure 4.6: ^{57}Fe pDOS curves from NRIXS spectra of Cu-6% Fe in the as-prepared state, and after annealing at four different temperatures for 1 hour. Bulk bcc Fe measured with NRIXS is shown for reference along with fcc Cu. Two curves for fcc Fe are also shown: the black curve from $Ni_{0.30}Fe_{0.70}$ [6], and the dashed curve from fcc Fe at 6 GPa and 920K [7].

4.5 Discussion

4.5.1 As-Prepared Alloy

The fcc Cu-Fe system has a positive heat of mixing, and the equilibrium solubility of iron in fcc Cu is low, approximately 0.5% at 600°C, and even less at room temperature [56]. For a 6% concentration of iron in fcc Cu, the free energy is increased by approximately 1 kJ/mole over the pure elements [57]. This is not large, and extended solid solutions of iron in copper can be prepared by a number of methods, including the high-energy ball milling used here. The defect enthalpy of ball milling has been measured by calorimetry to be approximately 0.5 kJ/mole [57], and the change in crystal size and strains in the present work are consistent with reduction of defect enthalpy during annealing. The Mössbauer spectrum of this material is dominated by a single paramagnetic peak. The as-prepared material is a solid solution with fairly good mixing at the atomic level, as also shown by APT.

From Fig. 4.6, the ^{57}Fe pDOS of the as-prepared fcc Cu-6%Fe is between that of fcc Cu and other examples of fcc Fe. All are scaled to lower energies than the DOS of bcc Fe. These trends are easiest to see for the peaks from the longitudinal modes, which are at 30 meV for the as-prepared material, 32 meV for the fcc Fe, and 27.5 meV for the fcc Cu curve. This peak and the Van Hove singularities from transverse modes at approximately 14 and 24 meV in the as-prepared material all show similar compositional trends for the fcc phases. The mass difference between iron and copper accounts for a 7% shift in vibrational frequencies through the expected dependence on the square-root of the mass. This accounts well for the difference in the Fe pDOS in the as-prepared Cu-6%Fe fcc material and the DOS in fcc Cu. It might be more appropriate to compare to the phonon DOS of Cu in the as-prepared material, but the lattice parameter of the as-prepared material is less than 0.2% larger than that of fcc Cu, and with a Grüneisen parameter of 2, we expect a shift of phonon frequencies of only about 1 % for this small change in volume.

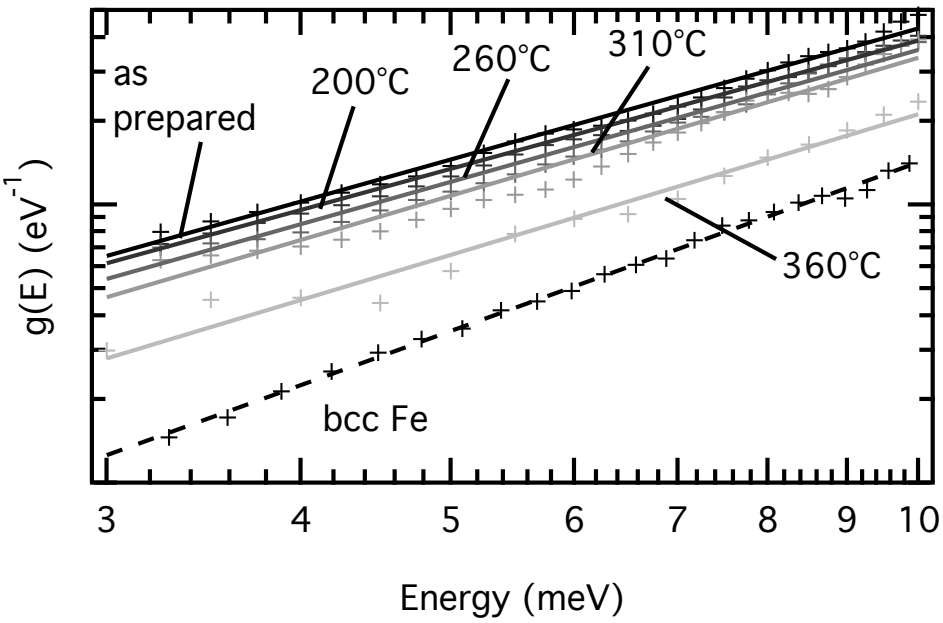

Figure 4.7: The ^{57}Fe pDOS curves from Fig. 4.6, examining only the low-energy region. As-prepared Cu-6% Fe is shown in black, and increasing annealing temperatures of 200°C, 260°C, 310°C, and 360°C are labeled. The dashed curve shows bulk bcc Fe for reference. Fits to the data are power-law functions, discussed in the text.

4.5.2 Changes in Nanostructure During Annealing

The APT results show that the composition modulations in the material annealed at low temperature give way to larger compositional heterogeneities at higher annealing temperatures. After annealing at 260°C, it appears that the iron atoms are still well-mixed in the fcc Cu matrix, with no strong segregations of iron atoms, as seen in the 2-dimensional representation of Fig. 4.4. Iron-rich regions begin to form at 310°C, the temperature at which the Mössbauer spectrometry begins to show growth of the ferromagnetic sextet. The fractional area of this ferromagnetic bcc iron, which is absent below 260°C, grows from 10% at 310°C to 73% to 360°C. At 360°C, the XRD also shows clear evidence of bcc iron. The APT measurements indicated that even at the highest annealing temperature, many iron-rich regions never fully exclude copper atoms. After annealing at 360°C, the Mössbauer spectrum shows a paramagnetic peak, consistent with about 27% of the iron atoms remaining in the Cu matrix (which would have a composition of about 0.6%Fe).

With increasing annealing temperature, Rietveld refinements of the diffraction patterns reveal an increasing crystal size from less than 18 nm to 25 nm, and a decrease in lattice strain by approximately 0.25%. The lattice parameter of the copper decreases gradually with increasing annealing temperature, an indication that iron atoms are diffusing out of the copper crystallites, allowing the copper unit cell to relax. Both the lattice parameter and lattice strain do not reach that of pure copper after annealing at 360°C, indicating that the unmixing transformation is not complete.

The ^{57}Fe pDOS undergoes no obvious change after annealing at 200°C, but there is a broadening of the longitudinal peak after annealing at 260°C, and this is more prominent at 310°C. This broadening is similar to that found in nanostructures, but the cause of this broadening has been controversial, as is addressed later in this discussion. It may be associated with phonon lifetime broadening owing to anharmonicity [58, 59, 60], or perhaps a distribution of high-energy modes that reflect a distribution of environments for harmonic vibrations [61]. The symmetric nature of the broadening would tend to favor the former explanation, since the iron environments are locally irregular, as seen from the APT results. However, this is not direct evidence supporting anharmonicity.

With annealing of our as-prepared Cu-6%Fe material, however, Fig. 4.6 shows a reduction in the intensity of the phonon modes at energies below 15 meV. After annealing at 310°C, the longitudinal peak characteristic of bcc Fe begins to emerge at approximately 36 meV, and by 360°C, this peak is distinct. The considerable broadening of this peak in comparison with the pure bcc Fe phase probably originates with the nanostructured form of the bcc clusters, but may also indicate a distribution of environments for the iron atoms. The Mössbauer spectra at 310°C and 360°C confirm these changes in the magnetic environment of the iron as the six-line splitting of bcc Fe emerges after annealing at 310°C and 360°C.

4.5.3 Vibrational Entropy of Unmixing

Obtaining the total vibrational entropy requires an accurate phonon DOS or accurate pDOS curves for both the copper and the iron, as seen in Eq. 4.2. We assume the pDOS from the majority copper atoms, $g_{\mathrm{Cu}}(\varepsilon)$, to be similar to the phonon DOS of fcc Cu. This assumption seems reasonable, because the pDOS of iron atoms in as-prepared material has the same shape as that of fcc Cu, as expected for a virtual fcc crystal. The assumption should be increasingly reliable as the iron atoms leave the Cu matrix. We can therefore focus on the pDOS of the iron atoms for describing the overall trends. In the as-prepared material, S_{vib} is 3.65 k_{B} per Fe atom compared with 3.96 k_{B} per Cu atom for fcc Cu, and 3.5142 k_{B} per Fe atom for the Fe-Ni system. These data, and the evolution of S_{vib} with annealing and unmixing, are shown in Fig. 4.8. For higher annealing temperatures, there is a gradual decrease in $\mathrm{S_{vib}}$. At 360°C, when the bcc Fe DOS is dominant, a larger decrease in S_{vib} is observed, with the S_{vib} of the 360°C material decreasing to 3.28 k_{B} per Fe atom, close to the 3.15 k_{B} per Fe atom for bcc Fe.

The ^{57}Fe pDOS in the as-prepared material probably originates with the dynamics of iron atoms having zero or a few Fe first-nearest neighbors (1nn) in the fcc lattice. For a random alloy, the probability of n 1nn Fe atoms on 12 sites for an alloy composition c is the binomial probability

$$P(n, 12, c) = \frac{12!}{n!\,(12-n)!}\; c^n\,(1-c)^{12-n}\;. \tag{4.4}$$

For $c = 0.06$, $P(n, 12, 0.06)$ evaluates to 0.48, 0.36, 0.13 for n equal to 0, 1, 2, respectively. As unmixing begins and the iron atoms form iron-rich zones separate from the copper, the majority region has fewer iron neighbors, and the iron atoms have a more heterogeneous chemical environment. This may be responsible for the broadening of the features in the Fe pDOS in the early stages of unmixing, when the bcc phase is not yet detected. This broadening does not cause significant overall shifts of the vibrational frequencies, however, so the vibrational entropy is little changed during this early stage of unmixing.

The large change in vibrational entropy occurs later upon the formation of the iron-rich bcc phase. The appearance of a longitudinal peak at 36 meV, a shift by a factor of 1.2 from the 30 meV in the fcc material, is approximately consistent with the shifts of other features in the phonon DOS. If we rescale the energy in Eq. 4.2 by a factor of 1.2 for the Fe pDOS, we obtain a change in vibrational entropy of $3k_B \ln(1.2) = 0.546\, k_B$/Fe atom in the high-temperature limit, which is an overestimate of the change shown in Fig. 4.8. With further unmixing and the growth of the bcc Fe zones, we expect a sharpening of features of the Fe DOS, but this sharpening is not expected to redistribute the average energies of phonons, and is therefore not expected to cause major changes in the vibrational entropy. We note that the decrease of S_{vib} with unmixing has the same trend as the configurational entropy, S_{cfg}, but it is smaller, being $0.4\, k_B$/Fe atom, or $0.024\, k_B$/atom for all atoms in the alloy (compared to an upper bound of $0.23 k_B$/atom for S_{cfg} in an alloy of 6% solute).

4.5.4 Vibrations in Nanocrystals

The phonon spectra in the early stages of unmixing show a broadening of peaks in the spectrum, a characteristic feature of nanocrystalline materials [43, 55, 32, 30, 33]. After annealing at 310°C, the longitudinal peak characteristic of bcc Fe begins to emerge at approximately 36 meV, and by 360°C, this peak is distinct. The considerable broadening of this peak in comparison with the pure bcc Fe phase probably originates with the nanostructured form of the bcc clusters, but may also indicate a distribution of environments for the iron atoms. The Mössbauer spectra at 310 and 360°C confirm these changes in the magnetic environment of the iron as the six-line splitting of bcc Fe emerges

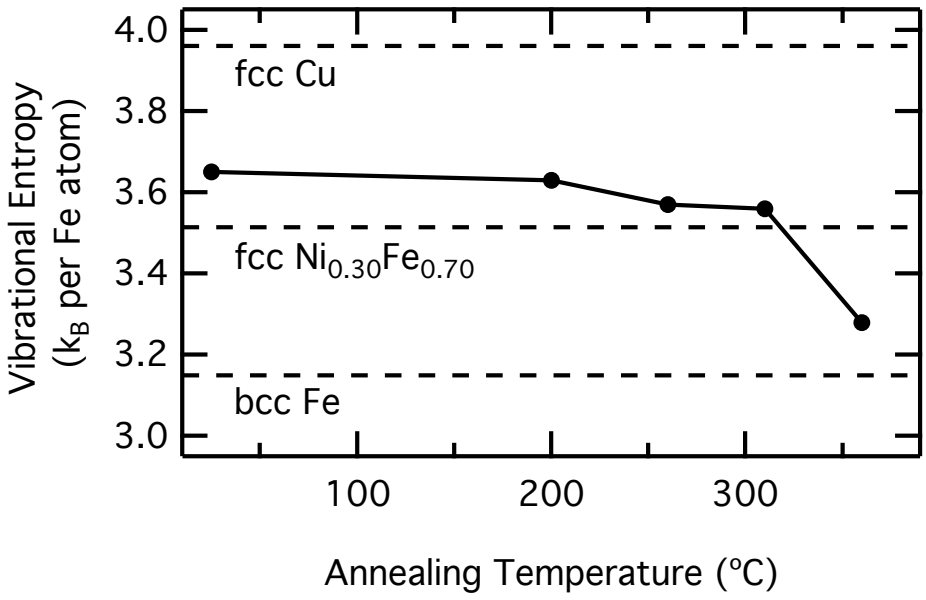

Figure 4.8: The partial vibrational entropy of ^{57}Fe atoms, calculated from the ^{57}Fe pDOS curves of Fig. 4.6. Dashed lines show bulk bcc Fe, fcc Cu, and fcc $Ni_{0.30}Fe_{0.70}$ at 25°C for reference.

after annealing at 310°C and 360°C. Although we may attribute the broadening to the distribution of iron environments as with Eq. 4.4, it could also be related to damping of phonons caused by anharmonic potential in a heterogeneous material. Such damping does not shift the average phonon frequencies, and does not affect the vibrational entropy substantially. If anharmonic damping is present, however, it will suppress thermal transport in materials with partial chemical unmixing.

With annealing of our as-prepared Cu-6%Fe material, however, Fig. 4.6 shows a reduction in the intensity of the phonon modes at energies below 15 meV. This low-energy mode enhancement is commonly observed in studies of nanostructures, and seems to be related to the dynamics of the structure itself. We find in the present work that the annealing reduces the intensity of modes at low energy, however, probably because the annealing induces both spatially-larger iron heterogeneities and grain growth. The low-energy modes are apparently dependent more on grain size than on chemical heterogeneities in the material. The as-prepared material, which appears to be a solid solution of iron in fcc Cu, has the smallest crystal size and the largest spectral intensity at low energies. The low-energy region from 3 to 10 meV was fit with a power function expression $g(\varepsilon)$

$\propto \varepsilon^n$, as shown in Fig. 4.7. Exponents n were found to be 1.50, 1.52, 1.57, 1.64, 1.68, and 2.00 for the as-prepared material, 200°C, 260°C, 310°C, 360°C, and bcc Fe, respectively. This may be interpreted as a change in the dimensionality [39] from 2.5 for the as-prepared material to 2.68 in the material annealed at 360°C. However, the APT results show no obvious trend indicating a reduced dimensionality.

4.6 Conclusions

Chemical unmixing in an fcc nanocrystalline solid solution of 6% Fe in Cu was followed in near-atomic detail by three-dimensional atom probe microscopy (APT), and its crystal structure was monitored by x-ray diffractometry. The unmixing was heterogeneous, with iron atoms forming iron-rich zones that may thicken with further annealing. The phonon partial density of states (pDOS) of ^{57}Fe was measured by nuclear resonant inelastic x-ray scattering (NRIXS) at various states of unmixing. The pDOS of the as-prepared material was similar to the DOS of fcc Cu, but approximately rescaled to higher energies for the mass difference of iron and copper atoms.

The overall changes in phonon frequencies and vibrational entropy were found to be small until the bcc phase began to form, when the vibrational entropy calculated from the pDOS approached that of bcc iron. The features of this pDOS became broader in the early stages of unmixing, a characteritic common to the study of nanocrystals. It most likely results from chemical heterogeneities, or perhaps owing to phonon damping caused by anharmonic potentials. Enhancement of low-energy modes, a feature commonly observed in the phonon spectra of nanomaterials, was also observed and fitting of the expression for the phonon densitities of states $g(\varepsilon) \propto \varepsilon^n$ yielded exponents n as small as 1.5 for the as-prepared material. However, the atom maps obtained from APT provide a compelling indication that there is no trend of reduced dimensionality present.

Chapter 5

Changes in entropy through the glass transition in Cu-Zr

5.1 Introduction

The atomic structure and dynamics of liquids and glasses are much less understood today than the properties of crystalline solids. First-principles theories have answered many questions about crystalline materials and can even be used to make predictions of phonons, for example. These successes are owed to the ability of translational symmetry and Blochs theorem to provide detailed descriptions of crystalline solids. However, this approach fails immediately when used to describe the complex many-body interactions in liquids and glasses [62]. Thus, the nature of amorphous materials and the glass transition remains one of the most challenging problems in solid state physics [63].

The glassy state is ubiquitous in nature and technology [64]. Window glass is the most widely-known glass, composed of sand (SiO_2), lime ($CaCO_3$), and soda (Na_2CO_3)[1]. The term 'glass' encompasses any solid that possesses a non-crystalline structure and exhibits a glass transition when heated towards the liquid state. However, metallic glasses are quite distinct in their physical properties from other types of glasses. Metallic glasses are much tougher than oxide glasses and ceramics, and also tend to have higher tensile yield strengths and higher elastic strain limits than polycrystalline metal alloys [66].

[1] Many who recognize the amorphous nature of window glass also fall prey to the common myth that the liquid-like structure of window glass can be seen in the thickness variation of stained glass windows in old cathedrals. In fact, solving the Volger-Fulcher-Tamman expression for the viscosity as a function of temperature yields a relaxation time on the order of 10^{32} years, which is well beyond the age of the universe [65].

The glass transition is unique to materials that are in an amorphous state at temperatures below the crystallization temperature of the material. Over a narrow temperature range immediately below the crystallization temperature, the solid amorphous material softens, becoming a viscous liquid that is deeply undercooled below the usual melting temperature. One of the most intriguing aspects of the glass transition is that the atomic structure of the supercooled liquid does not change significantly across the transition, while the transport properties such as viscosity change by more than ten orders of magnitude [67, 68, 69, 70].

The glass transition can be regarded as a kinetic phenomenon in which the rapidly-increasing time scale for structural equilibration of the supercooling liquid crosses the time scale of the experimental tools used to study the material [67]. When a liquid is cooled, its molar volume, enthalpy, and entropy decrease, and there is a concomitant increase in its viscosity and relaxation time. Fig. 5.1 illustrates the temperature dependence of a liquid's volume (or enthalpy) at constant pressure. Upon cooling below the freezing point T_m, atomic motion slows down. If the liquid is cooled sufficiently fast, crystallization can be avoided. Eventually, atoms will rearrange so slowly that they cannot adequately sample configurations in the available time allowed by the cooling rate. The liquids structure therefore appears 'frozen on the laboratory timescale (for example, minutes). This falling out of equilibrium occurs across a narrow transformation range where the characteristic atomic relaxation time becomes of the order of 100 seconds, and the rate of change of volume or enthalpy with respect to temperature decreases abruptly (but continuously) to a value comparable to that of a crystalline solid. The resulting material is a glass. The behavior depicted in Fig. 5.1 is not a true phase transition, as it does not agree with Ehrenfest's requirement that a discontinuity be observed in a derivative of the Gibbs free energy with respect to some thermodynamic variable.

The observed behaviors indicate that changes in V, H, and S may be quantitatively related to changes in both the phonon properties and atomic configurational dynamics. Relations between the frequency of vibrational modes and the heat capacity are understood in terms of the Debye Einstein theory and Grüneisen parameters, and these relations are usually regarded as satisfactory for most solids. It may be expected that both the free volume and S_{exc} of a liquid would have additional

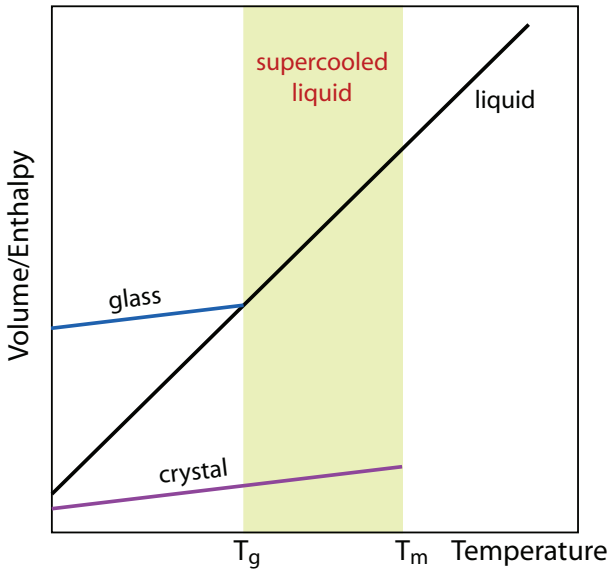

Figure 5.1: Temperature dependence of a liquid's volume or enthalpy at a constant pressure. T_m is the melting temperature. For glasses that are cooled sufficiently quickly, the liquid enters the supercooled liquid regime before atomic motions become 'frozen' on the laboratory time scale, resulting in the glass with a higher volume and enthalpy and volume than its corresponding crystal.

contributions from atomic vibrations and associated anharmonic forces, and that these contributions would decrease on cooling. However, the significance of these additional contributions is generally neglected in both free volume and entropy theories. These contributions to heat capacity and entropy can be described qualitatively in terms of potential energy landscape theory [71] or inherent state model [72]. This leads to an insight into the interdependence of the configurational and vibrational contributions to C_p and entropy of an equilibrium liquid. Measurements of the total heat capacity, including both of these entropy contributions, are made routinely [73, 74]. However, a definitive measurement of either the total configurational or vibrational entropy contribution has not been made.

The configurational entropy model of Adam and Gibbs [75] hypothesizes that the progressively increasing size of the cooperatively rearranging regions and decreasing configurational entropy in a liquid as temperature decreases is responsible for the apparently diverging relaxation times and viscosity. The transition from the glassy state to the supercooled liquid state is accompanied by a positive jump in heat capacity in this narrow range of temperature defined as the glass transition

temperature.

Their theory yielded the quantitative expression

$$\eta = \eta_{\circ}\exp(\mathrm{C}/\mathrm{TS_c}), \tag{5.1}$$

which connects the viscosity η with the configurational entropy S_C, where C is a constant containing a free enthalpy barrier to cooperative rearrangements, and T is temperature.

Vibrational entropy is noticeably absent in Adam-Gibbs theory, as the excess entropy associated with the jump in heat capacity is assumed to be caused entirely by the configurational entropy. However, this assumption has not been tested experimentally, and there is no *a priori* reason to believe that that this is the case. Understanding of the contribution of the vibrational entropy to the excess entropy of the supercooled liquid plays a critical role in building a quantitative description [76, 77, 78, 79, 80].

5.2 Present Work

This study presents the first experimental determination of the change in vibrational entropy through the glass transition for a metallic glass. Inelastic neutron scattering was used to obtain the phonon density of states at temperatures from 300 to 823K for equiatomic amorphous CuZr. The vibrational entropy results from integration of phonon density of states over narrow temperature intervals during continuous heating through the glass transition. The temperature for the onset of the glass transition and the subsequent crystallization is predicted from differential scanning calorimetry performed at the same rate. These temperatures are confirmed by elastic scattering obtained during the neutron scattering measurement that shows the emergence of diffraction intensities at the expected temperature for crystallization.

The selection of the binary Cu-Zr alloy for this study is made for its simple structure and good glass-forming ability. Cu and Zr are also a good choice because of their similar efficiency for the

scattering of neutrons by phonons, which is proportional to the total scattering cross section divided by the molecular weight. These values are 0.1178 and 0.0708 for Cu and Zr, respectively; thus, the phonon DOS and resulting vibrational entropy will not be dominated by the large motions of one atom type over another.

5.3 Potential Energy Landscape Theory

Potential energy landscape theory provides a natural separation of low-temperature atomic motion into sampling distinct potential energy minima (i.e. configurational hopping) and vibration within a minimum (i.e. vibrational motion) [77]. This separation arises from the expression for the Helmholtz free energy for which there are three distinct components: (1) the energetic, reflecting the depth of landscape basins sampled preferentially at a given temperature, (2) the entropic, accounting for the number of existing basins of a given depth, and (3) the vibrational, describing thermal motions confined to a given basin. Minimization of the free-energy gives a basin enumeration function that is a statistical description of the landscape based on the assumption that all basins have the same mean curvature at their respective minima.

The attempt to characterize the viscous slow-down and jump in heat capacity that define the glass transition in amorphous materials has lead to the natural assumption that these changes in kinetic behavior are due solely to the exploration of different basins [75]. That is, the configurational entropy dominates, and the vibrational component from thermal motions confined to a given basin provides a negligible contribution to the total change in entropy through the glass transition. While this claim has foundation in the separation of the thermal motions within a basin from the exploration of numerous basins, it has not been supported experimentally, as no measurement of the change in vibrational entropy through the glass transition has been performed to date.

5.4 Related Work

There is extensive literature examining binary Cu-Zr metallic glasses, including some on phonons studied by inelastic neutron scattering [81, 82, 83], but there has been no attempt to determine the explicit contribution of vibrations to the excess entropy of the liquid over the crystal through the glass transition. Previous studies have been limited by the instrumentation required to obtain spectra in the short times available at temperatures above the glass transition before crystallization occurs. The power of the proton beam at the Spallation Neutron Source (SNS) has recently surpassed 1 MW, allowing spectrum acquisition on the ARCS spectrometer in a few minutes [84]. Additionally, the SNS uses a unique data collection method that provides flexibility in post-processing data in a way that was not previously possible (see Section 5.5.2.2).

Other previous attempts to characterize the vibrational entropy contribution have suggested a non-trivial contribution of vibrations to the excess entropy of the liquid over the crystal through the glass transition. A Raman spectroscopy study of a chalcogenide glass suggested that vibrations contribute as much as 20% to the total excess entropy of the liquid in comparison to the crystal, but very few of the Raman-active vibrational modes were explored [85]. Neutron scattering measurements of glassy and liquid selenium estimate one-third of the additional entropy to be vibrational [86]. Phillips et al. cite agreement with estimates made from Goldstein based on a comparison of quenched and annealed glasses, including selenium [87, 88]. However, Goldstein does not measure the vibrations directly, instead arguing that it is possible to quantify the changes in vibrational frequencies and anharmonicities on the basis of changes in heat capacity near 0K̇. Heat capacity measurements are performed on two samples of glass of identical composition, but produced in different structural states by altering their thermal histories. Based on a large variation in the fraction of the entropy difference at the glass transition still present near 0 K, he concludes that up to half of the excess entropy of the liquid over the crystal comes from anharmonicity and vibrational entropy.

The velocity of sound has been measured through the glass transition of alloys of excellent glass forming ability, $Zr_{46.25}Ti_{8.25}Cu_{7.5}Ni_{10}Be_{27.5}$ and $Pd_{43}Ni_{10}Cu_{27}P_{20}$ [89, 90]. It was found that the shear and bulk moduli decreased by approximately 7 and 4 percent, respectively, giving an

approximate change in vibrational frequency at long wavelengths of 3%. In the high temperature limit, this corresponds to a change in vibrational entropy of $\Delta S = 3\ln(1.03) = 0.09 k_B$/atom, a small contribution. However, the vibrational entropy is often dominated by changes in the more numerous phonon modes at higher frequency, and these typically do not scale with the trends at long wavelength.

The measurements presented here differ from previous experimental work in three important ways: (1) $Cu_{50}Zr_{50}$ is a metallic glass, (2) the measurements were performed on all vibrational modes using neutron scattering, and (3) the measurements were performed *insitu*. Previous estimates of vibrational contributions to the excess entropy at the glass transition have not been made for metallic glasses (as far as we are aware). Neutron scattering provides an excellent probe of the phonons in materials and gives direct access to the vibrational entropy through measurement of the phonon density of states. However, previous reports estimates of the vibrational contribution have come from heat capacity measurements which give an indirect estimate by measuring near 0 K where vibrations are 'frozen out.' Finally, other reports of *insitu* measurements have not studied all of the vibrational modes in the material. While Raman spectroscopy is capable of giving detailed information about the behavior of vibrational modes as a function of temperature, it is limited to only Raman-active modes, and does not provide a complete phonon density of states.

5.5 Vibrational Entropy from Neutron Scattering

5.5.1 Experimental

5.5.1.1 Sample Preparation and Characterization

Copper and zirconium were arc-melted to form the binary alloy, then vacuum-cast. Fig. 5.2 shows the samples as cast. The casting mold featured a 1 mm thick plate at the bottom, and 2 mm thick plate at the top. The bottom sections 5 mm by 13 mm and 1 mm in thickness were amorphous, and these sections were separated and used for neutron scattering experiments. The samples were arranged in an 5 x 4 array approximately 52 mm by 25 mm by placing 5 plates each into a foil

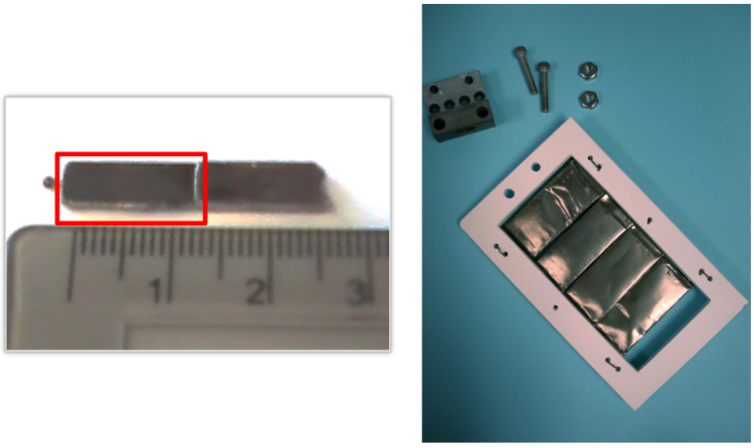

Figure 5.2: (Left) Samples were cast from a two-stage mold that produced plates 1 mm in thickness (outlined in red), which were cut apart and used for the experiments. (Right) For scattering experiments, the plates were wrapped in 4 individual foil packets, each containing 5 plates, and fixed to a BN absorbing frame. This frame was attached to the sample stick with the clip, screws, and bolts.

packet, and fixing 4 foil packets to a BN absorbing frame, as shown in Fig. 5.2.[2]

To confirm that the amorphous phase was achieved, X-ray diffraction and differential scanning calorimetry were performed. A representative DSC scan performed at 20K per min is shown in Fig. 5.3. The inflection of the glass transition, T_g, is indicated by a small rise followed immediately by the endothermic crystallization peak. The units given are endothermic heat flow, which can be converted to heat capacity. This is performed and discussed in great detail in Appendix B. This scan was performed at a faster heating rate than the neutron scattering measurement, so it confirms that the samples are fully amorphous, but does not provide accurate temperatures for the onset of the glass transition and crystallization. Additional scans were performed at a heating rate matching the experimental condition.

5.5.1.2 Data Collection

Inelastic neutron scattering (INS) measurements were performed with ARCS, a time-of-flight Fermi chopper spectrometer at the Spallation Neutron Source at Oak Ridge National Laboratory. The sample thickness of 1.0 mm gives a ratio of multiply to singly-scattered neutrons of approximately

[2]The photo shows the sample configuration for measurements in the high-temperature MICAS furnace. The data presented here are from the low-temperature stick furnace. The sample configuration was nearly identical, except that aluminum foil and wire was used instead of the Nb foil and wire shown here.

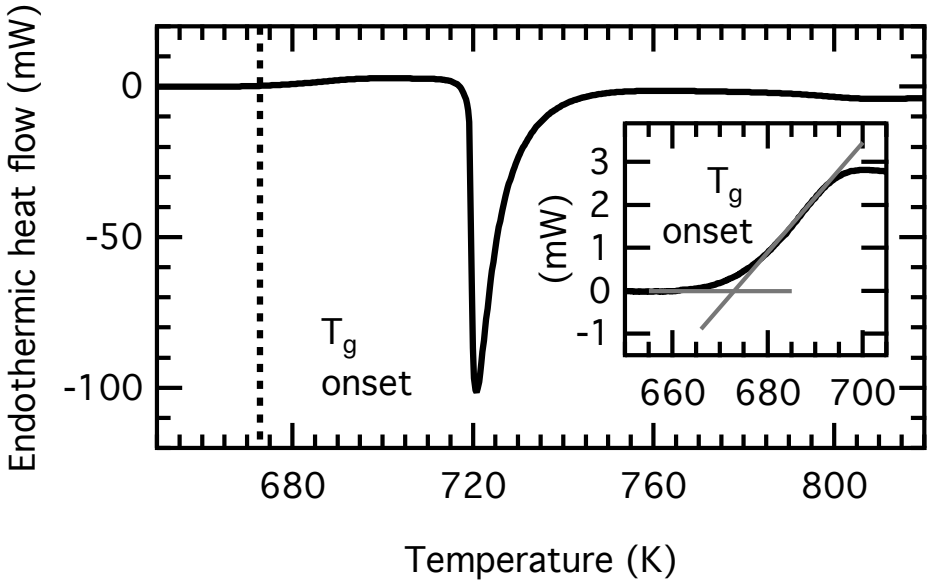

Figure 5.3: DSC of the amorphous alloy shows the endothermic heat flow as a function of temperature. The glass transition is indicated by the rise in heat capacity before the sharp endothermic peak of crystallization. The inset shows the glass transition in more detail with common tangent lines indicating how the temperature of the onset of T_g is determined.

5%. The measurements were performed with a monochromatic beam of neutrons with an incident energy of 80 meV.

The furnace, referred to as a 'stick furnace,' is a low-mass electrical resistance furnace designed so that all components in the neutron beam are aluminum. In addition to the sample and sample holder, a cylinder of aluminum foil is placed around the sample. The temperature was monitored by several thermocouples giving agreement within 5K over the sample. The glass sample was measured at room temperature, and then continuously heated at 2K per min up to 734K, where the temperature was maintained for 30 min. The sample was then cooled to 600K and re-measured, then cooled to room temperature.

Background measurements were acquired under identical experimental conditions. The sample was removed and replaced with sheets of aluminum foil to simulate the sample holder. For final extraction of the densities of states, the background is reduced identically, and 90% of the background contribution is removed from the measurements of the sample. Data reduction was performed with

the software package DRCS [91] for ARCS, for which details are described elsewhere [92].

Data acquisition was performed in 0.1 pC runs. This is a unit of proton charge that is counted by a beam monitor before the sample. The time required to acquire a given proton charge depends on the power of the accelerator at the time of the measurement. For these measurements, beam power was stable at ∼850 kW, and each run averaged 2 minutes to acquire 0.1 pC. Acquiring the data in these intervals provided additional flexibility for post-processing the data. With a heating rate of 2K/ min, each run contained an approximate 4K change in temperature. As is presented in the results section, the data were analyzed in several ways by using as few as one run of data and as many as six runs to compare the effect of averaging over smaller or larger temperature bins.

5.5.2 Results

5.5.2.1 Diffraction

Fig. 5.4 compares the $S(Q, E)$ for the amorphous and crystalline material at 600K. Integrating the neutron scattering intensity around the elastic peak from -2 to +2 meV provides diffraction patterns, shown in Fig. 5.4. Background contributions from the sample environment were not subtracted here, so the scattering from the aluminum sample environment and sample holder are present. This contribution is indicated by the positions for Al powder diffraction overlaid on the plots.

The elastic scattering, together with DSC performed at the same heating rate as the INS measurements, can be used to determine where the glass transition occurred under these conditions. Fig. 5.5 shows the diffraction from the total elastic scattering (sample and sample environment) integrated over a 10K change in temperature between 605K and 733K. The sample is amorphous at 605K, so the diffraction peaks are entirely from the aluminum sample environment. The diffractions from the sample environment remain relatively constant with temperature, with changes becoming visible at the highest two temperatures. A region from 3 to 5 Å in Q in the inset of Fig. 5.5 highlights the onset of crystallization at 725K, and complete crystallization at 733K.

Fig. 5.6 also shows the diffraction over the same temperature range, with diffraction from the total elastic scattering subtracted at 575K subtracted from each of the diffraction patterns. This also

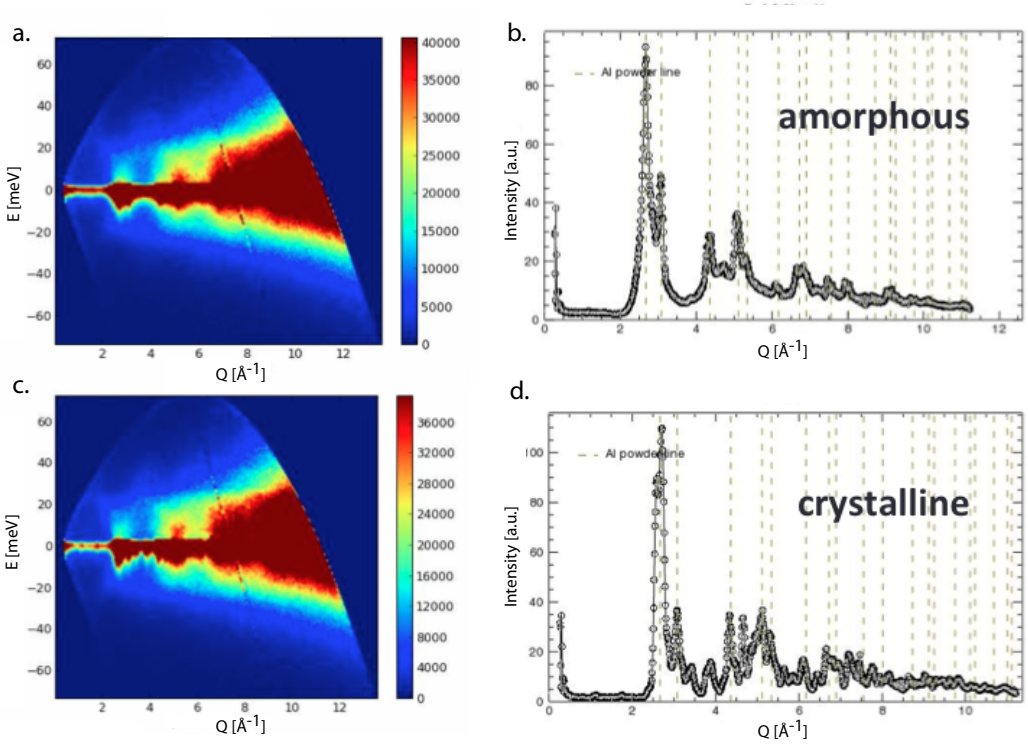

Figure 5.4: (a) and (c) $S(Q, E)$ for the amorphous material and crystalline material at 600K. (b) and (d) The elastic scattering obtained from integrating over E from -2 to +2 meV. Powder diffraction lines from aluminum are overlaid on the diffraction to show the contribution from the sample environment and sample holder to the elastic scattering.

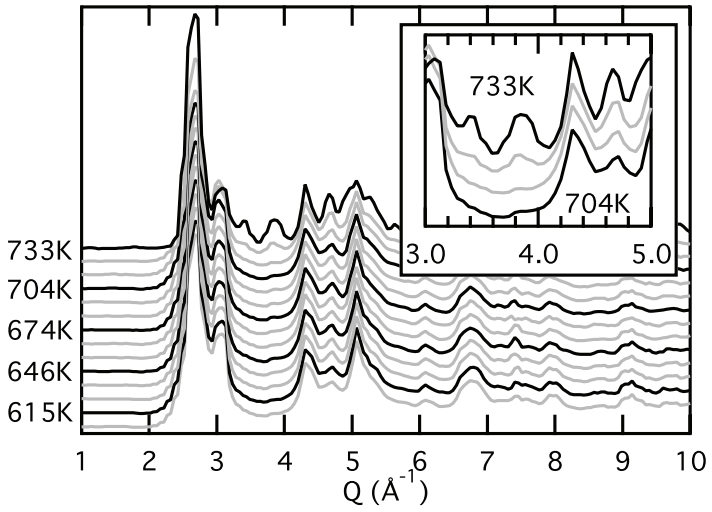

Figure 5.5: Diffraction from elastic scattering plotted as a function of momentum transfer Q from continuous heating of CuZr from the amorphous state at 610K through the glass transition and above crystallization at 715K. Background was not subtracted from the elastic scattering; thus, diffraction peaks below the crystallization temperature of the glass are due to the sample environment. The inset highlights the transition from the amorphous phase at 704K to complete crystallization at 733K.

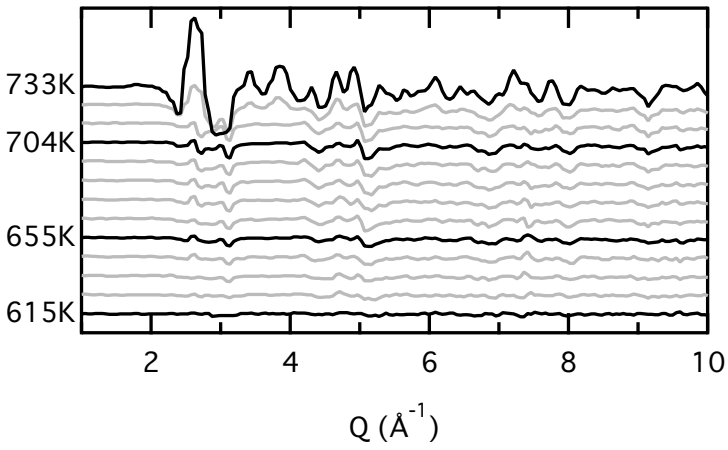

Figure 5.6: Diffraction patterns from Fig. 5.5 after subtracting the diffraction at 575K to highlight the onset of crystallization at 725K, becoming fully crystalline by 733K.

shows clearly the onset of crystallization at 725K, and the sample fully crystallized at the highest temperature.

5.5.2.2 Inelastic Scattering

The standard method for data collection at the SNS is referred to as 'event mode.' Event mode collection of scattering data provides each neutron event with a position and time stamp, and all processing and binning occurs later. This approach allows the data to be post-processed in several ways to compare the effect of binning over different temperature ranges. The software necessary to post-process data that takes advantage of this mode of data collection is not currently in place at most beamlines. ARCS has recently gained capabilities to perform some types of event-mode data reduction that allows a large run of data to be binned after collection according to a variable used during the measurement, such as sample temperature or angular sample position. This method of data collection is in contrast to standard histogram data collection, where detector events over a given time period are binned and it is not possible to extract individual neutron events from the bins.

Post-processing the data in several ways allowed us to ensure that effects through the glass transition would not be overlooked by examining data sets that averaged over effects through this narrow range. Fig. 5.7 shows $S(Q, E)$ plots obtained by binning data over 25K, 10K, and 4K ranges in temperature for the same average temperature, and plotted on the same intensity scale. Energy bins of 1 meV for all three temperature binnings are also compared to 3 meV energy bins for 4K temperature bins.

Corresponding with each $S(Q, E)$ plot in Fig. 5.7 is a plot of intensity as a function of energy summed over all Q. The raw intensity is multiplied the factor Λ:

$$\Lambda = [1 - (\exp(E/(k_{\mathrm{B}}T)))] \times (k_i/k_f)^4 \times E/Q^2, \tag{5.2}$$

where the momentum transfer to the sample, Q, is related to k, the magnitude of the incident and

scattered waves by the relation $Q = k_i - k_f$. This is a sort of density of states that does not follow the detailed procedures outlined in Chapter 1 for reduction to DOS and correction for multiphonon and multiple scattering. Most notably, the I vs. Q plots in Fig. 5.7 have a non-physical feature below 10 meV from the improper correction for the elastic scattering centered at 0 meV. However, it is employed here to demonstrate a raw comparison of the differences produced for each type of energy and temperature binning. Error bars are included in intensity which are derived from counting statistics[3].

Fig. 5.7 demonstrates that binning into larger temperature intervals of 25K produces the highest statistical quality results, and detailed features are apparent in the I vs. Q plot, such as a small inflection at 37 meV on the shoulder of the main peak. The $S(Q, E)$ is finely grained, with gradual changes in intensity to the highest energies. Increasing the temperature binning to 10K produces a sharper feature on the shoulder of the main peak, now shifted to slightly lower energy transfer, but the validity of this peak is more questionable due to the increase in statistical variation, especially at the highest intensities. The $S(Q, E)$ is more coarsely grained, as expected from a histogram from a fewer number of neutrons. Further decrease in temperature bins to 4K produce an $S(Q, E)$ that has considerably fewer statistics than the previous two plots. These data were acquired in 120 seconds of counting time at 850 mW, and probably indicate a lower bound for the minimum counting time to produce results of acceptable statistical quality. The I vs. Q plot produces a notch in the main peak around 19 meV that was not previously visible, and the errors in counting statistics increased considerably over the 10K temperature binning. Increasing the energy binning is a way to increase the histogram statistics, but also has a smoothing effect that could diminish sharp features. Given the broadness of the I vs. Q plot, this is not as much of a concern as in a spectrum with many sharp features. The final I vs. Q plot for 4K temperature bins and 3 meV energy bins thus improves considerably the counting statistics, even flattening the intensity at high energy. While it clearly produces a much coarser peak shape, the overall peak shape is in surprisingly good agreement with the I vs. Q plot for much larger 25K energy bins.

[3]It is obvious that these error bars don't derive from any sort of multiphonon or multiple scattering correction, because at the highest energies between 60 and 70 meV, the DOS does not go to zero, and the error bars do not indicate that it should.

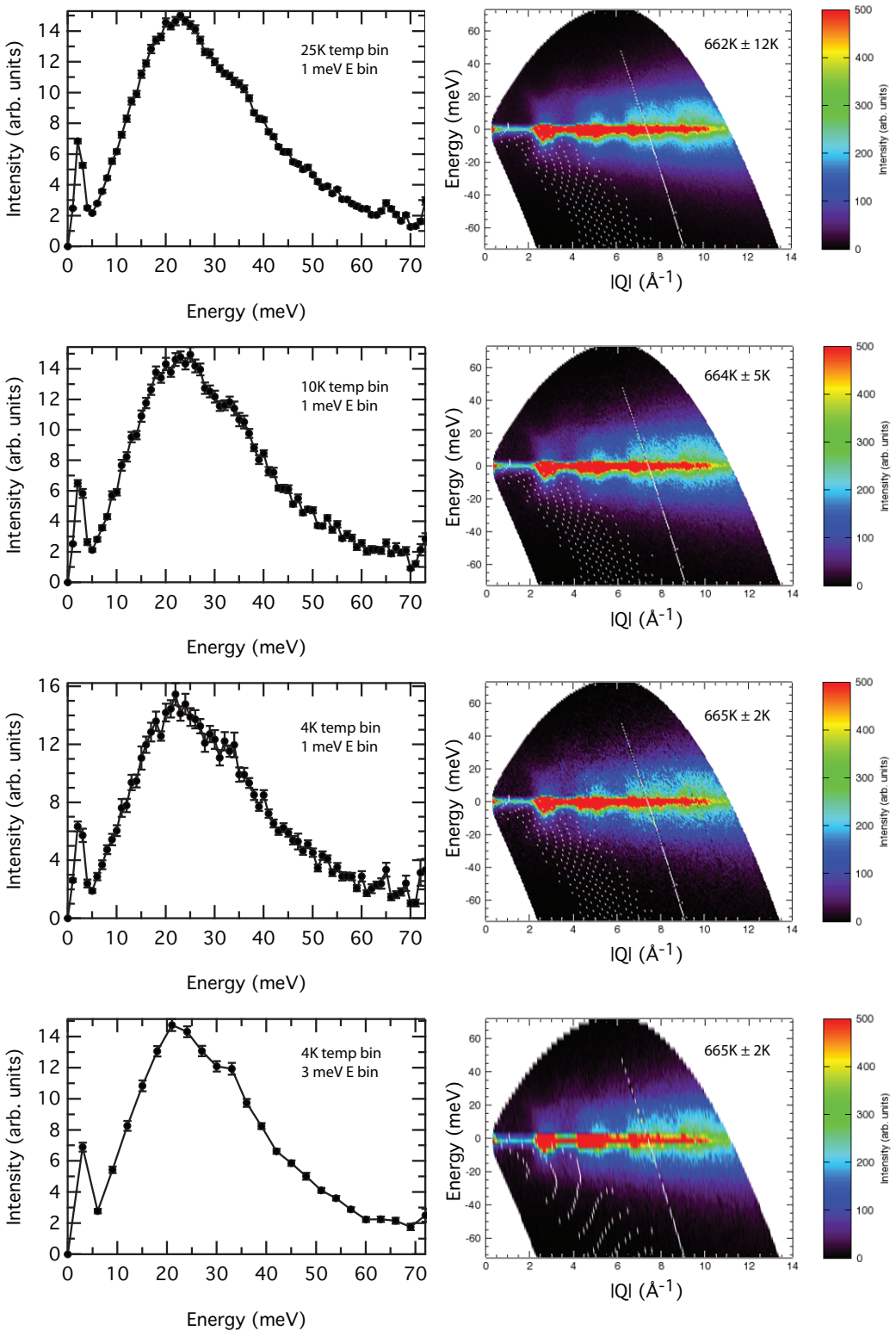

Figure 5.7: Comparison of the statistical quality of raw $S(Q, E)$ and I vs. Q plots for 3 different temperature bin sizes with 1 meV energy binning and the smallest temperature binning with larger energy binning. Each I vs. Q plot on the left corresponds to the $S(Q, E)$ plot on the right.

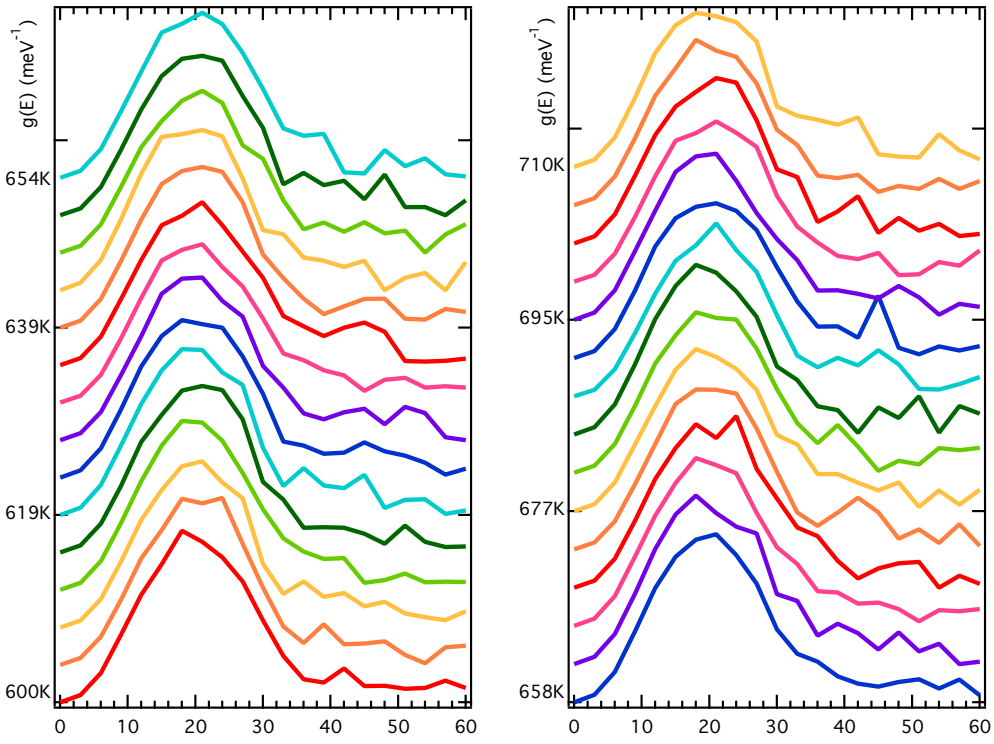

Figure 5.8: Phonon DOS for 4K temperature bins and 3 meV energy bins between 600K and 710K. Each spectrum was acquired in 120 seconds.

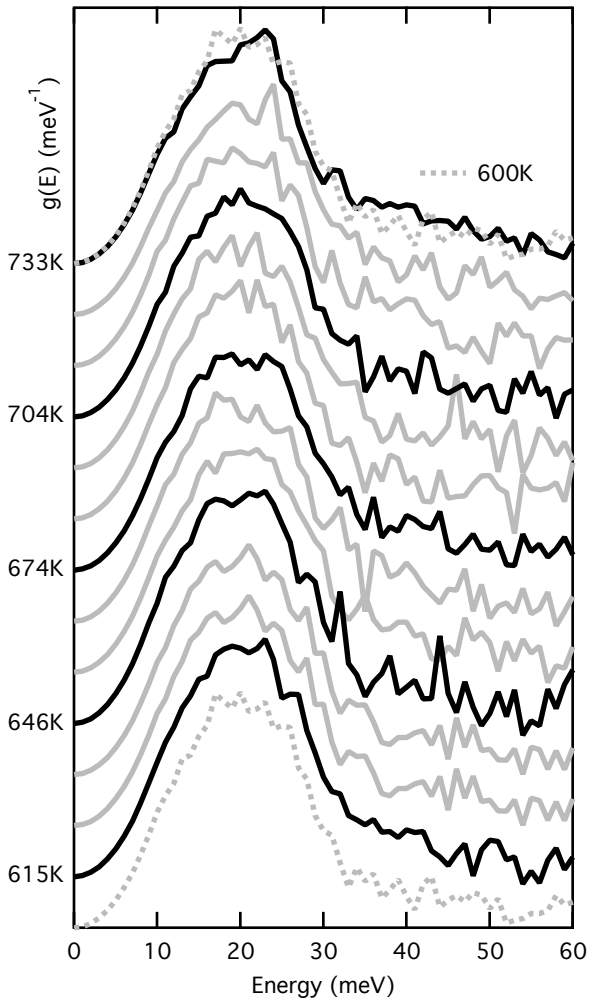

Figure 5.9: Phonon DOS for 10K temperature bins and 1 meV energy bins from heating of CuZr from the amorphous state at 600K through the glass transition and above crystallization at 715K. Each spectrum was acquired in 4-6 minutes. The amorphous 600K DOS (dashed grey) is shown also at high temperature, overlaid with the DOS of the crystalline material at 733K.

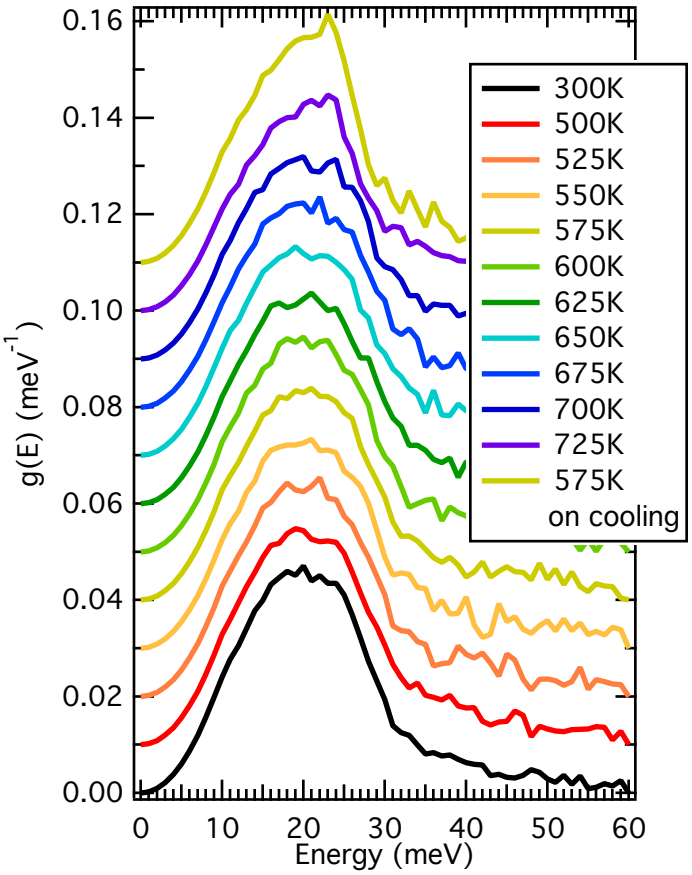

Figure 5.10: Phonon DOS curves for 25K temperature bins and 1 meV energy bins between 600K and 725K.

With consideration for these preliminary results, a full reduction to the DOS, including a correction for multiphonon and multiple scattering, was performed for 4K, 10K, and 25K temperature bins with energy binning of 1 meV, 1 meV, and 3 meV, respectively. Sets of DOS obtained with this temperature binning are shown in Figs. 5.8, 5.9, and 5.10 for 4K, 10K and 25K respectively.

The spectra in Fig. 5.9 provide perhaps the best compromise in statistical quality for the temperature bin size. These curves show little change over the temperature range shown. At the highest temperature, additional weight is visible in the peak at 23 meV. This clear change in the shape of the spectrum is an indication that the material has crystallized. Comparison with the temperature interval immediately below, at 715K, shows some indication of a change in the spectra intensity, though the statistical quality likely exaggerates this as a sharp peak.

The phonon entropy can be calculated from each of the DOS curves in Figs. 5.8, 5.9, and 5.10 using the following expression:

$$S_{\mathrm{vib}}(T) \quad = \quad 3k_{\mathrm{B}} \int_0^\infty g(E) \, \Big([1+n(T)] \ln[1+n(T)] \, n(T) \ln n(T) \Big) \, dE \; , \tag{5.3}$$

where $n(T) = (\exp(E/(k_{\mathrm{B}}T)) - 1)^{-1}$ is the Planck distribution for phonon occupancy. [93]

An expression for the high-temperature limit of the difference in vibrational entropy between two harmonic phases, α and β, can be obtained from Eq. 5.3

$$S_{\mathrm{vib}}^{\beta-\alpha} \quad = \quad 3k_{\mathrm{B}} \int_0^\infty (g^\alpha(E) - g^\beta(E)) \ln E \, dE. \; , \tag{5.4}$$

The phonon entropy calculated from each of the DOS curves using Eq. 5.3 is shown in in Fig. 5.11 as a function of the average temperature of the spectrum. The results are also tabulated in Table 5.1. The temperature of the onset of the glass transition T_g and crystallization T_{c1} are indicated in Fig. 5.11.

Table 5.1: Entropy values calculated using Eq. 5.3 for three different temperature binnings. These values are plotted in Fig. 5.11.

4K Binning		10K Binning		25K Binning	
Temperature (K)	Entropy (kB/atom)	Temperature (K)	Entropy (kB/atom)	Temperature (K)	Entropy (kB/atom)
601.0	8.78	605.7	8.80	590.0	8.78
604.7	8.82	615.0	8.84	613.4	8.79
608.5	8.83	624.7	8.80	639.4	8.80
612.3	8.87	636.1	8.83	664.0	8.83
616.0	8.83	646.0	8.81	688.4	8.82
619.9	8.79	655.5	8.82	713.8	8.83
623.8	8.76	664.8	8.84	730.9	8.85
627.8	8.78	674.2	8.87		
631.4	8.84	685.4	8.77		
635.1	8.85	694.7	8.76		
639.0	8.76	704.1	8.82		
643.1	8.77	714.9	8.91		
647.3	8.80	733.2	8.89		
650.9	8.85				
654.7	8.88				
658.3	8.77				
662.2	8.83				
665.8	8.83				
669.7	8.87				
673.5	8.83				
677.1	8.86				
680.8	8.86				
684.6	8.72				
688.4	8.83				
692.1	8.83				
695.7	8.78				
699.5	8.85				
703.2	8.87				
707.0	8.81				
710.7	8.87				

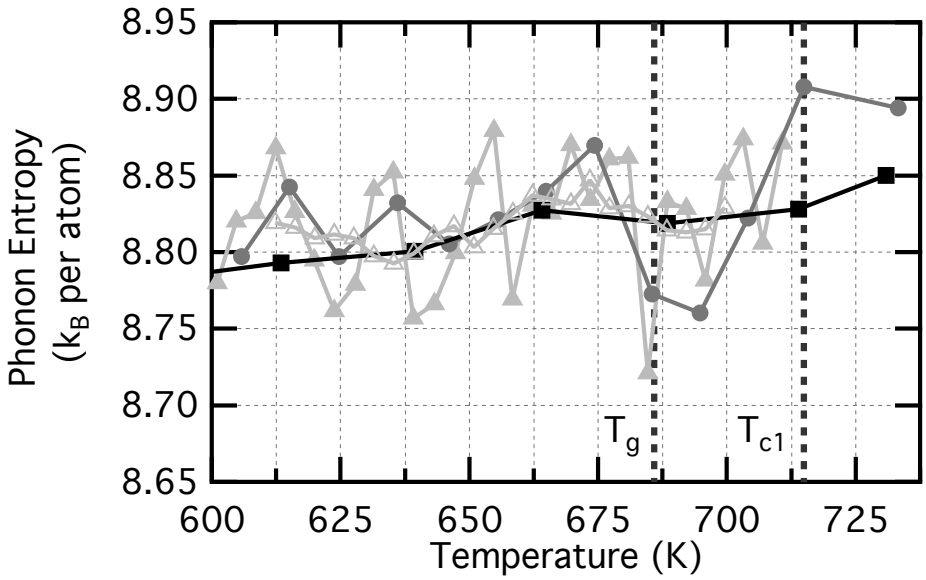

Figure 5.11: The vibrational entropy is calculated from the DOS curve and plotted for temperature bins of 25K (black squares), 10K (gray circles), 4K (light gray triangles), and a 6-point running average of 4K (open light gray triangles). Vertical lines indicate the temperature at which the T_g inflection and T_{c1} peak are observed at this heating rate.

5.5.3 Discussion

The disordered structure of a metallic glass has the implication that the energies of interaction between atoms will generally be very complicated. The part of configuration space explored by the material in the amorphous state is characterized by the presence of many local minima of the potential energy. This potential energy landscape approach to describe the complicated interactions in a metallic glass decomposes the traditional 3N dimensional configuration space into basins of individual local potential energy minima [71, 72]. Each basin is a minimum defined by sets of points in the configuration space. Thus, the configurational entropy is characterized in this approach by the number density of basins with a given energy, and the vibrational entropy is the curvature of the basin. The concerted movement of the system between basins to a new configuration would then provide a contribution of configurational entropy, but a contribution from vibrational entropy would only arise if the basins sampled have a different curvature.

From the phonon entropy presented in Fig. 5.11, we can conclude that the vibrational entropy

contribution to the dynamics occurring through glass transition is negligible. Several approaches of analysis of the DOS have ensured that summation of the DOS over a range of temperatures has not precluded elucidation of small changes that may be occurring. Indeed, the close agreement of the DOS curves above and below T_g are indication alone that the vibrational entropy is virtually unchanged.

It should be noted that the present neutron scattering results are not sensitive to phonons at long wavelength, owing to the overlap of intensity from the tails of the elastic peak. Correcting for these tails may not be accurate, so we also evaluated the effect on vibrational entropy from sound velocity measurements performed previously, although not for this same chemical composition [90]. Generously assuming that 10% of the phonon DOS follows the change of sound velocity through the glass transition, we obtain an increase of vibrational entropy of approximately $0.01k_B$/atom, which is negligible.

The present results help to refine our understanding of the potential energy landscape (PEL) of the atomic configurations in a fragile glass, of which Cu-Zr is an example. For fragile glasses (in contrast to strong glasses), it is expected that when moving up the PEL with thermal energy, a large number of transition states are soon accessible to the system. The presence of a large number of barriers of similar energy implies a similarity of the PEL around the different low-lying basins in the PEL. The present results do not probe the transition states between basins. Nevertheless, the negligible change in vibrational spectra across the glass transition shows that as the glass begins to make transitions between low-lying basins in the PEL, the individual basins are not significantly different in their local potentials. These results may not apply to strong glasses such as silicates, perhaps.

A more complete picture of the entropy changes through the glass transition could be obtained from comparing the vibrational entropy results presented here to the total entropy change from the increase in heat capacity. Obtaining quality differential scanning calorimetry results to obtain accurate C_p information is an experimental challenge. There measurements are currently being performed, and are detailed in Appendix B.

5.6 Conclusion

Time-resolved vibrational spectra through the glass transition in the bulk metallic glass CuZr were acquired with inelastic neutron scattering. Vibrational density of states (DOS) in ranges as small as 4K were extracted from continuous heating through the glass transition. For each temperature interval, the vibrational entropy is calculated from the DOS. This provides a detailed characterization of how the vibrational entropy contributes to the large jump in heat capacity that characterizes the glass transition in amorphous materials. This change in heat capacity has been attributed to combinations of configurational and vibrational entropy. However, the role of vibrational entropy in this transition has never been demonstrated for all vibrational modes in an amorphous material. This work provides the first experimental measurement of the change in vibrational entropy through the glass transition. We found the unique contribution of the vibrational entropy to the excess entropy in the supercooled liquid, and found that the change in vibrational entropy through the glass transition can be bound at less than 0.01 k_B per atom. By elimination, this means that the configurational entropy is dominant, putting to rest a controversial debate over the role of entropy through the glass transition.

Part 3: Nanostructured Cathode Materials for Lithium Ion Batteries

Chapter 6

Iron Trifluoride

6.1 Introduction

The secondary lithium battery is the electrochemical energy storage technology with the highest performance today, as yet unmatched in energy density and robustness in charge-discharge cycling [94, 95]. The high energy density is directly attributable to the significant voltage difference between the electrode materials and their substantial capacity for reversible lithium storage, although the fundamental reasons for their good cycling performance is less well-understood. Metal fluorides, including FeF_3, CoF_3, NiF_2, and CuF_2, have attracted recent attention as cathode materials [96]. Iron trifluoride, FeF_3, stands out as a potential electroactive material because of its attractive cost, with relatively low molecular weight and high reduction potential (owing to the highly ionic Fe-F bond) leading to high theoretical capacity and specific energy/energy density.

Early studies on pristine FeF_3 as a cathode against lithium metal demonstrated an initial discharge capacity of 140 mAh/g that decreased to 80 mAh/g upon cycling [97]. The low electrical conductivity and resulting poor capability of FeF_3 has been improved by reducing its crystal size and preparing carbon-FeF_3 nanocomposites. Carbon coating and particle-size reduction led to reports of high capacity from 300 mAh/g to 1000 mAh/g, depending on the procedure employed [98, 99, 100, 101, 102, 103]. These increased capacities have been associated with the electrochemical formation of Fe and LiF. This reaction was investigated by solid state nuclear magnetic resonance (SS-NMR) and x-ray diffractometry (XRD)[104]. The reverse reaction to recover FeF_3 from Fe and

LiF was not observed by XRD, and many details of NMR remained ambiguous due to the large amount of Li in the electrolyte residue or SEI. On the other hand, cathode materials prepared from nanocomposites of LiF and Fe in a discharged state showed a capability of cycling up to 200 cycles [105]. The cathode in a discharged stated can be alternatively prepared by reducing FeF_3 with Li_3N [106], or with LiF to form Li_xFeF_3 [107].

Many of these studies on nanostructured materials reported impressive capacities, much higher than the commercialized cathode materials such as $LiCoO_2$, $LiMn_2O_4$, $Li[NiMnCo]O_2$, and $Li[NiCoAl]O_2$, which have a capacity ranging from 100 mAh/g to 170 mAh/g. However, the work to date indicates that the majority of the extended capacity for FeF_3 is realized at lower potentials than for oxide cathodes, requiring a lower practical cutoff voltage of 1 V, and displaying a large hysteresis of approximately 1 V between charge and discharge cycles [108, 109]. In addition, the performance of this material over a large number of cycles remains unclear.

It is generally agreed that the lithiation of FeF_3 occurs in two stages, as first proposed by Amatucci et al. [98, 99]. Stage 1 is the reduction of Fe^{3+} to Fe^{2+}, with a theoretical reduction potential of 3.44 V versus Li^+/Li, and an attractive theoretical capacity of 237 mAh/g, storing one charge per FeF_3. The cutoff voltage for Stage 1 is approximately 2 V. Stage 2 converts the stoichiometric $LiFeF_3$ into Fe and LiF, with an additional capacity of 475 mAh/g. There have been many investigations of the reaction dynamics of these two stages, but the transition between the two stages remains unclear. A computational study using density functional theory reported that the original ReO_3 structure of FeF_3 changes to Li_xFeF_3 ($0 < x < 1$) with an unstable rutile structure before further decomposing to LiF and Fe [109]. However, an XRD/Mössbauer study conducted during electrochemical cycling of chemically synthesized $LiFe_2F_6$ demonstrated both reversibility and structural stability [107, 110]. Another study proposed two-phase intercalation with lithium ions first filling the (204) plane in the rhombohedral FeF_3 framework to form $Li_{0.5}FeF_3$, followed by further lithiation to form $LiFeF_3$ [104]. Today, although a chemical reduction has been demonstrated [106, 107, 110], there is scant experimental evidence to support the electrochemical formation of a rutile structure from the rhombohedral FeF_3. It also remains unclear whether the first-stage

reduction of Fe^{3+} to Fe^{2+} occurs within a single crystal structure, or if new phases nucleate during the reaction.

These questions about the two stages of lithiation extend to questions about electrochemical performance. First, what is the effect of discharge depth on reversibility and cycle life? Second, how does FeF_3 accommodate the insertion of lithium into its crystal structure? We addressed the first question by evaluating cycle life and capacity fade for different discharge voltage cutoffs. Cycling between FeF_3 and $LiFeF_3$ (Stage 1) was compared to cycling with deep discharges to LiF and Fe (Stages 1 and 2), and we report very large and systematic changes in cycle life with changes in the cutoff voltage for discharge. To address the second question, we performed an *in situ* XRD study on the structural changes during the first discharge of nanostructured FeF_3, and we offer a simple mechanism for lithiation between the compositions FeF_3 and $LiFeF_3$.

6.2 Experimental

The active cathode material was prepared by sealing equal masses of pristine FeF_3 (Alfa Aesar, 99.9%) and super P carbon black (Timcal) in a steel vial in a high-purity argon atmosphere. Ball-milling was performed with a Fritsch Planetary Mono Mill for 36 hours at 200 rpm using a steel ball-to-powder weight ratio of 42:1. A mixture of 85 wt.% ball-milled material and 15 wt% polytetrafluoroethylene (PTFE) powder in isopropanol was rolled into a free-standing film 50 μm in thickness. After the solvent was evaporated, the film was punched into 16 mm-diameter circles with a load of 2-2.2 mg/cm^2, and sealed in 2016 coin-cell cans with lithium metal as the counter electrode and an electrolyte solution of 1 M $LiPF_6$ in 1:1 or 3:7 ethylene carbonate (EC) and dimethyl carbonate (DMC). The same anode and electrolyte solution were used for pouch cell preparation, where the cathode material was pressed onto an aluminum mesh 30 mm$\times$30 mm and 200 μm in thickness ($\sim$5.7 mg/cm^2). The mesh was sealed into a pouch with a 20 mm$\times$20 mm polyethylene window at the center of one side. Coin cells were cycled at a constant current of $\pm$142 mA/g ($\sim$C/5) using an Arbin cell cycler. The pouch cell was cycled *in situ* with a rate of 2.37 mA/g ($\sim$C/100) using a Versastat potentiostat.

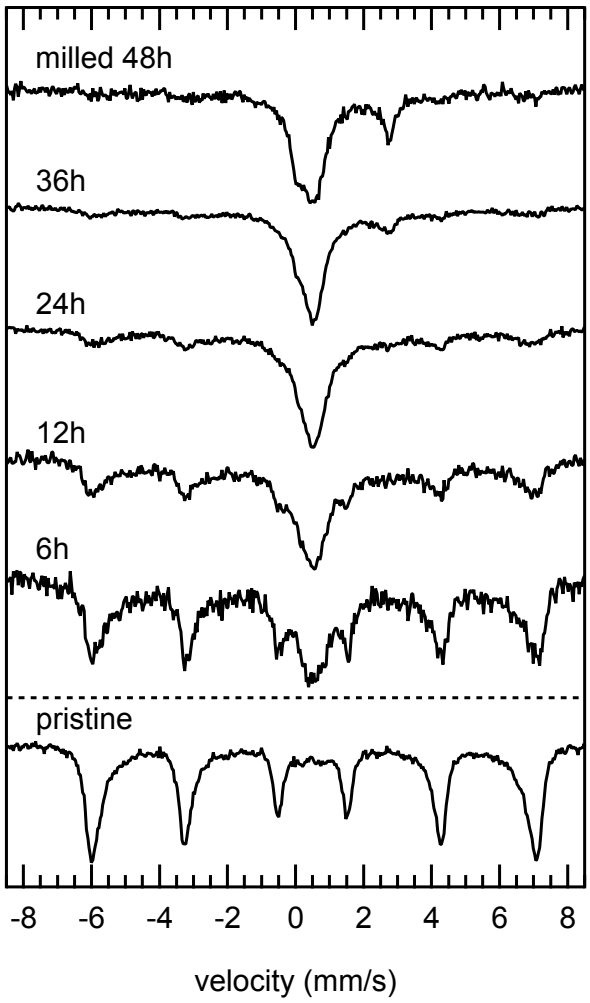

Figure 6.1: Mössbauer spectra for FeF_3 with carbon after various times of ball-milling. The pristine (as-received) material is shown at the bottom, and samples milled for increasingly longer times are shown above. All samples were sealed in an Argon atmosphere and milled at 200 rpm with a 42:1 steel ball-to-powder ratio.

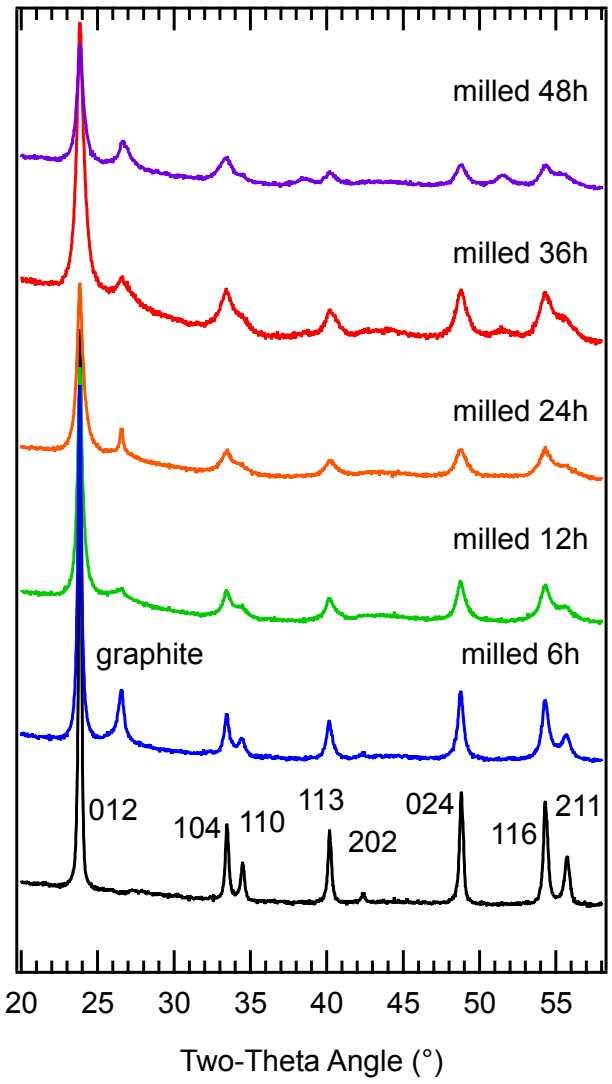

Figure 6.2: XRD patterns corresponding to the spectra shown in Fig. 6.1 for FeF_3 ball-milled with carbon for various times. Crystallite size for each spectrum obtained from Rietveld analysis is shown in Table 6.1.

Table 6.1: Particle size as a function of mill time for carbon-FeF_3 composite milled under argon at 200 RPM for the times indicated.

Mill time with carbon	crystallite size (nm)
as-received	69
6 h	41
12 h	26
24 h	21
26 h	18

X-ray diffraction (XRD) patterns were collected using Cu Kα radiation. *In situ* XRD measurements were performed with the pouch cell oriented for reflection. Rietveld analysis was used to determine lattice parameters and crystal size. CrystalMaker® and CrystalDiffract® software packages were used to design unit cells and simulate XRD patterns. A Tecnai TF30 field-emission transmission electron microscope (TEM) was used for imaging the cathode active material nanocomposite at 300 kV bias. The sample was dispersed in ethanol and prepared on a C-Flat™ holey carbon grid. Bright-field and dark-field images were acquired using a 10 μm objective aperture. The electron diffraction patterns were acquired using a 10 μm selected area diffraction (SAD) aperture.

Mössbauer spectrometry was performed with a conventional constant acceleration system with a radiation source of ^{57}Co in a Rh matrix. Velocity and isomer shift calibrations were performed with reference to a room-temperature α-Fe spectrum.

6.3 Results

6.3.1 Materials Characterization

The ^{57}Fe Mössbauer spectra of FeF_3 are shown in Fig. 6.1 for as-received material and material ball-milled with carbon for various amounts of time at 200 rpm under argon with a 42:1 steel ball-to-weight ratio. The pristine material shows a classic sextet of peaks from a large hyperfine magnetic field typical of bulk materials [111, 112]. This FeF_3 is, in fact, ferromagnetic, and powdered

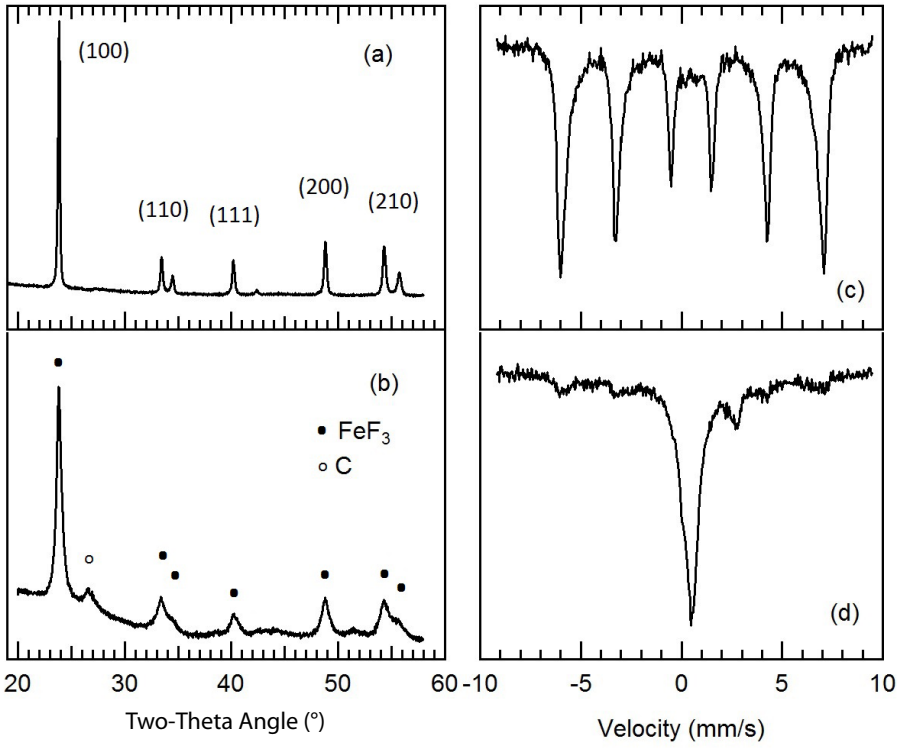

Figure 6.3: XRD patterns (a and b) and Mössbauer spectra (c and d) from FeF_3 as obtained (a and c), and the cathode material comprising carbon-FeF_3 prepared by ball-milling (b and d).

material is attracted to a permanent magnet. Ball-milling the pristine material with carbon creates a carbon-FeF_3 nanocomposite that changes the magnetic environment of the Fe atoms. As mill time is increased, the original magnetic sextet gives way to an increasing fraction of a central peak from superparamagnetic relaxation [113, 114], with an isomer shift of 0.5 mm/s (Fig. 6.1). After 36 hours of ball-milling, 75% of the 'ferromagnetic Fe' transformed to 'superparamagnetic Fe'.

After significant reduction in particle size, the majority of iron has become paramagnetic, resulting in the doublets in the center of the spectra. The transition into the paramagnetic state indicates that the iron domains in the material are below the threshold size for domain magnetism [113, 114], which is considerably reduced with particle size and carbon-coating. Continued milling for 48h causes the material to decompose from FeF_3 into rutile-structured FeF_2, evidenced by the new peak emerging in the Mössbauer spectrum around 2.5 mm/s, and confirmed with XRD.

XRD patterns of the ball-milled carbon-FeF_3 nanocomposite corresponding to the Mössbauer

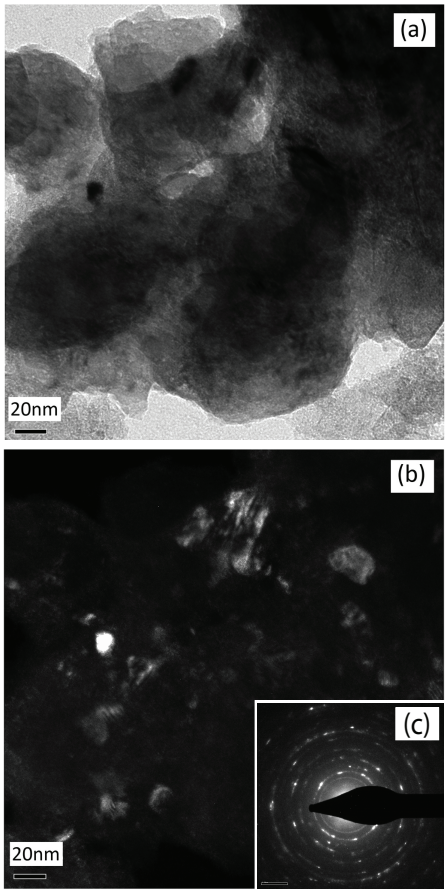

Figure 6.4: Images of the ball-milled carbon-FeF_3 composite: (a) bright-field TEM image, (b) dark-field TEM image taken from the FeF_3 (100) diffraction ring, and (c) electron diffraction pattern acquired from the same area of (a) and (b).

spectra in Fig. 6.1 are shown in Fig. 6.2. The additional peak, the (002) peak of graphite, is visible. These results are consistent with previous studies of FeF_3 with similar materials preparation[98, 99, 104]. FeF_3 is commonly indexed to a $R\bar{3}c$ rhombohedral crystal structure [98, 99, 104]. However, the unit cell is only slightly distorted from the cubic ReO_3 structure, having a decrease in α-angle from 90° to 88.23°. This shearing of the unit cell causes the diffractions at 33°, 40°, and 54° to split into two peaks. When particle sizes are small, however, there is considerable peak overlap, so for simplicity, we use the ReO_3 cubic indices to help interpret changes in the diffraction patterns with lithiation.

Increasing mill time results in continuously broader peaks. The crystallite particle size as a function of mill time is given in Table 6.1, as determined from Rietveld analysis. The reduction in

crystallite size is non-linear with mill time. The greatest reduction occurs after 6 hours of mill time, after which nominal particle size reduction occurs with each additional 6 h of mill-time. However, significant changes in the Mössbauer spectra continue to occur with increased milling, indicating that while further reduction in particle size is not occurring as rapidly, the material continues to be better mixed with the carbon matrix, which influences the environment of the Fe atoms.

The XRD patterns and Mössbauer spectra of the the ball-milled carbon-FeF_3 nanocomposite used in this study are shown in Fig. 6.3 (b) and (d) in comparison with pristine FeF_3 (a) and (c). The material milled with carbon for 36 h was selected because the fraction of superparamagnetic iron in the material is dominant over the antiferromagnetic without indication of any additional phase formation in the XRD. The average crystallite size of 18 nm is small enough to benefit from reduced particle size effects commonly observed in nanocomposite cathode materials [99, 98].

Bright-field and dark-field TEM was performed on the ball-milled carbon-FeF_3 nanocomposite. Images acquired from the same region of the sample are shown in Fig. 6.4. The bright-field image in Fig. 6.4(a) shows the aggregated FeF_3 nanoparticles surrounded by amorphous carbon. The dark-field image in Fig. 6.4(b) was taken using the FeF_3 (100) diffraction ring (d = 3.60 Å). An average particle size of 15 ± 8 nm was determined by examining several regions of the sample, which is consistent with the value of 18 nm obtained from XRD. In the electron diffraction pattern of the carbon=FeF_3 nanocomposite shown in Fig. 6.4(c), the innermost fine ring corresponds to the 10 μm SAD aperture used to obtain the diffraction pattern. The remaining diffraction rings visible in Fig. 6.4(d) match well with indexes of FeF_3 as a ReO_3 cubic structure, consistent with the XRD pattern of Fig. 6.3(b). A number of electron diffraction patterns were taken and impurities from ball-milling such as Fe or Mn metals were not found, nor were any additional elements visible by energy-dispersive X-ray spectroscopy (EDS) analysis of the milled materials.

6.3.2 Electrochemical Measurements

Electrochemical cycling tests were performed using a constant current of ±142 mA/g. This rate is equivalent to C/5 for a three-electron conversion from FeF_3 to Fe with a theoretical capacity of

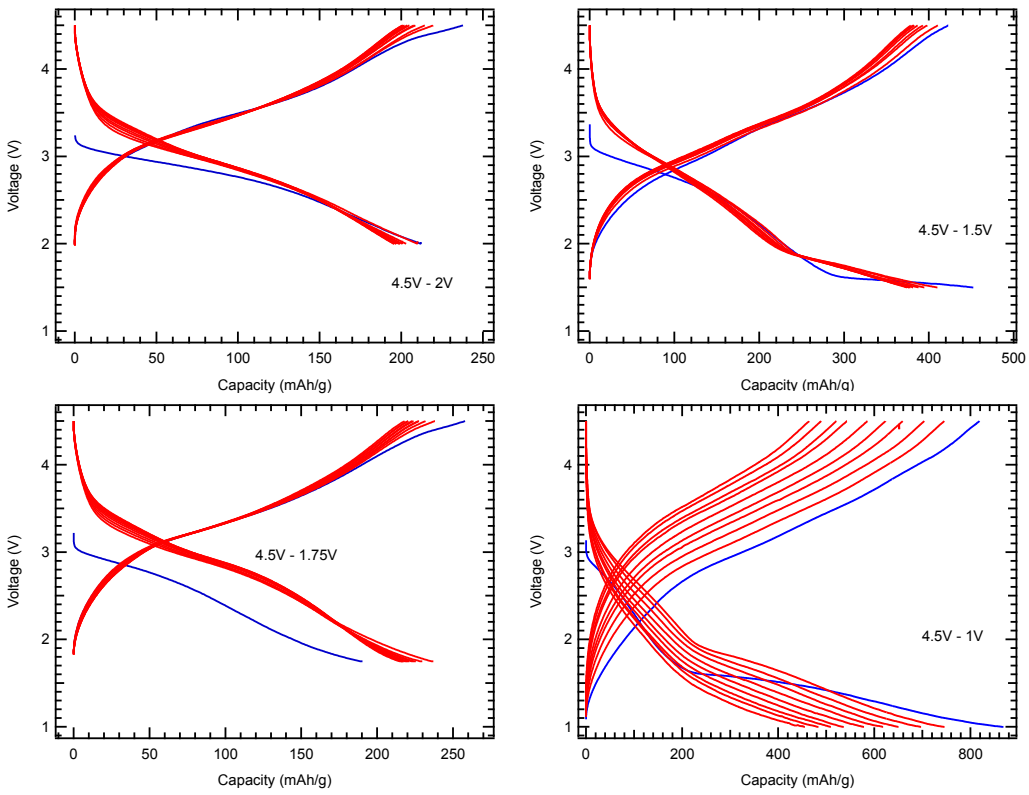

Figure 6.5: Cycling curves for coin cells cycled at $\pm 142\,\mathrm{mA/g}$ between 4.5V and 1.0V, 1.5V, and 1.75V, 2.0V. The first ten cycles are shown, with the initial cycle in blue.

710 mAh/g. One set of tests was performed over 10 cycles with a maximum voltage of 4.5 V and minimum discharge voltages of 1.0, 1.5, 1.75, and 2.0 V. Voltage versus capacity curves are shown in Fig. 6.5, with the first cycle in blue and subsequent cycles in red. In all cases, the capacity decreases with cycling. A substantial initial capacity is observed during discharge to 1.0 V, reaching over 800 mAh/g on the first cycle, compared to only 220 mAh/g on the first cycle discharged to 2.0 V.

The specific capacity and specific energy density as a function of cycle number are shown in Fig. 6.6. The largest capacity and energy density come from cycling to a lower voltage cutoff of 1.0 V, but this benefit may be offset by the significant capacity fade from over 800 mAh/g to less than 500 mAh/g after just ten cycles. In contrast, cycling to a higher voltage cutoff of 2.0 V yields a much more stable capacity and energy density over 10 cycles, although the capacity is only ∼200 mAh/g.

Thus, a second set of tests were undertaken to investigate discharge voltages of 1.0 and 2.0 V over a larger number of cycles. Figure 6.7 shows voltage versus capacity curves for selected cycles over 100-cycle tests between 1.0 to 4.5 V, and 2.0 to 4.5 V. The cells undergoing the 'deep discharge' to 1.0 V showed a large voltage hysteresis between charge and discharge, indicating very low Coulomb efficiency. Their discharge profiles had large slopes, and their discharge capacity faded quickly during cycling. The cells undergoing the 'shallow discharge' to 2.0 V showed a voltage plateau between 3.0 and 2.7 V that undergoes little change up to 20 cycles. Their capacity decreased slowly upon cycling, with the slope of the discharge curve increasing gradually. The voltage hysteresis remained around 0.7V to the 100th cycle. The voltage hysteresis during cycling with a "shallow discharge" was much smaller than for the "deep discharge", consistent with previous cyclic voltammetry results [109] which are discussed in the next section.

The performance of the cathode material may be better demonstrated by comparing the relative capacities versus cycle number for the different depths of discharge. In Fig. 6.8(a), the charge and discharge capacities relative to the charge capacity in the third cycle are plotted versus cycle number. Figure 6.8(b) shows that even over 10 cycles, there are obvious differences in the capacity fade as a function of minimum discharge voltage. When discharged to 2.0 V, the capacity loss after

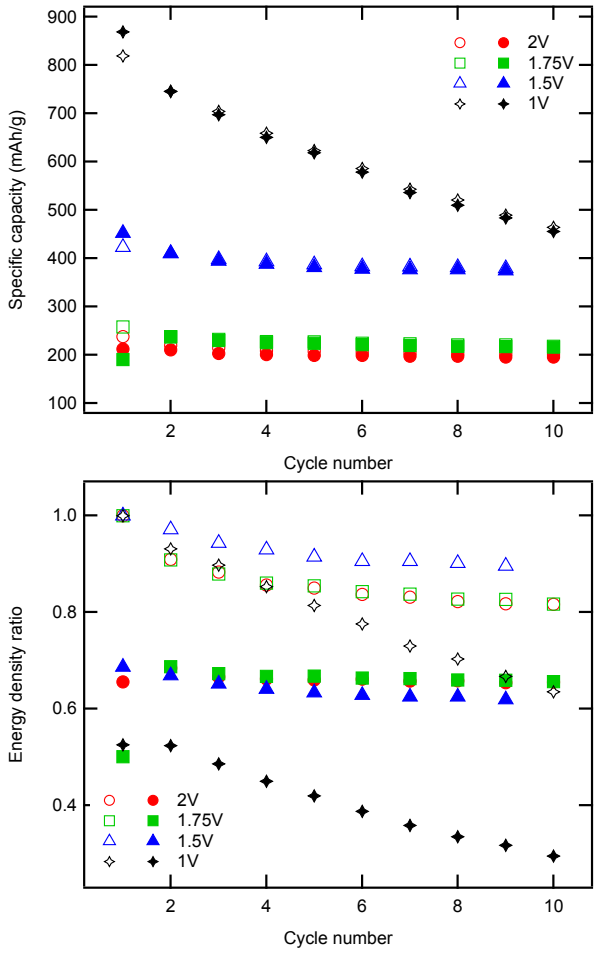

Figure 6.6: Specific capacity and energy density shown as a function of cycle number for charge (solid symbols) and discharge (empty symbols) corresponding to the voltage profiles shown in Fig. 6.5. Coin cells were cycled at $\pm 142\,\mathrm{mA/g}$ between 4.5V and 1.0V, 1.5V, and 1.75V, 2.0V.

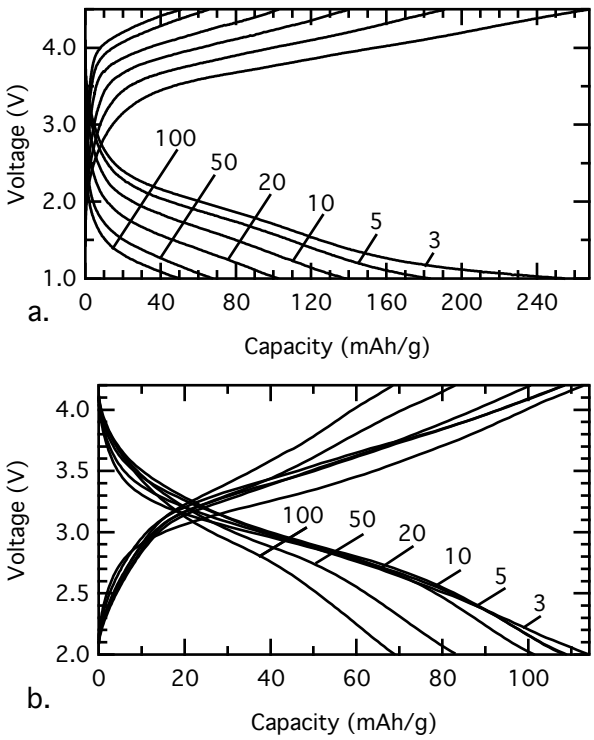

Figure 6.7: Cycling curves for coin cells cycled at $\pm 142\,\mathrm{mA/g}$ between (a) 4.5V and 1.0V and (b) 4.5V and 2.0V. Each cell underwent 100 cycles. The 3rd, 5th, 10th, 20th, 50th, and 100th cycles are shown.

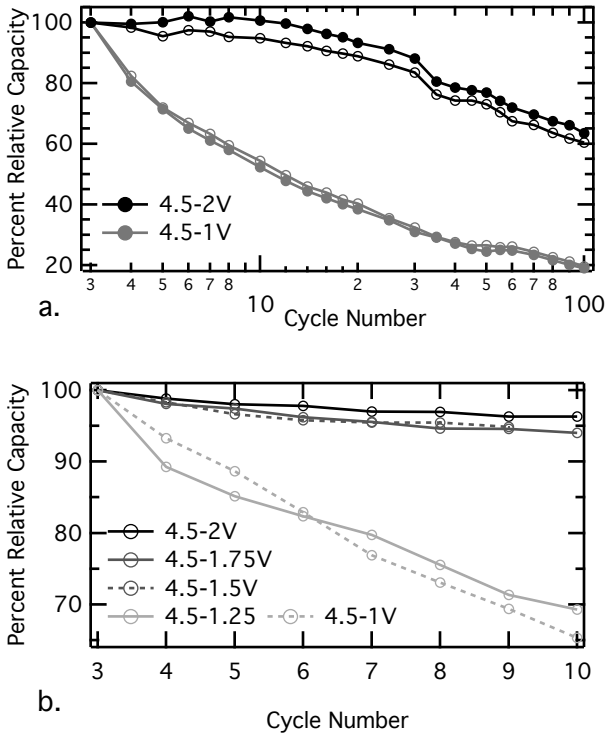

Figure 6.8: Coulombic efficiency relative to the third cycle versus cycle number for capacities during charge (solid circles) and discharge (empty circles). (a) Capacities in the extended tests shown in Fig.6.7. (b) Capacities from shorter tests.

10 cycles was 4%, whereas discharging to 1.75 V and 1.5 V caused capacity losses of 5% and 6%, respectively. For deeper discharges below 1.5 V, the capacity losses in 10 cycles jumped to greater than 30%. These differences were even more prominent after further cycles, as seen from Fig. 6.8(b). For shallow cycling between 4.5 and 2.0 V, both charge and discharge capacities were stable for the first ten cycles, decreased approximately 10% between cycles 10 and 20, and reached 100 cycles with over 60% capacity remaining. Deep cycling between 4.5 and 1.0 V gave a fade in capacity to 50% after 10 cycles, an additional fade to 40% between cycles 10 and 20, and less than 20% capacity remained after 100 cycles.

6.3.3 *In situ* XRD

A set of *in situ* XRD measurements were performed on uncycled pouch cells at a C/100 discharge rate to study the Stage 1 of lithiation. A typical voltage profile during this *in situ* measurement is

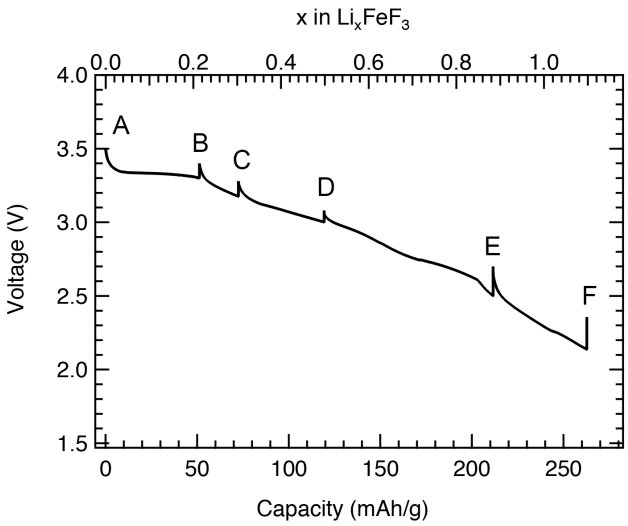

Figure 6.9: A typical galvanostatic discharge profile during the *in situ* XRD measurement, showing the points where XRD patterns were acquired A before the discharge, and at the nominal lithium concentrations, B $Li_{0.2}FeF_3$, C $Li_{0.3}FeF_3$, D $Li_{0.5}FeF_3$, E $Li_{0.85}FeF_3$, F $Li_{1.1}FeF_3$.

shown in Fig. 6.9, where XRD patterns of the cathode composite were acquired at several different steps during discharge, marked as A to F. The corresponding XRD patterns are shown in Fig. 6.10, also labeled as A to F. Indexed to the cubic ReO_3 structure, the first five peaks – (100), (110), (111), (200), (210) – are seen clearly before the discharge starts (pattern A in Fig. 6.9). As lithium ions enter the FeF_3 cell, the intensities of the (100) and (110) peaks decrease sharply, to less than 10% in step C. The (111) peak has a slight shift to higher diffraction angle from steps A to C of about 0.3° in 2θ angle, followed by a larger shift to lower diffraction angle from steps C to F of about 1°. The (210) peak has a large shift to lower diffraction angle of about 2° from steps A to F, but the position of the (200) peak remains nearly unchanged.

A unit cell of rhombohedral FeF_3 was modeled using CrystalMaker®, with the lattice parameters $a = 3.734\,\text{Å}$, and $\alpha = 88.23°$. This structure is very close to that of cubic ReO_3 shown in Fig. 6.10c with $\alpha = 90°$. The atom positions are also consistent with the alternative rhombohedral unit cell used previously ($a = 5.362\,\text{Å}$, $\alpha = 58°$) [98, 99], except for the missing (111) diffraction caused by the cancellation of Fe and F atomic form factors in a perfect cubic lattice. Different locations for lithium sites in the structure were tested, and diffraction patterns simulated. The measured

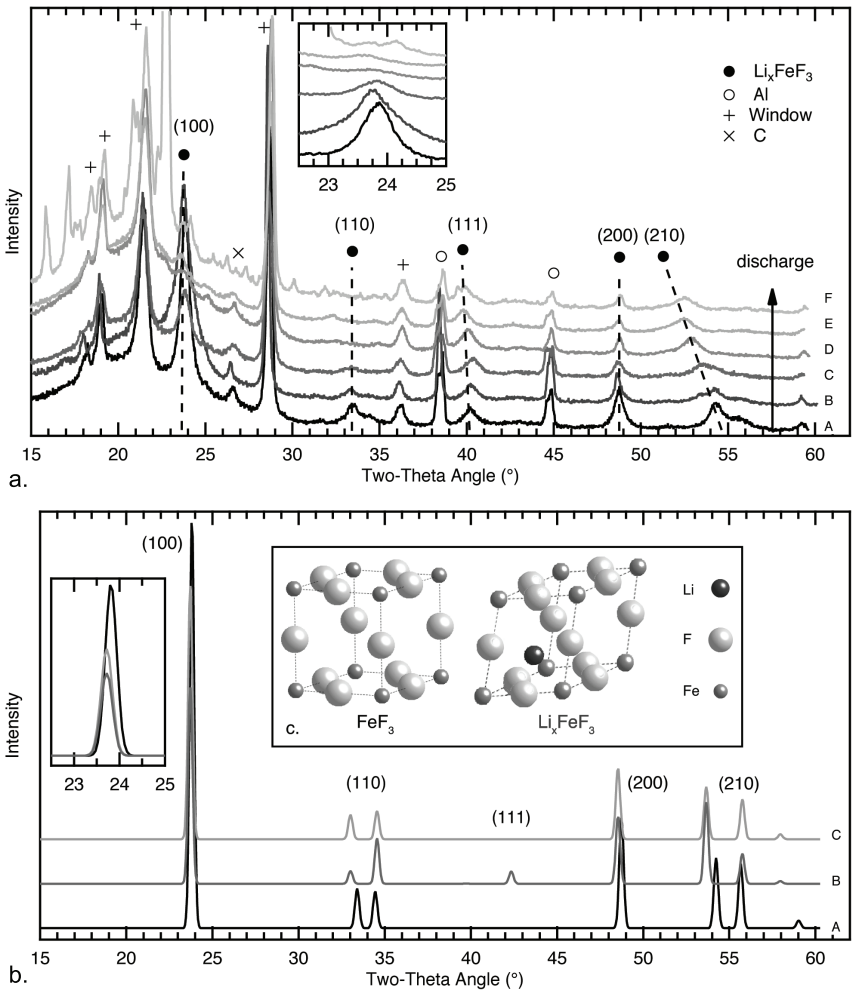

Figure 6.10: (a) XRD patterns from the *in situ* discharge measurements. Labels A-F at right correspond to the stages of lithiation indicated in Fig. 6.9, where the black curve A was obtained before discharge. (b) Simulated XRD patterns from FeF_3 (curve A, black) and Li_xFeF_3 (curve B, grey), using the unit cells depicted in the inset (c). Curve C (light grey) is simulated from the lithiated structure with rhombohedral distortion and additional 30% Li-Fe site substitution.

changes of the *in situ* diffraction patterns with lithiation, especially the reduction in intensity of the (100) diffraction and the large shift of the (210), were reproduced reasonably well when the Li^+ ion was inserted along the body diagonal of the cubic FeF_3 unit cell near three F^- ions, with the cell undergoing a small decrease of rhombohedral angle α of approximately 1°. The distortion of the unit cell with Li^+ insertion is primarily an elongation of the cubic cell along the body diagonal line in which the original (100) interplanar spacing increases by only 0.5%. The volume of the unit cell increases with the Li^+ insertion, as may be expected.

6.4 Discussion

Based on the capacity values obtained above, and consistent with the proposal of a topotactic lithiation mechanism [98], Stage 1 lithiation occurs when FeF_3/Li is discharged to approximately 2 V [99, 104, 108]:

$$FeF_3 + x\text{Li} \rightarrow \text{Li}_x\text{FeF}_3, \quad 0 < x < 1 \quad \text{(Stage 1)},$$

which we studied as 'shallow discharge'. Most previous studies on FeF_3 used 'deep discharge' that included both Stage 1 and Stage 2 when the cell voltage was reduced to 1 V versus Li. For deep discharge the overall reaction is

$$FeF_3 + 3\text{Li} \rightarrow \text{Fe} + 3\text{LiF} \quad \text{(Stage 1+2)}.$$

With deep discharge, galvanostatic cycling gives a high capacity, but shows two issues: a large voltage hysteresis, and poor cycle life. The hysteresis was systematically studied by cyclic voltammetry and galvanostatic cycling under quasi-static conditions by Liu et al. [108]. In this work, the cyclic voltammograms with a 2 V lower potential cutoff showed only about 0.25 V difference between the two redox peaks, whereas in the case of 1 V lower potential cutoff, the second redox reaction corresponding to the Stage 2 exhibits around a 1 V difference between the oxidizing and reducing peaks. Therefore, a large difference of energy efficiency is expected beween the 'shallow discharge' and 'deep discharge.' It was also reported that the large activation energy of forming Fe/LiF composite phases during discharge was the intrinsic cause of the large voltage hysteresis [108]. The capacity fade

during cycling during deep discharge is less well-understood, although prior studies have shown the formation of a number of different phases including LiF, which may be electrochemically inactive. In the course of this work, we also performed *in situ* XRD on materials subjected to deep discharges through Stage 2, but the diffraction patterns were complicated and inconsistent.

The large difference in cycle life between deep and shallow discharging shown in Fig. 6.8 suggests distinctly dissimilar lithiation mechanisms for Stages 1 and 2, and this is consistent with the evidence for topotactic insertion [98] of lithium in Stage 1, and the formation of new phases in Stage 2. Figure 6.7 and 6.8 show that the problems of capacity fade and hysteresis are greatly ameliorated when the cycling is limited to Stage 1. Although most previous studies focused on the higher capacity performance obtained with Stage 2, a better understanding of the lithiation mechanism in Stage 1 helps to explain the differences in cycle life shown in Fig. 6.8.

Stage 1 corresponds to the insertion of up to one Li^+ ion per FeF_3 unit cell. Figure 6.10c depicts a plausible configuration where the Li^+ ion is situated to allow a symmetrical rhombohedral shear, and is approximately consistent with the shifts of the measured diffraction peaks. If a Li^+ ion is inserted along the body diagonal line in the FeF_3 unit cell, it may attract three neighboring F^- ions on the edge, promoting the shear of the unit cell. There is some degree of ambiguity in this modeling, because the FeF_3 crystallites are both small and probably have some lattice strain. There is a tendency for the higher-order diffraction peaks to be broader than the lower-order ones, a characteristic of strain distribution in the material, but this is not practical to quantify with the present XRD patterns. The nanocrystals of FeF_3 are consolidated into larger particles, and another strain effect arises when individual crystals or parts of them begin to undergo rhomobohedral shears. The elastic constraint from surrounding regions does not allow the full transformation strain that occurs without constraint, for which we expect a larger change in α-angle. A distribution of α-angles may be responsible for the large broadening of the (210) diffraction peak, in particular.

A second feature of the diffraction patterns is the large decrease in intensity of the (100) diffraction peak with lithiation. This is also consistent with a previous observation by *ex situ* XRD [115]. Some such change is calculated with the Li^+ insertion and rhomobohedral shear, but the measured changes

in intensity are even larger. Such a large change can only occur if Fe atoms, which scatter x-rays strongly, occupy sites near the center of the cubic unit cell. These anti-site Fe atoms scatter X-rays out of phase to suppress the (100) diffractions. As an example with the structure of Fig. 6.10c, a 30% interchange of Li and Fe atoms accounts accurately for the intensity changes, as is seen in the the simulated pattern in Fig. 6.10b. Other point defects can explain the changes in the diffraction pattern, but some Fe disorder is required. In spite of these ambiguities, it is evident from our *in situ* measurements that lithiation involves a continuous topotactic insertion of Li through the discharge of Stage 1. In Stage 1, we did not find evidence for the formation of rutile FeF_2 or LiF [106, 104, 109], but for coin cells discharged to below 1.5 V, the diffraction peaks from LiF were prominent, along with unidentified reaction products.

We found that by limiting the discharge voltage within Stage 1, the cycle life of nanostructured FeF_3 improves dramatically. Nevertheless, there is still some loss of capacity over time. The capacity fade may be rate-dependent. During slow discharge, the voltage and capacity were much larger than shown in Fig. 6.7. Note in Fig. 6.9, for example, that the discharge capacity at 2 V was approximately 250 mAh/g, whereas it was 115 mAh/g during the faster cycling of Fig. 6.7b.

There are other challenges when using FeF_3 as a cathode. For example, the cell must be prepared with a pre-lithiated anode. Although almost all previous studies of FeF_3 used lithium metal as the anode, the dendrite issue of lithium metal likely prevents its use in practical applications. Other pre-lithiated anodes may warrant further investigation. Another approach is preparing the cathode in a lithiated form such as $LiFeF_3$ or $Li_{0.5}FeF_3$. This approach has shown promise [106, 107, 110], but more work is needed to synthesize materials with the correct stoichiometry and crystal structure.

6.5 Summary

Nanocrystalline FeF_3 was prepared and studied as a cathode material for rechargeable lithium batteries. The reduction of crystal size was characterized by XRD and Mössbauer spectrometry. For the first time, the cycle life was measured with different cutoffs for the discharge voltage. It was found that by limiting the discharge within Stage 1, i.e., storing less than one lithium per FeF_3, both the

cycle life and energy efficiency are dramatically improved compared to converting FeF_3 into Fe and LiF by deep discharge. An *in situ* XRD study of the initial discharge in Stage 1 showed a continuous change of the peak intensity and position from the original FeF_3 diffraction pattern. A lithium intercalation mechanism was proposed in which the partial Li occupancy inside the rhombohedral FeF_3 unit cell slightly distorts its lattice parameters without nucleating a new crystal structure. This mechanism is consistent with the observed highly reversible FeF_3 cathode performance.

Part 4: Conclusions and Future Directions

Chapter 7

Future Directions

The topics covered in this thesis lend themselves to extension in several directions. Possibilities for additional work are described for entropy and the glass transition and battery materials.

7.1 Entropy and Phase Transitions

The successful measurement and interpretation of the vibrational entropy through the glass transition using inelastic neutron scattering opens new possibilities for the measurement of kinetically limited processes that could not previously be studied with this technique due to instrumental limitations. An obvious next step in this work is to consider additional metallic glass compositions. Additionally, the CuZr binary structure transforms to a chemically-ordered B2 phase (CsCl structure) above 715°. Although many alloy phase diagrams have chemically-ordered crystal structures at elevated temperatures, these are usually low-symmetry phases. Our collection of INS on the metallic glass system also provided the opportunity to obtain INS spectra above this phase transformation, and analysis of these results in conjunction with heat capacity measurements can provide insight into the the role of vibrational entropy in stabilizing the B2 phase at high temperature.

7.1.1 Glass Transition

Deviation from Arrhenius-like behavior in the temperature dependence of the viscosity in glasses can be indexed by a fragility proposed by Angell [116]. Strong glasses deviate less from Arrhenius behavior and tend to be better glass formers[117], while fragile glasses have more deviation from

Arrhenius behavior. Silicate glasses are generally strong glasses, while Pt-based glasses tend to be fragile.

The CuZr metallic glass studied in Chap. 5 is a relatively fragile glass, and we concluded that there was a negligible change in vibrational spectra across the glass transition. This indicates that as the glass begins to make transitions between low-lying basins in the PEL, the individual basins are not significantly different in their local potentials. However, the number of low-lying basins in the PEL may differ for strong glasses, giving the material access to fewer transitions states as it moves up the PEL with thermal energy. Thus, an INS to measure the vibrational entropy through the glass transition in a strong glass is the next logical experiment.

7.1.2 Crystalline Phase

A peculiar crystalline phase that is found in the Cu-Zr phase diagram is the chemically-ordered B2 structure of equiatomic CuZr. This phase exists in equilibrium only at high temperatures, so it must have relatively high entropy. The B2 phase (prototype CsCl) is highly symmetrical, has little chemical disorder, and is stable only in a narrow range of composition. This B2 phase undergoes a eutectoid transformation below 715° to two other intermetallic compounds of lower symmetry. Thermodynamic assessments give it an entropy of stabilization of 0.46 k_B/atom with respect to pure Cu and Zr, which cannot be accounted for by configurational entropy [118].

There is almost certainly some stabilization of this B2 phase at high temperatures due to its vibrational entropy being greater than the $Cu_{10}Zr_7$ and $CuZr_2$ phases that form from it at temperatures below 715°. Although many alloy phase diagrams have chemically-ordered crystal structures at elevated temperatures, these are usually low-symmetry phases. The rule of thumb today is that phases of low symmetry tend to have higher vibrational entropies due to anisotropic atom vibrations. Thus, the B2 phase in Cu-Zr is a major exception to a rule for vibrational entropy stabilization in low-symmetry structures.

Combination of INS and heat capacities above the B2 phase transition in CuZr, $Cu_{10}Zr_7$, and $CuZr_2$ will allow a quantitative description of what role configurational entropy and vibrational

entropy each play in the stabilization of the highly-ordered high-temperature structure in the binary alloy. This chemical order-disorder transformation has been studied in other systems, including CuZn and FeCo. In the case of FeCo, the ordered phase was studied in a quenched sample at 300K, and showed the vibrational entropy role to be small in the B2 ordering transformation of FeCo **??**. The CuZn system was studied in the 1950s using a classical partition function for vibrations in the Einstein model to extend the early model of Bragg-Williams that explained order-disorder transformations without vibrational entropy**??**.

Thus, there are still open questions in identifying if and how vibrational entropy stabilizes the high-symmetry B2 phase at high temperature. Additional work on Cu-Zn and Fe-Co may also be warranted at high temperatures, depending on what is revealed from the CuZr work. The Fe-Co system could be of particular interest, because NRIXS could be used to extract the pDOS from the iron atoms, giving the individual contributions of Fe and Co atoms by extraction from INS of the total vibrational entropy.

7.2 Battery Materials

The development of new materials for anodes and cathodes is one of the most active areas of research and development for lithium batteries. For the most successful electrode materials, lithium atoms are inserted into a host crystal, and then removed from it as the battery is charged or discharged. The crystal undergoes distortions, sometimes considerable, when lithium is inserted or removed. These changes to the crystal lattice are often deemed responsible for deterioration such as fracture, decrepitation, and a loss of electrochemical performance that occurs over many cycles [119]. Study of the 'ageing' behavior of batteries seeks to understand the irreversible changes in the active materials of electrodes that result in decreased capacity and power capabilities over many cycles [120]. The post-mortem study of the complex changes that have occurred within the cell is well suited to experimental techniques that require disassembly of the cell for analysis. However, these studies often reveal only the formation of new phases, and fail to explain their time sequence, providing less help in finding underlying mechanisms of lithiation that would be useful in the development of new

materials.

In work presented in Chapter 6, we studied one cathode material for lithium batteries by examining its cycling performance and proposing a lithium intercalation mechanism consistent with highly reversible FeF_3 cathode performance over a limited voltage range. While structural investigations by XRD have already led to proposed reaction mechanisms for this material, many questions remain that could be further investigated to improve the performance of this material or provide insight into in the reaction mechanisms of other potential cathode materials [98, 99]. Neutron scattering presents a unique opportunity for detailed structural investigations because of its sensitivity to Li and ability to penetrate deeply into materials. Possible experiments to study FeF_3 and other cathode materials are discussed below.

The results presented in our work on the cycle life of FeF_3 and the large range of reported capacities for this material (80 $mAhg^{-1}$ to 600 $mAhg^{-1}$ for nanocomposites of carbon- FeF_3 [98, 99, 100]) also raise questions about how the preparation of the material may be affecting cycling performance. Additionally, commercialization of this material is limited because it requires a lithium anode, unless a method for prelithiation can be found that demonstrates the same electrochemical performance. These questions are also discussed below as issues for the continued development of FeF_3.

7.2.1 Continued Development of FeF_3

Reports of high capacities for carbon-FeF_3 nanocomposites have drawn attention into its development as a cathode material for lithium-ion batteries. Web of Science reports find more than 400 papers published on this material, with more than 100 papers published in 2012 and 2013.[1] Despite limitations in cycle life and reversibility detailed in Chapter 6, this material continues to attract attention because of its attractive cost, relatively low molecular weight, high reduction potential, and high theoretical capacity and specific energy/energy density.

We demonstrated the limitations of cycle life that result from cycling with different cutoffs for

[1] Search performed May 2014 using keywords 'FeF3' or 'iron fluoride' and 'battery.'

the discharge voltage, and showed the dramatic improvements in cycle life and energy efficiency that result from more shallow cycling. Our *in situ* XRD work led to a proposed lithium intercalation mechanism that is consistent with the highly reversible FeF_3 cathode performance that we demonstrated by limiting the cutoff of the discharge voltage. However, many open questions remain about the detailed structural changes that accompany the proposed two-stage process for lithiation, especially after tens of cycles may have produced irreversible domains of reaction products.

Mössbauer spectrometry was used as an effective method to characterize the carbon-nanocomposite material and optimize its preparation for use in the cycle tests. Its unique nature as a probe of the local electronic structure and dynamics in iron compounds is ideally suited to the investigation of iron-containing cathode materials. While XRD has the advantage of revealing structural changes in the cathode material as a whole during cycling, the numerous changes often render the data extremely difficult to interpret [98, 100]. Using Mössbauer spectrometry to characterize changes to the environment of iron atoms during cycling of a pouch cell battery will narrow the focus to a single critical component of the cathode material. The fraction of Fe^{3+}/Fe^{2+} ratios can be extracted at each state of charge, revealing details of the reversible and irreversible structural changes occurring during cycling. This approach was demonstrated for $LiFePO_4$, and provided results consistent with changes observed with XRD [121].

An additional challenge when using FeF_3 as a cathode is that the cell must be prepared with a pre-lithiated anode. Although almost all previous studies of FeF_3 used lithium metal as the anode, the well-documented issue of dendrite formation on lithium metal likely prevents its use in practical applications [94]. Prelithiation of the anode, such as graphite, would result in a highly reactive compound presenting stability challenges for its handling and processing. Thus, preparing the cathode in a lithiated form such as $LiFeF_3$ or $Li_{0.5}FeF_3$ warrants further investigation. Compared to the considerable work on the study of FeF_3, there is very little work done on these materials. Some work has shown promise, usually employing mechanical alloying with Li_3N acting as a reducing agent. However, the synthesis of these materials with the correct stochiometry and crystal structure has been challenging [106, 107, 110]. Additionally, the resulting nanocomposites have not demonstrated

cycling performance matching their electrochemically-formed counterparts [106].

The use of n-butyllithium as a chemical reducing agent for pre-lithiation of metal fluorides was first investigated prior to the upsurge in popularity of FeF_3 [122]. It has not generated much interest, perhaps due to the challenges of working with n-butyllithium in an electrochemical lab. Our preliminary attempts to produce $Li_{0.5}FeF_3$ have shown promising XRD and Mössbauer results that indicate that the correct crystal structure can be achieved. However, this method did not produce nanoparticles of the size typically studied (such as in Chap. 6), nor are they carbon-coated, as is typical to improve conductivity. Further development of lithiation procedures are necessary, but its performance compared with electrochemically-lithiated FeF_3 will be a critical test of whether this is a feasible replacement for FeF_3 with lithium metal anodes.

7.2.2 Directions for Neutron Scattering

In situ studies of active materials can provide a detailed understanding of the simultaneous physio-chemical and electrochemical processes during active cycling. In particular, real time measurements can provide insight into the early stages of lithium insertion and extraction that set the stage for the long-term performance of the cell. Such questions that can be addressed include how a crystal lattice rearranges after removal of lithium, whether lithium is extracted or inserted preferentially from different planes, whether delithiation causes irreversible changes to the lattice, and at what stage other atoms may leave the lattice. Understanding these processes can provide optimized parameters for cell performance, and drive the engineering of new materials.

Neutrons provide an ideal tool for the study of lithium dynamics. Previous literature has relied heavily on the use of *in situ* x-ray scattering to understand structural evolution in these materials, but is severely limited by the shallow penetration depth of x-rays and their insensitivity to lithium itself. Neutrons penetrate deeply into materials, allowing observation of both the anode and cathode simultaneously. The negative scattering length of lithium gives large contrast against its neighboring elements in the periodic table, and allows determination of its position in a crystal structure. These advantages are partially offset by strong incoherent scattering from hydrogen atoms that are usually

present in the battery electrolyte solution, and by lithium's moderate absorption cross-section. However, high neutron flux (and longer counting times), isotopic enrichment with ^{7}Li, and deuteration can offset these challenges [123].

Recent measurements on VULCAN, an engineering materials diffractometer at the Spallation Neutron Source, have demonstrated the ability to obtain information about the chemical and structural changes in a commercial pouch cell for a spatially-defined region of the cell [124, 125, 126]. Thus, there is considerable opportunity to obtain real-time information about the structural changes that occur during cycling for conditions that replicate a real system. Pair distribution function analysis is often performed for *in situ* x-ray studies of batteries, but here, the poor sensitivity of x-rays to lithium is especially problematic [127]. As the pouch cell system is further optimized for diffraction measurements, the ability to obtain PDF information will offer insight on the local structural changes that may be occurring locally in regions of the electrode material. Reflectometry measurements will present unique challenges to obtain atomically thin films with small enough surface roughness to extract meaningful depth profiles. However, more reports are emerging of successful i*in situ* measurements of Li half-cells [128], and the information that can be revealed about surface effects on the preferential extraction and insertion of lithium is uniquely accessible with this technique.

In situ neutron diffraction measurements could address questions raised from the work presented here on FeF_3 nanocomposites for lithium-ion batteries. *In situ* x-ray diffraction measurements have offered some insight into how the lattice distorts when lithium is inserted into the lattice and the potential versus lithium at which new phases form, but these studies have also prompted new questions [98]. Does first-stage reduction of Fe^{3+} to Fe^{2+} occur within one crystal structure, or do new phases nucleate during the reaction? What is the lowest voltage that can be achieved without forming irreversible reaction products? How does cycling rate affect the lithium insertion and extraction mechanism? Can reports of the formation of a rutile structure from the rhombohedral FeF_3 in chemically-lithiated materials be confirmed in the electrochemical cell [106]?

Design of the cell for these *in situ* studies will be critical to optimizing counting rates and lowering background. Large format pouch cells are preferable because they are most representative of what is

in use in applications such as electrical vehicles, and they provide sufficient loading of active materials to increase counting statistics. Modifications such as a Teflon pouch cell casing, or other polymer that does not contain hydrogen, could be considered. Assessment of sources of background from the pouch cell and a detailed process of measurement and re-design will be necessary, but a low-background cell would provide enormous improvement in the level of detail that can be achieved. Additional materials of immediate interest for similar studies include $(Li_2MnO_3)_x(LiMO_2)_{1-x}$-type layered oxides, fluorphosphates $LiFeSO_4F$ and $LiVPO_4F$, and Li_2FeSiO_4. Investigation of solid electrolyte systems, such as $Li_{10}GeP_2S_{12}$, is a considerable topic in itself, but could also be considered, as the elimination of hydrogen-containing electrolyte makes it ideal for neutron measurements.

Appendices

Appendix A

Virtual Neutron Experiments with MCViNE

A.1 Introduction

Inelastic neutron scattering data contains a complex overlap of signals that add to the measured $\mathbf{S}(\mathbf{Q}, \mathbf{E})$. Multiple scattering and multi-excitation scattering provide contributions that will vary depending on the sample (ie magnetic and lattice vibrations). Sample geometry, thickness, and temperature can vary the amounts of these contributions. Scattering from additional components in the beam such as sample containers and the sample environment is often non-trivial. In addition, scattering can occur between the sample and these components. The instrument itself has a complex resolution function. Traditional data reduction approaches assume that the resolution function can be modeled by a simple function, though in reality it is much more complex [84]. All of these components complicate the separation of the scattering process of interest from the measured signal.

The data reduction process attempts to strip the measured data of these unwanted contributions. In much of the work presented here, the single phonon density of states is extracted by removing elastic scattering, multiple scattering, and multi-phonon scattering from the measured data as described in Chapter 1, Section 1.5. Because the contributions from each scattering process are not known independently, data reduction is done with a series of approximations that are imperfect, and are not capable of capturing the complex overlap of signals.

The continued improvement of instrument design presents the opportunity to extract more de-

tailed information from experiments. This requires a fundamental understanding of the measured scattering and an accurate and reproducible approach to data reduction. The simulation of neutron experiments offers an approach to decouple aspects of the measured signal and parse the individual contributions described above.

The Monte Carlo VIrtual Neutron Experiment (MCViNE) package is a Monte Carlo neutron ray tracing package developed during the commissioning of the ARCS instrument. It is used to simulate experimental results from SNS inelastic scattering instruments [129, 3, 12]. Monte Carlo ray tracing simulations have played an important role in neutron instrument design and optimization for the last several generations of instruments. These simulations typically treat a neutron instrument as a linear chain of optical components, providing computational efficiency and simplifying the coding. MCViNE differs from previous packages in its focus on making the simulations useful for interpretation of neutron scattering spectra, and as a result several key features of its design are different. MCViNE provides easy setup for running of simulations by inexperienced users. Its construction allows for the flexible re-arrangement of components, which is important for constructing a simulation that closely mimics experiment conditions. In addition, the inherent handling of multiple scattering makes it possible to turn on and off this scattering component to see its effect on the scattering spectra.

This section describes the basic concepts of MCViNE, and compares experiments and simulations of samples typically used for instrument calibration, aluminum and vanadium. Next, a template for introducing a high-temperature furnace into the simulation is constructed and tested with empty furnace measurements. Finally, experimental data and simulations are compared for a powder sample of chromium.

A.2 Basic concepts in MCViNE

MCViNE uses the concept of a 'scatterer' to define the individual components to be scattered. The scatterer is often elemental, though it can also be a compound. For each scatterer, a shape is defined, typically a plate or rod, and dimensions inputted. There are several options for scattering

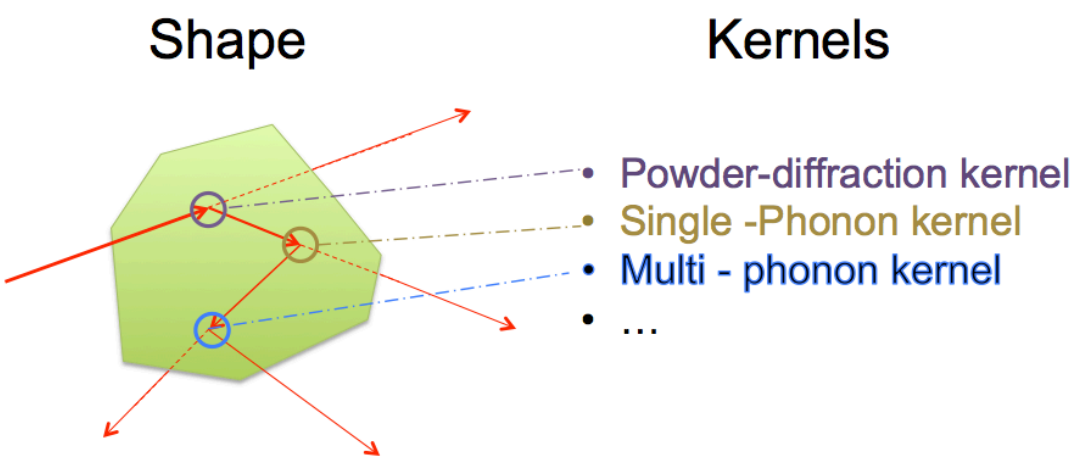

Figure A.1: A neutron incident on a scattered can be scattered multiple times. Scattering events are represented in different colors corresponding to the scattering kernel used for this event. Red arrows are paths of neutron propagation, and at each scattering event, the original neutron is also propagated out of the scatterer.

kernels for each scatterer. A powder-diffraction kernel allows coherent and incoherent elastic scattering. A single-phonon kernel allows coherent and incoherent inelastic single-phonon scattering. A multi-phonon kernel allows multi-phonon scattering using an incoherent approximation. Multiple scattering processes, allowing a single neutron to undergo more than one scattering process, can be allowed or turned off. Figure A.1 shows how a neutron incident on the scatterer, can be scattered by the various scattering kernels defined for the scatterer. The neutron follows the red path and can be scattered (i) elastically by the powder diffraction kernel, following the dashed line out of the scatterer in the same direction, (ii) inelastically by the single-phonon kernel, or (iii) in a multi-phonon process.

A 'sample assembly' is constructed from several scatterers, and arranged in a specific geometrical configuration to simulate the exact physical layout of all components in the path of the beam. For the most simple case, the sample assembly may only consist of a single scatterer in the form of a sample with a plate or rod geometry. This will be placed at the center of the sample position. A more complex sample assembly may simulate a powder sample inside of a niobium foil sachet. This sample assembly would consist of a powder sample, simulated as a plate, with a thin Nb plate on the front and back of the sample. The choice of positioning is at the discretion of the user, but is

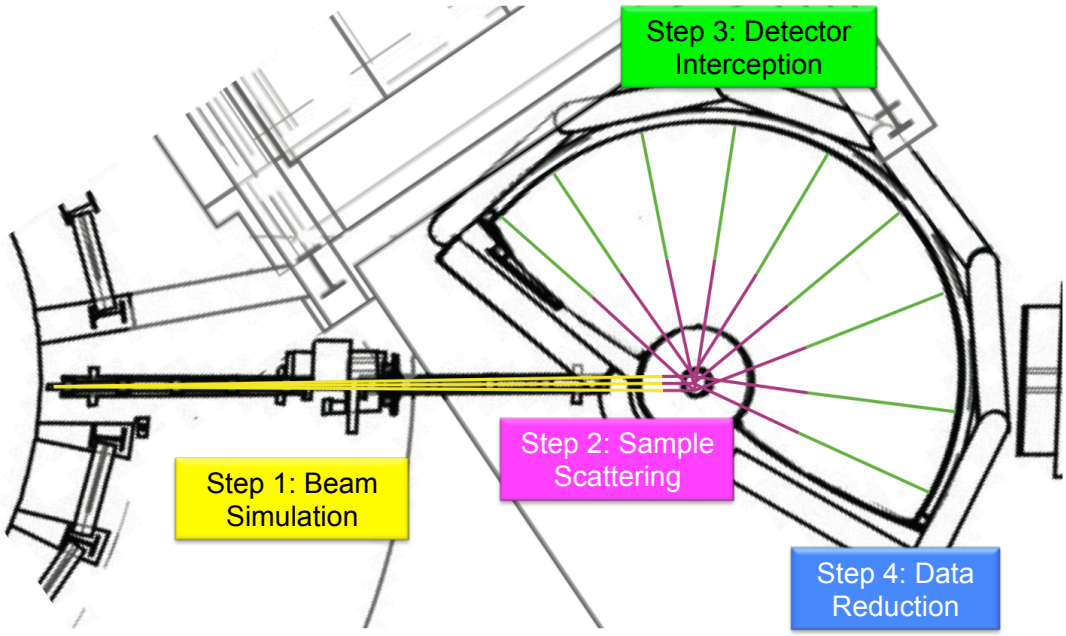

Figure A.2: The simulation proceeds in four steps, as shown for a schematic of the ARCS instrument. First, the neutrons travel from the moderator to the sample (yellow path). Second, the neutrons are incident on the sample and scatter from the sample (pink path). Third, the neutrons are intercepted by the detector array (green path). Fourth, the event-mode NeXus file is reduced using Mantid.

usually most easily defined by having the sample at the center of the beam position, and the Nb plates each offset from the beam center by one-half the thickness of the sample.

The orientation of the scatterers are individually defined in x, the direction of the incident beam, y, 90-degrees to the incident beam in the horizontal plane of the beam, and θ, the angle relative to the incident beam. The z variable defines the third axis, normal to the $x-y$ plane. The coordinate system follows the right-hand rule with positive x following the incident neutrons, positive y in the direction the finger curl, and positive z in the direction of the thumb. An example of the user-modifed input file to construct the sample assembly is given in Section A.4.

Construction of the sample assembly is the primary task of the user before beginning the simulation. The instrument configuration of the various guides and choppers down the flight path before the sample has been previously developed. The detector configuration to intercept the scattered neutron is also static and does not require user modification.

The simulation sequence follows four steps. A schematic in Fig. A.2 shows neutrons passing

through the ARCS instrument during the simulation sequence. First, the beam is simulated as the neutrons travel from the moderator to the sample. The instrument components before the sample are modeled in a linear chain, and scattering probabilities are propagated and updated by each component in the chain until the neutron reach the sample. This beam simulation is static, as long as the instrument components remain unchanged. As a result, this aspect of the simulation only needs to be run once for a given incident energy and number of neutrons.

Second, the neutron are scattered from the sample assembly. The sample assembly, as described above, is the collection of scatterers used to describe the sample and additional components including the sample container and sample environment.

Third, the scattered neutrons are intercepted by the detector array. This assigns a detector pixel ID and time-of-flight to each neutron that reaches the detector. The collected neutrons are then processed into an event-mode NeXus file. This approach to data collection is the same as is currently in use at the SNS. That is, instead of relying on histograms of detector events for finite bins of energy and time, neutrons are tagged individually.

The final step in the simulation sequence is the reduction of the NeXus file using Mantid. This reduction step uses the routines and procedures that are used for reduction of experimentally-collected data.

It is also possible to introduce a radial collimator between the second and third steps, allowing the neutrons to pass through the collimator after scattering from the sample and before entering the detectors.

A.3 Examples: Vanadium and Aluminum

In order to simulate more complex samples and sample environments, the simulations must first be validated for simple scatterers such as vanadium and aluminum. Vanadium scatters almost entirely incoherently, with a very small coherent scattering cross section. Aluminum scatters entirely coherently. The neutron scattering cross sections can be found in Table 1.1. For purposes of comparing these simple cases, thin plates were measured, mounted on the end of a stick. The

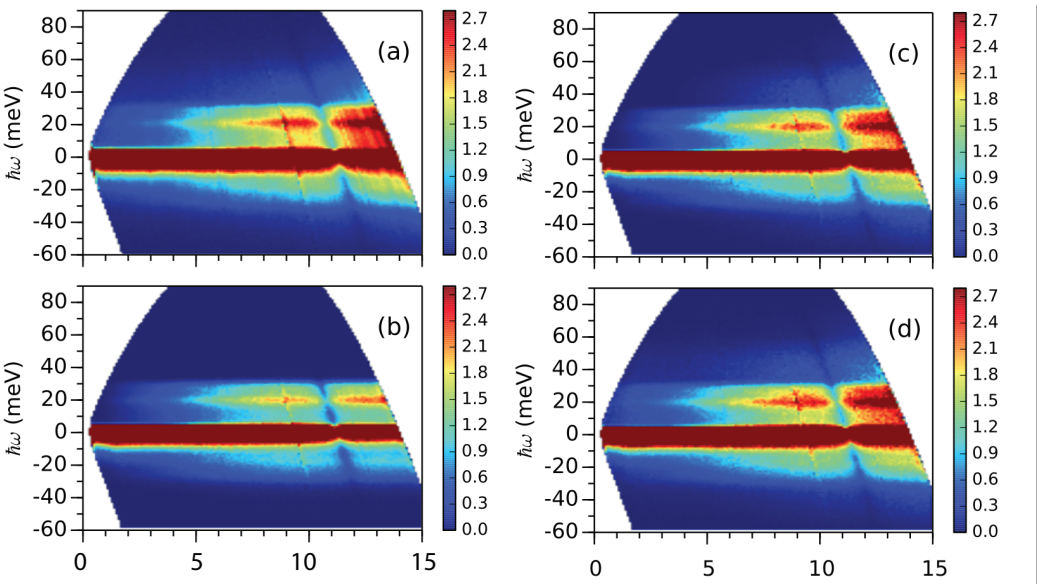

Figure A.3: Vanadium (a) Experiment, (b) simulation with no multi-phonon scattering and no multiple scattering, (c) simulation with multi-phonon scattering, no multiple scattering, and (d) simulation with multi-phonon and multiple scattering.

plates are large enough to cover the entire incident beam, and slit packages were used to mask the attachment of the sample to the stick at the top of the plate.

A.3.1 Vanadium

Vanadium is often used for calibration of instrument energy resolution. The absence of Bragg scattering peaks also makes it a typical choice for sample containment for diffraction experiments. Figure A.3 compares an experimental measurement of a thin vanadium plate (1.2 mm) in panel (a) with simulations with various scattering kernels (b-d). The most obvious features in the experimental data are the absence of defined features along the elastic line near E=0, the lack of **Q**-dependence of the intensity, and the sharp drop in intensity around **Q**=12.5 Å. The sharp intensity drop results from the 'dark angle,' a shadowing effect that occurs because of the sample's plate geometry. The sample is oriented at 90-degrees to the incident beam. Neutrons scattering from the sample in the direction of the sample plane will be less likely to reach the detector because of the considerable sample distance that must be traversed. This causes a drop in the number of neutrons received in the detectors from this scattering angle.

Figure A.3 (b-d) show simulations with various scattering kernels turned on or off. In panel (b), only an incoherent single-phonon kernel is used, and no multiple scattering is allowed. This captures reasonably well the features of the experiment in panel (a). The introduction of multi-phonon scattering in panel (c) more closely captures the higher scattering intensities at high **Q**. The comparison of the simulation in (b) and (c) demonstrate that this feature is contributed primarily by multi-phonon scattering. The addition of multiple scattering in (d) is not significantly different from (c), which contains all of the same scattering kernels but does not allow multiple scattering. It is not surprising that the effects of multiple scattering are small here, as the sample is very thin.

A.3.2 Aluminum

Aluminum is a common choice for windows and sample environment components at low temperatures because it does not scatter incoherently, and has a relatively small coherent scattering cross section. Figure A.4 compares an experimental measurement of an aluminum plate in panel (a) with simulations with various scattering kernels (b-e). The experimental data in panel (a) shows detailed features along the elastic line, as well as **Q**-dependent features as a function of **E**. The sample in this case also has a plate geometry, but the plate was oriented at 45-degrees to the incident beam. This shifts the dark angle to a position where there is no detector coverage, hence the absence of a visible dark angle as in the case of vanadium.

Figure A.4 (b-e) show simulations of aluminumwith various scattering kernels. A simulation of only incoherent elastic and incoherent single-phonon scattering in panel (b) shows the predictable lack of **Q**-dependent features and no agreement with this coherent-scatterer. A simulation of only coherent elastic (powder diffraction) and coherent single-phonon scattering in panel (c) shows reasonable agreement with the experimental data, but broad background along the elastic line is notably absent, as well as some intensity at high-**Q**. Panel (d) uses both inelastic and elastic scattering kernels depicted in (b) and (c), and also introduces multiphonon scattering. This more accurately reproduces the features lacking in (c), capturing the scattering at high-**Q**. In this case, the introduction of multiple scattering in (e) plays some role in filling in diffuse scattering, most notably along

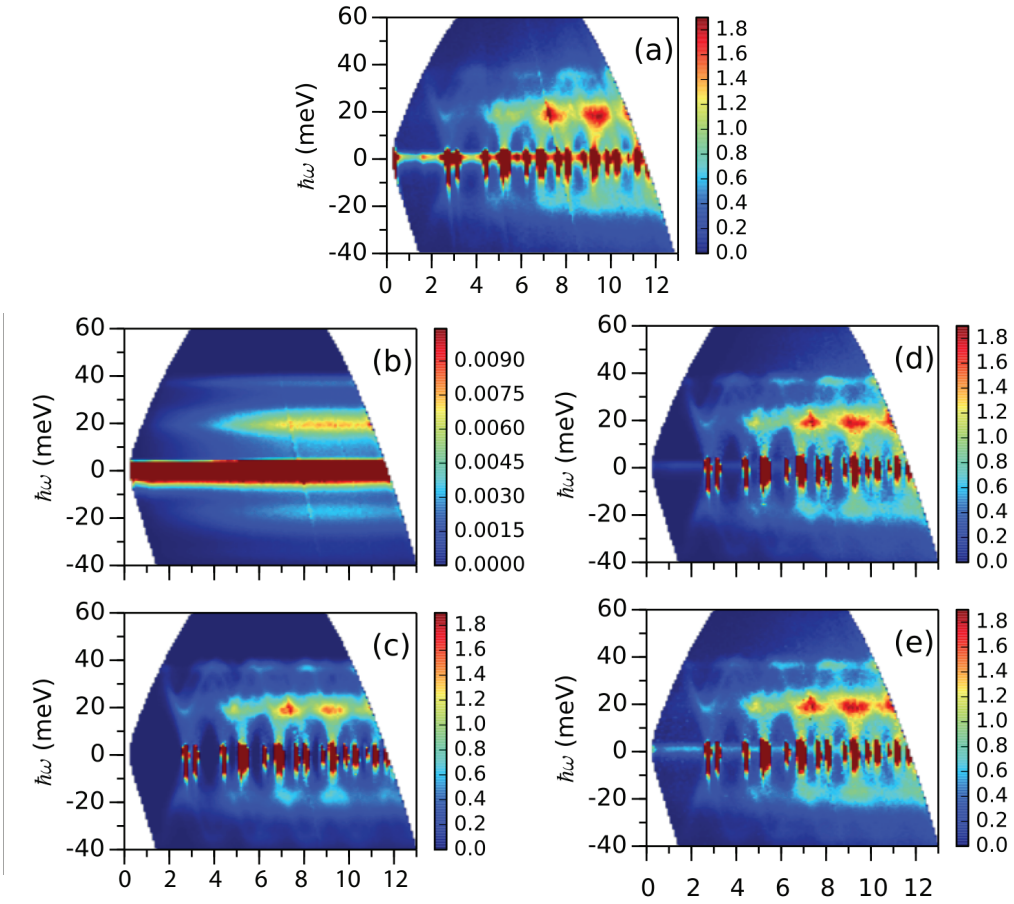

Figure A.4: Aluminum (a) Experiment, (b) simulation with incoherent elastic and incoherent single-phonon scattering, (c) simulation with coherent elastic (powder diffraction) and coherent single-phonon scattering, (d) simulation including all kernels in (b) and (c), as well as multi-phonon scattering, (e) simulation including all kernels in (d) and multiple scattering.

the elastic line.

These two case studies demonstrate the ability of the simulations to reproduce experimental data for these simple samples measured on the ARCS instrument. The power of the simulations in providing details about the origins of scattering, such as multi-phonon scattering at high-**Q** and the contribution, or lack of contribution, of multiple scattering is immediately apparent.

A.3.3 Radial Collimator

The introduction of the radial collimator to the ARCS instrument marked a considerable reduction in 'background' contributions that were difficult to characterize and often difficult to remove from measured data, as discussed in Section 1.4. Figure 1.5 shows the actual radial collimator in position around the sample space in ARCS. For the purpose of the MCViNE simulations, this component is introduced between the second and third steps of the simulation, after neutrons have scattered from the sample, but before interception by the detector. For the simulation, the radial septa are configured with the same geometrical positioning and spacing, but are modeled as 'ideal' septa that are infinitely thin and give 100% absorption.

Figure A.5 compares (a) an experimental measurement of a vanadium plate with the collimator in place with simulation (b) without the collimator and (c) with the collimator. In the experiment, the vanadium plate is positioned 45-degrees to the incident beam, while the simulation exhibits a dark angle because the plate is positioned normal to the beam. Comparison of the simulation with and without the collimator, both plotted on the same intensity scale, is informative. The collimator provides a clear reduction in scattered intensity, with a notable modulation in intensity along **Q** that likely results from visibility variation.

Figure A.6 compares experiment (a) and simulation (b) without the collimator to experiment (c) and simulation (d) with the collimator. This example also makes clear the intensity modulation that results from the introduction of the collimator. The simulation with all scattering kernels, multiple scattering, and the radial collimator in (d) does a reasonable job of reproducing the experiment result in (c), though there is an extra source of elastic diffraction in the experiment that is not

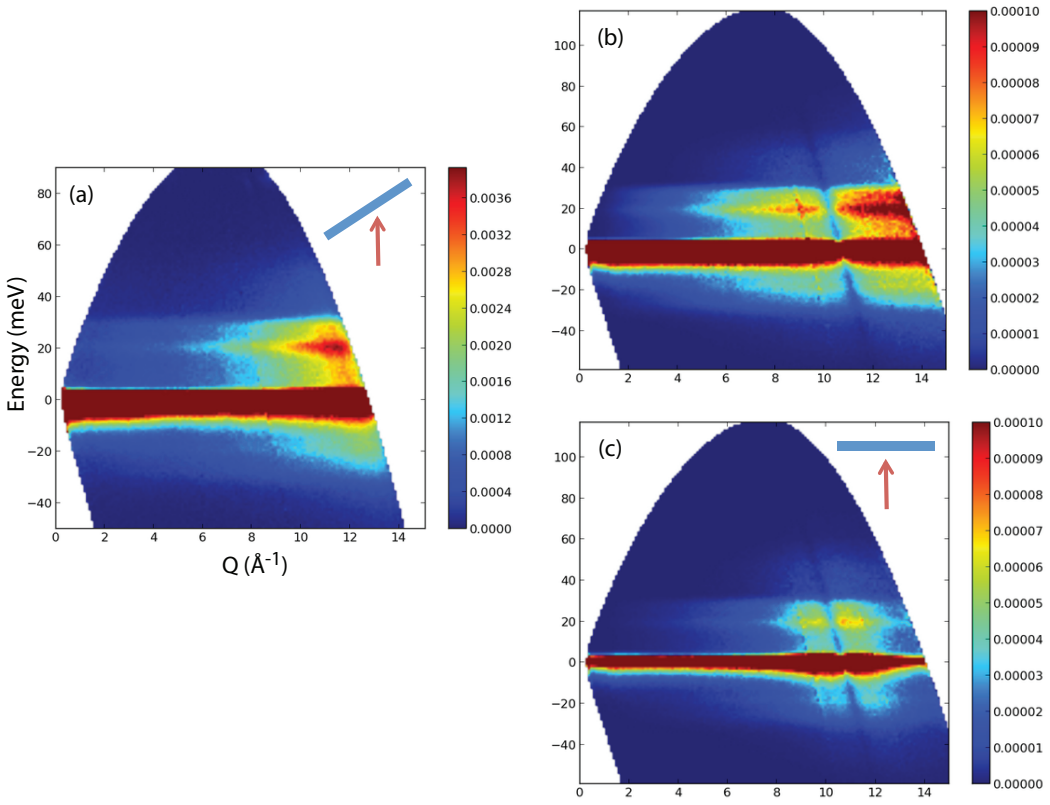

Figure A.5: Vanadium (a) Experiment with the collimator, and the vanadium plate at 45 degrees to the incident beam. (b) Simulation without the collimator. (c) Simulation with the collimator and the vanadium plate normal to the incident beam.

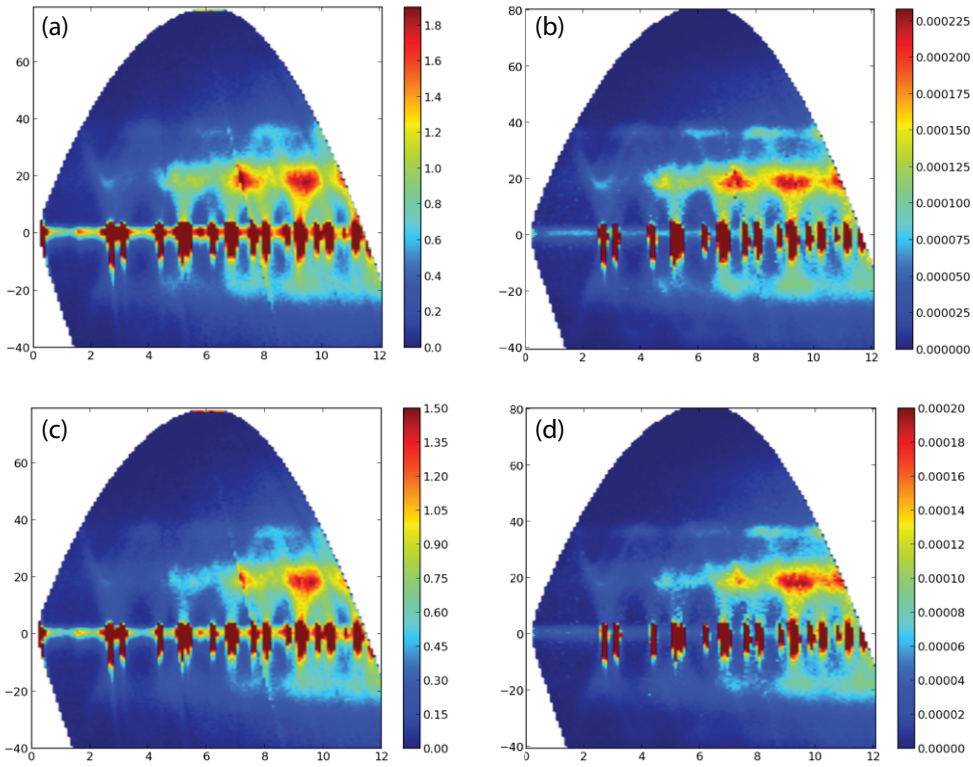

Figure A.6: Comparison of an aluminum plate without the collimator for the experiment (a) and simulation (b), and with the collimator for the experiment (c) and simulation (d).

captured in the simulation.

These examples demonstrate the successful introduction of a radial collimator component into the simulation. The radial collimator is likely to be used in routine operation of ARCS, and may be introduced in other SNS chopper spectrometers as well. For this reason, it is important to that this component to the simulation gives close agreement with experimental results.

A.4 Furnace Simulation Template

Few inelastic scattering measurements are performed only at ambient pressure and temperature, so an accurate sample environment template for MCViNE is important to providing useful simulations for comparison with experiment. Sample environments, and particularly furnaces which have many layers of heat shielding, provide a considerable background contribution to the scattering. This is visible in Fig. A.10 in which the scattering is shown from an empty furnace.

In a typical inelastic experiment, the empty furnace is measured under experimental conditions identical to those used for the sample measurement. During the data reduction process, 90% of the normalized intensity from this empty measurement is removed from the sample measurement. This approach is imperfect for a number of reasons, but notably because scattering between the sample and furnace components are not represented. This presents an opportunity for these simulations to play an important role. Accurate simulations of the empty furnace, the furnace containing the sample, and the sample by itself, could elucidate the contributions of background scattering from the furnace, and between the furnace and sample. This result could then be used to inform the fraction of 'empty' furnace measurement to be removed from the sample, or serve itself as an empty signal to be removed from the sample.

The MICAS furnace is currently the highest temperature furnace in use on ARCS, and is capable of measurements up to 1900 K (or more practically, 1500 K). The furnace is briefly described in Section 1.4. Figure A.7 shows an engineering drawing of a version of the MICAS furnace (left) and the furnace itself in storage on a cart (right). For measurement, the entire furnace is lowered with a crane into the instrument sample area. The bottom-most portion of the furnace, the many-layered

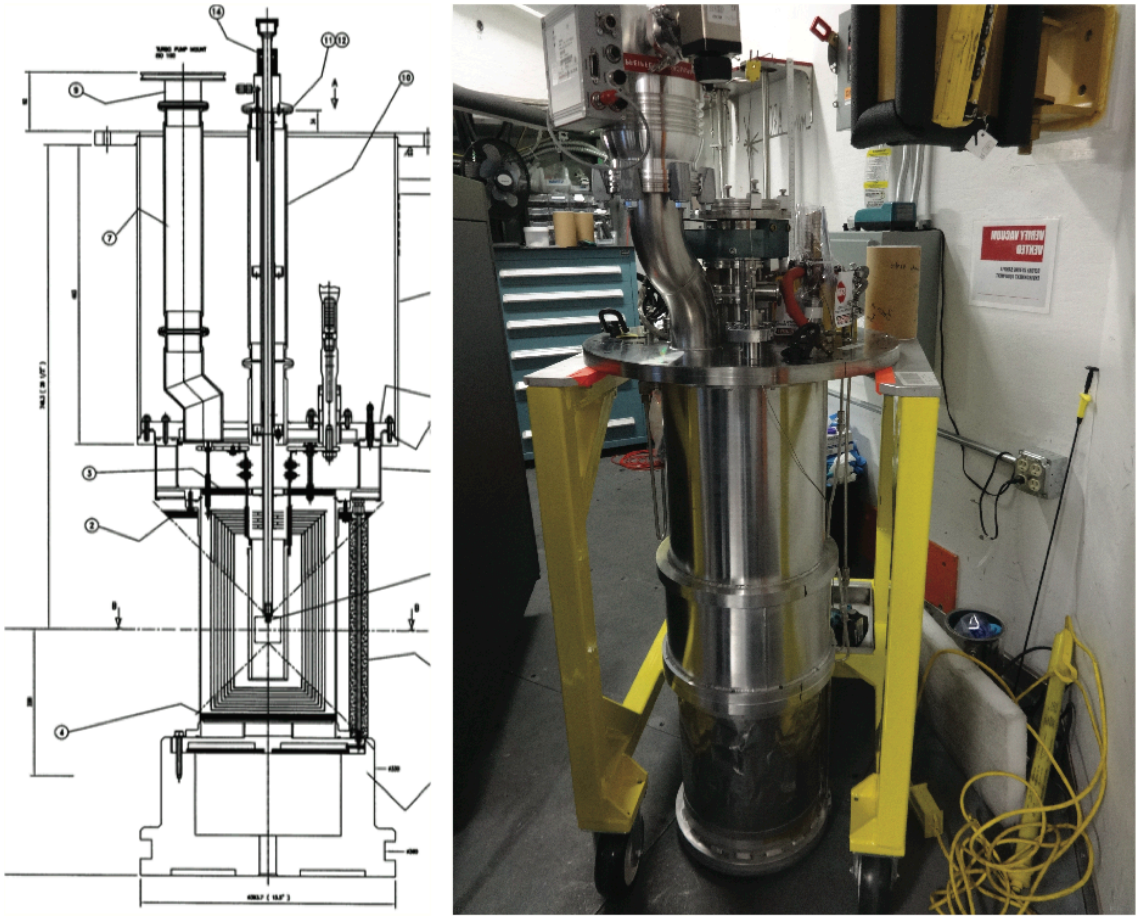

Figure A.7: Schematic of the MICAS furnace (left) and the furnace itself, in storage on a yellow cart.

region in the schematic and the crinkled-foil region in the photo, is the region of the furnace that is in the path of the beam. For introduction of this furnace into the MCViNE simulation, it is this region that must be accurately described.

The region of the furnace in the beam contains the sample at the center, which is attached to the bottom of a stick and inserted into the furnace. Concentric cylinders surround the sample providing heating and shielding, the dimensions of which are given in Table A.1. Figure A.8 shows these concentric cylinders schematically. The two inner-most cylinders serve as the heating element. This is surrounded by between 1 and 8 layers of shielding, in place to dissipate the heat radiating into the sample space. For operation at the highest temperatures, all eight shields must be in place. Dissipation of heat from the heating element into the instrument tank is an issue that must be

Table A.1: Outer diameters of the concentric cylinders of heating elements, shielding, and the outer vacuum tank containment for the MICAS furnace. All of these components are made from high-purity Nb foil with a thickness of 0.002 in.

inner heating element	3.13 in.
outer heating element	3.65 in.
heat shield 1	5.10 in.
heat shield 2	5.52 in.
heat shield 3	5.93 in.
heat shield 4	6.35 in.
heat shield 5	6.77 in.
heat shield 6	7.18 in.
heat shield 7	7.60 in.
heat shield 8	8.01 in.
outer tank	11.54 in.

observed closely, ideally by monitoring the temperature on the outer tank layer. As this outer tank layer reaches elevated temperatures, it compromises the vacuum inside the instrument tank, which presents a dangerous operating condition for the detectors. In recent modifications of the MICAS furnace design, this issue is somewhat mitigated by the addition of water cooling lines running above and below the sample region of the furnace (and not in the path of the beam).

The MCViNE furnace template is comprised of a collection of additional scatterers that can be added to the sample assembly. The optimal design of the furnace template went through several iterations. It was discovered early in the design process that the precise diameters of these layers is crucial in accurately reproducing their scattering. The values given in Table A.1 were obtained from an actual measurement of the heating element and heat shields with a micrometer when the furnace was deconstructed and not in use [1]. Initially, all of the concentric layers were simulated as individual scatterers. This proved to be cumbersome and unnecessary.

The present template consists of two scatterers: (1) the outer vacuum container, and (2) the two heating elements and eight heat shields. The outer vacuum container is described by a hollow cylinder with radius 5.77 in., thickness 0.1 mm, and height 15 in. As is obvious from the photo in Fig. A.7, this outer layer does not form a perfectly smooth cylinder because this layer is exposed during transport of the furnace. It also serves as the outer vacuum containment for the furnace, so

[1] When not in use, these layers of shielding are stored in a dry box purged with helium gas.

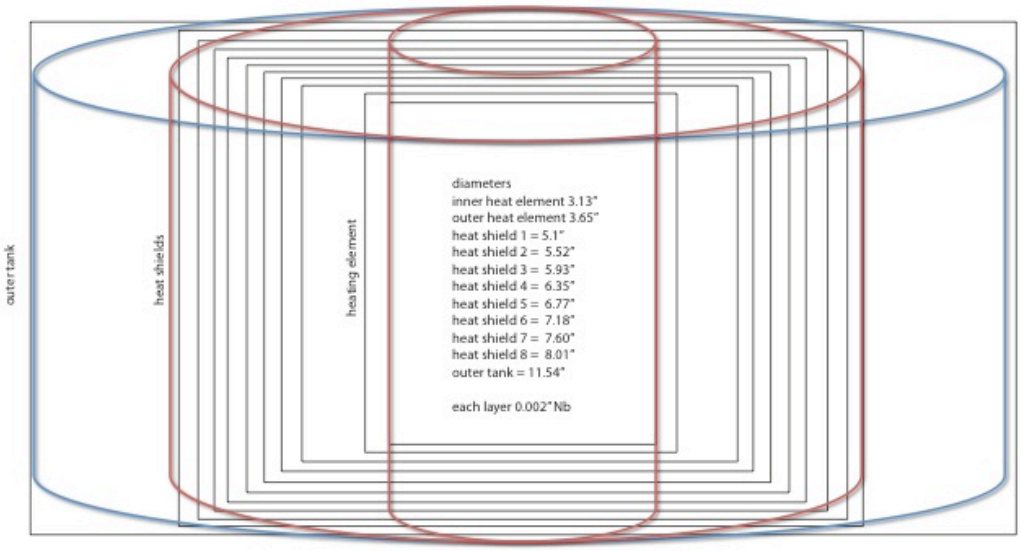

Figure A.8: Drawing (not to scale) of the heating element and heat shield region of the MICAS furnace. The inner and outer heating elements and the outer tank are fixed. Heat shields can be removed, beginning with the outermost, depending on the maximum temperature of the experiment.

any pressure imbalance that is created during pump down and venting of the furnace and sample area can cause this thin layer to crinkle. Thus, instead of modeling this region as a perfectly dense cylinder of thickness 0.002 in. (0.05 mm), it is modeled with twice this thickness, and a reduced 'packing factor' of 0.5. In Fig. A.8, this is depicted as the blue cylinder.

The scatterer describing the remaining components also has a hollow cylinder shape with inner radius 1.56 in., outer radius 4 in., and height 15 in. This hollow cylinder has a reduced packing factor of 0.008 to capture the considerable amount of 'empty space' present in this cylinder. In Fig. A.8, this is depicted by the volume encompassed by the two red cylinders.

Together, these two scatterers constitute the 'furnace template' that can be added to the sample assembly to simulate samples measured in the MICAS furnace. An example of the furnace template in the sample assembly file is shown in Fig. A.9. The sample assembly is an xml file modified by the user to add or remove components of the sample to the simulation. In this example file, the furnace template is in use as indicated by the blue labels for the two furnace scatterers, the 'outer most and 'Nb heating elements etc. 2+8. The shape, composition, and geometric conditions described for

```
<?xml version="1.0"?>

<!DOCTYPE SampleAssembly>

<SampleAssembly
   name="withfurnace"
   max_multiplescattering_loops_among_scatterers="5"
   max_multiplescattering_loops_interactM_path1="1"
   >

<!-- sample -->
  <PowderSample name="sample" type="sample">
    <Shape>
      <block width="6*cm" height="10*cm" thickness="0.2*mm" />
    </Shape>
    <Phase type="crystal">
      <ChemicalFormula>Nb</ChemicalFormula>
      <xyzfile>Nb.xyz</xyzfile>
    </Phase>
  </PowderSample>

<!-- outer most -->
  <PowderSample name="can" type="sample">
    <Shape>
      <hollowCylinder in_radius="5.77*inch" out_radius="5.77*inch+0.1*mm" height="15*inch"/>
    </Shape>
    <Phase type="crystal">
      <ChemicalFormula>Nb</ChemicalFormula>
      <xyzfile>Nb.xyz</xyzfile>
    </Phase>
  </PowderSample>

<!-- Nb heating elements etc. 2+8 -->
  <PowderSample name="heater-shield" type="sample">
    <Shape>
      <hollowCylinder in_radius="1.56*inch" out_radius="4*inch" height="15*inch"/>
    </Shape>
    <Phase type="crystal">
      <ChemicalFormula>Nb</ChemicalFormula>
      <xyzfile>Nb.xyz</xyzfile>
    </Phase>
  </PowderSample>
```

Figure A.9: The furnace template is comprised of two components added to the sample assembly file. The blue labels indicate which component is being described. The ‘outer most and ‘Nb heating elements etc. 2+8 make up the furnace.

these components are inputted as variables. A separate 'scatterer' file for each of the components provides details including the packing factor, scattering kernels, and scattering probabilities.

The furnace template was characterized at room temperature for an 'empty' furnace both with and without the radial collimator. Figure A.10 compares experimental results (a, b) with simulations (c-f). For these test cases, the empty furnace is not truly empty. The experiment contains an empty Nb sample sachet fixed in a BN absorbing frame at 45 degrees to the incident beam. The simulation is more simple than this, it contains two pieces of Nb foil at the sample position, also 45 degrees to the incident beam.

The experimental data in (a) and (b) are plotted on the same intensity scale, demonstrating the dramatic effect of the radial collimator in reducing unwanted scatter from the sample environment. Prior to the introduction of the radial collimator, the result in (a) represented the considerable background scattering that needed to be removed from the experimental data. Most notably is the high intensity scattering along the elastic line, including a peculiar split in the elastic intensity, especially towards higher **Q**. Inelastic scattering intensity is also visible, and it is even possible to make out some Nb dispersions at low **Q**. The split in intensity of the elastic scattering likely results from two distinct regions of scatterers in the furnace. There is a high concentration of Nb near the sample position, including the Nb foil at the sample position and 10 concentric layers of Nb foil within 4 in. of the beam center. This produces a set of elastic scattering peaks with an intensity somewhat broadened along **E**. The second set of elastic scattering peaks results from the outermost Nb foil layer, which is at a considerable distance of nearly 6 in. from the beam center. A gap of nearly 2 in. exists between the sample and shielding, and this outer cylinder. This produces its own set of diffraction peaks from scattering at this distinct position. In the experimental measurement with the collimator introduced (b), this effect is entirely eliminated. This is as expected because the radial geometry of the collimator is highly effective in removing scattering that occurs at angles not radiating directly from the sample position. Also noticeable in the experimental result is an intensity variation with **Q** along the elastic line. This results because the collimator is less effective at low **Q**.

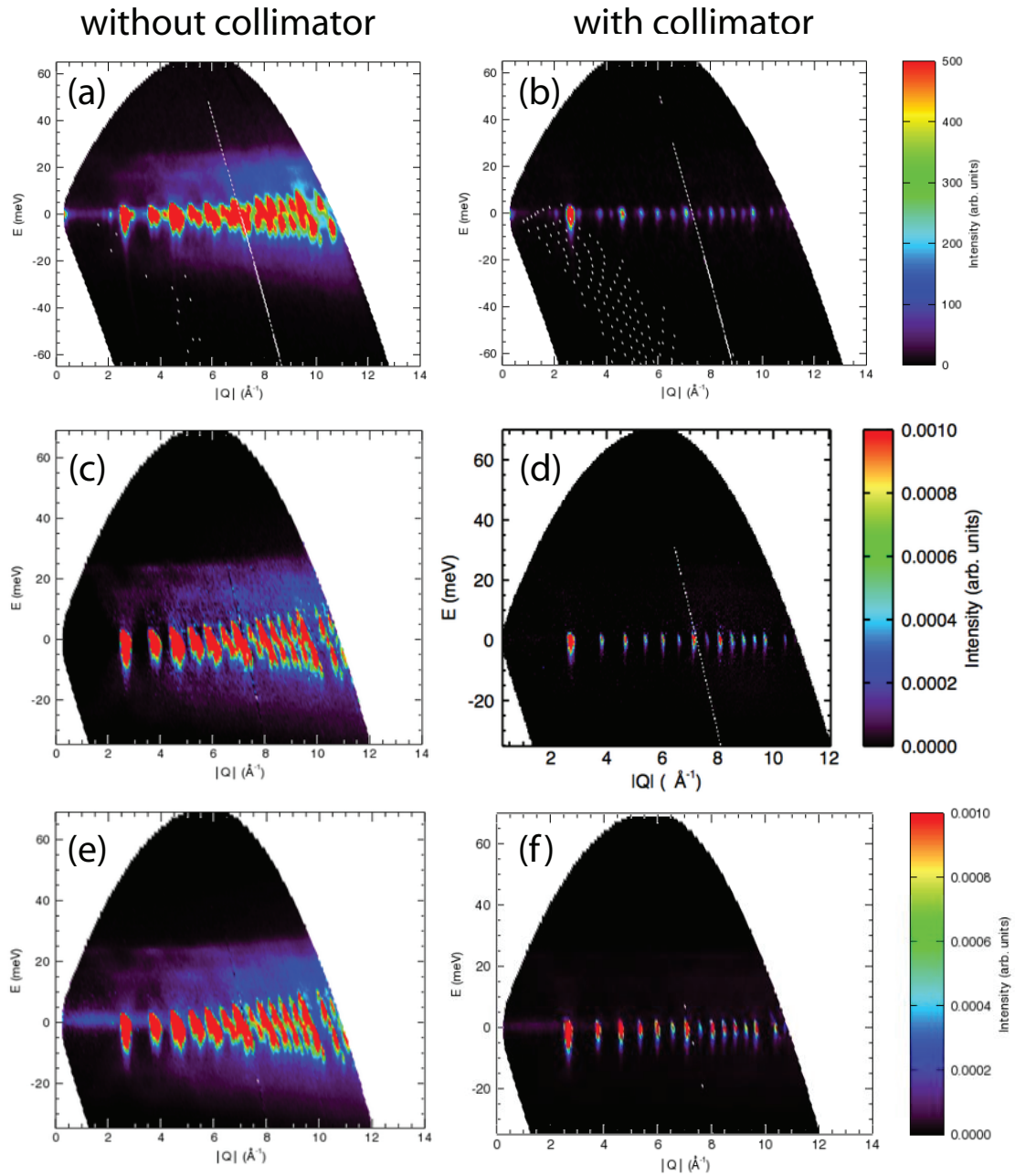

Figure A.10: The empty furnace provides significant background, as is visible from the experiment without the collimator (a), but the background is considerably reduced with the collimator (b). The simulation without the collimator is shown without multiple scattering (c) and with multiple scattering (e). The simulation with the collimator is also shown without multiple scattering (d) and with multiple scattering (f).

The simulations in Fig. A.10 show the furnace without the collimator (c, e) and with the collimator (d, f), and provide a comparison with (e, f) and without (c, d) multiple scattering. The intensity scales are matched in all of the simulated results to demonstrate the high efficiency of the collimator in reducing this unwanted background scattering. Thus, it is easier to analyze the results for the simulation without the collimator, when the features are more intense. Panel (c) shows the empty furnace with all scattering kernels in use, but no multiple scattering permitted. This reproduces the experiment data in (a) reasonably well, although intensity along the elastic line, especially at low **Q**, is noticeably absent. This is also evident in comparison of (b) and (d), the experiment with the collimator in place and simulation without multiple scattering. In (e), multiple scattering is introduced, which provides the missing intensity near **E**=0 and also smears out the scattering along **Q**. This appears to also be the case in (f), though it is less obvious.

These empty furnace measurements demonstrate the viability of the furnace template in reproducing the experimental result. The ability to model the furnace background is useful itself as a tool for characterizing unwanted scattering contributions. It also serves to validate the design of the template, which can now be tested with samples present.

A.5 Example: Chromium

In selecting a sample to use for calibration of the furnace simulation template, chromium presented a strong case. This sample is an elemental scatterer with both a coherent and incoherent scattering cross section (1.66 and 1.83 barns, respectively). This sample is also expected to be highly anharmonic [25], and it is possible to measure this sample to a reasonably high fraction of its melting temperature. Chromium melts at 2180 K, and measurements were performed in MICAS furnace to 0.7 T/T_m, or 1500 K.

Figure A.11(a) shows the $\mathbf{S}(\mathbf{Q}, \mathbf{E})$ of chromium measured in the MICAS furnace at 60°C with the radial collimator in place. Measurements were performed for a powder sample, which is two pressed plates (one large, one small) with an overall thickness of 2.2 mm. The two pieces were secured inside a Nb foil sachet, giving overall dimensions of 4.1 cm in height and 2.9 cm in width. The plates were

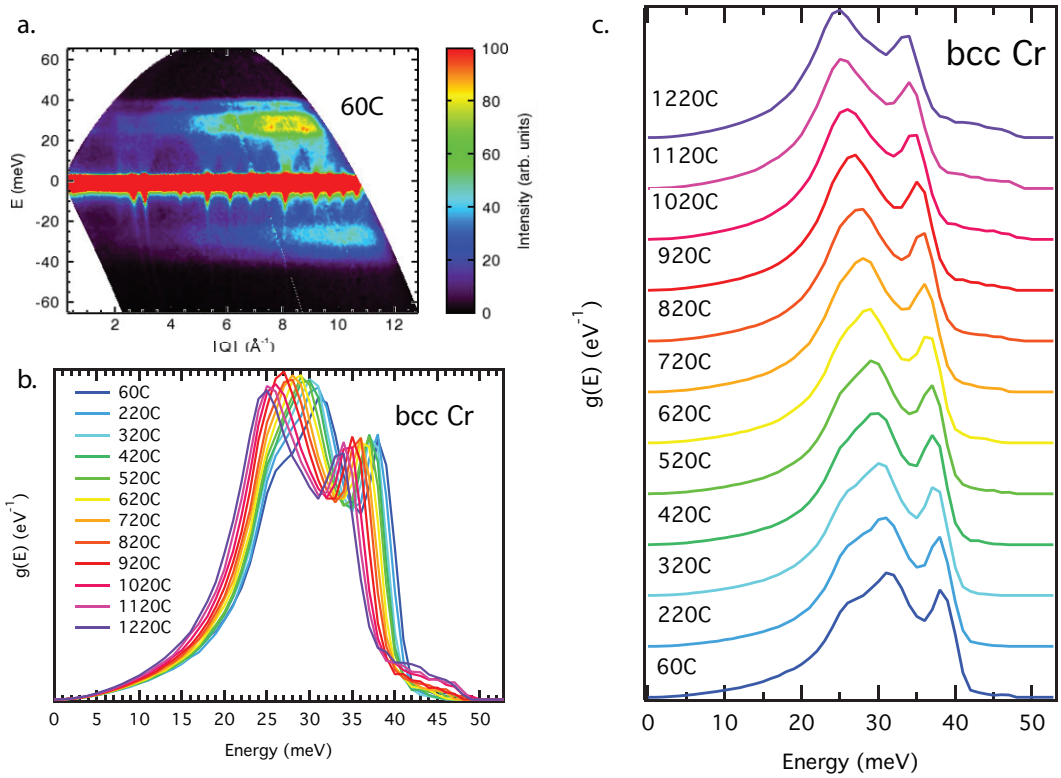

Figure A.11: $\mathbf{S}(\mathbf{Q},\mathbf{E})$ of chromium measured in the MICAS furnace at 60°C (a), and reduced to a density of states for all the measured temperatures (b) and (c). Data was reduced over a full range of $\mathbf{Q}$, and standard reduction procedures used to extract a single-phonon density of states.

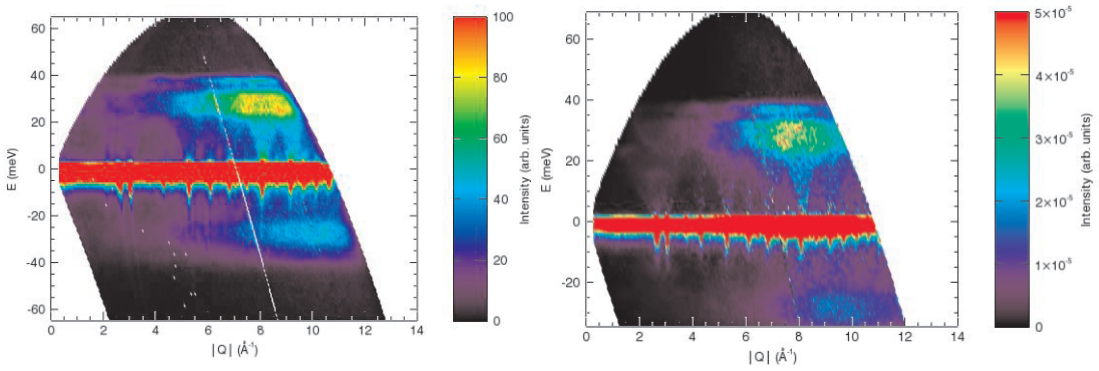

Figure A.12: Chromium measured in the MICAS furnace at 60°C (left) and simulated using the furnace template (right).

not entirely flat, but slightly warped to have overall thickness curvature of ∼4.5 mm. The sample was measured in 100 K increments between room temperature and 1500 K. Figure A.11(b,c) shows the data reduced to a single-phonon DOS for the full range of temperatures. An interesting feature noticeable after reduction to the DOS is the persistence of intensity after the phonon cutoff, near 40-45 meV. The standard correction procedures for data reduction should have eliminated this feature, which is most likely multi-phonon scattering.

The sample assembly constructed for the furnace simulation consisted of the furnace template, with all heat shields in place, and the chromium powder sample modeled as a plate with dimensions 4.1 cm by 2.9 cm and 2.2 mm thick, and placed at 45 degrees to the incident beam. Additional components, such as the BN frame or Nb sachet were not included in the simulation.

Figure A.12 compares the experiment (left) and simulation (right) at 60°C. The most notable features in the experimental data are the strong elastic intensity and Bragg peaks, because chromium is a good coherent scatterer, and the two intensity bands in the inelastic scattering at ∼E=32 and ∼E=38. Additionally, there is a sharp drop in intensity at the highest **Q**, which likely results from positioning the sample at 45 degrees to move the dark angle to this position in **Q**.

In the simulated data, all of the scattering kernels are used, and multiple scattering and multiphonon scattering are allowed. There is a variation in **Q**, most likely due to a difference in the angular position of the sample in the experiment and simulation. Positioning of the sample for the

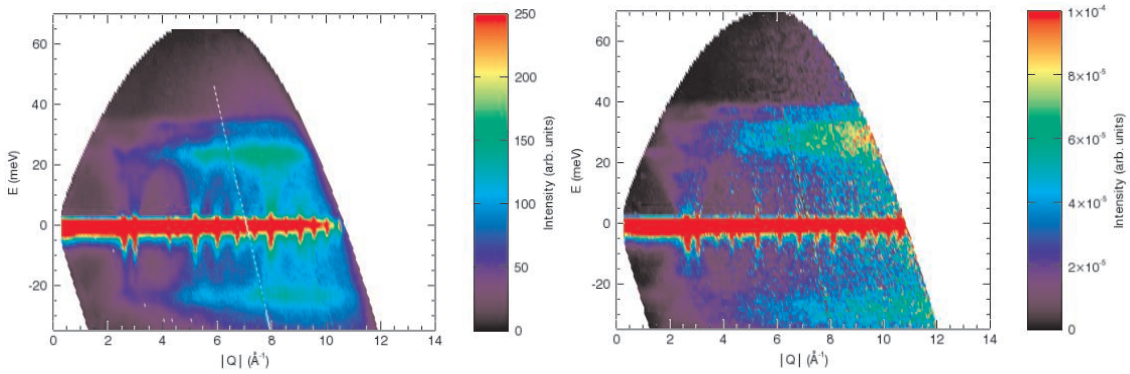

Figure A.13: Chromium measured in the MICAS furnace at 1200°C (left) and simulated using the furnace template (right).

experiment is done by estimate of the beam position, but rotation by +/-10-15°C is very possible.

Figure A.13 compares the experiment (left) and simulation (right) at the highest measured temperature. The conditions for the experiment and simulation are identical to the low temperature measurements. For the simulation, the entire sample assembly, including all components of the sample and the furnace template, are elevated in temperature to 1220°C. The experimental data again shows strong Bragg diffraction near E=0, and two intensity bands in the inelastic scattering now shifted considerably with temperature to ∼E=25 and ∼E=34. Strong dispersions are visible, and the drop in intensity at high **Q** appears more dramatic.

The simulated data at high Q has less agreement with the experimental data for this high temperature case. The dispersions appear to be captured with reasonable agreement, as well as the Bragg scattering. However, the variation in **Q** observed at low temperature appears more pronounced, which is difficult to interpret because the angle of the sample between room temperature and high temperature likely did not change. In addition, the position of the peaks in the inelastic data do not match in the high temperature experimental and simulated data. This is simply explained because a room temperature BVK model was used. Additional discrepancies may result because in the simulation, all of the components of the sample assembly are assumed to be at the same elevated temperature, including the sample, heat shields, and outer vacuum container. In the experiment, this is not likely the case. The purpose of the heat shielding is to prevent the outer vacuum container

from reaching elevated temperatures, thus there is likely a decrease in temperature as a function of distance from the sample for each component. It is possible to introduce a temperature distribution into the simulation, though this is reasonably complex.

Chromium serves as an interesting case study for testing the furnace template over its full range of operating temperatures. The simulations show reasonable agreement at room temperature, and less good agreement at high temperature. There are several possible sources for this disagreement. Work in this direction should continue, as the merit of using MCViNE simulations as an additional tool to understand experimental data has been well-established.

Appendix B

Differential Scanning Calorimetry Measurement Guide

B.1 Introduction

Differential scanning calorimetry (DSC) is a widely used thermal analysis technique defined by the ASTM as one in which a physical property of a material is measured as a function of temperature while the material is subjected to a controlled temperature program [130]. DSC measures the amount of energy absorbed or released by a sample when it is heated or cooled, providing information about exothermic and endothermic transitions in a material. The most common measurements made with DSC include: melting temperature and heat of fusion of metals, phase formation temperature and exothermal energies of intermetallic phase formation, transition temperature and heat of transformation of structural or magnetic transitions in metals, and glass transition temperatures in amorphous materials.

DSC measures the energy necessary to maintain a zero temperature difference between the material being studied and a reference material as a function of time or temperature. Raising the temperature of the material at a constant rate gives the amount of heat per unit mass required to raise the temperature, which is the definition of the specific heat capacity, C_p. DSC is used to refer to two types of calorimeters that obtain similar information with several important differences. These two instruments are heat flow calorimeters and heat flux calorimeters. This appendix will provide a brief overview to both techniques, but is intended to provide a practical introduction to

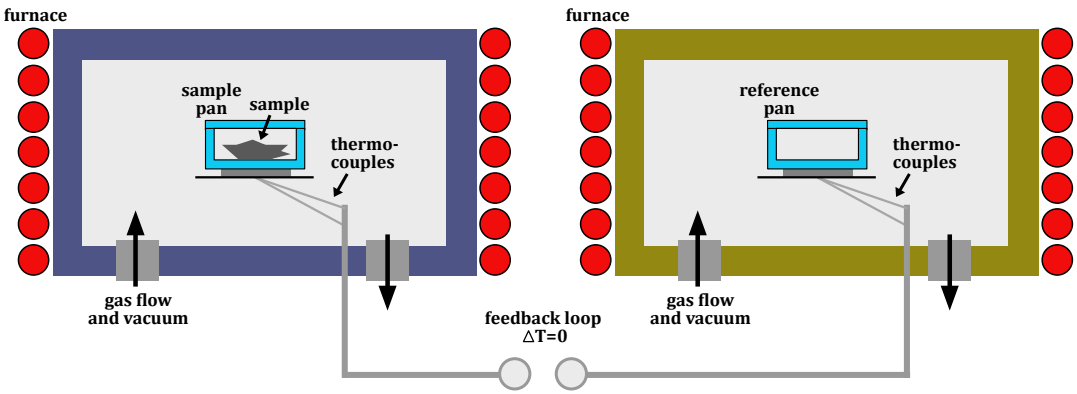

Figure B.1: Schematic of a heat flow calorimeter. Sample and reference pans are contained inside two separate but identical heating elements. Temperature is measured in each furnace by a thermocouple below the pans. Ports for gas flow in and out of the chamber are shown schematically, but not positioned relative to the sample pans as drawn. The temperature difference between the sample and reference pans is maintained at zero by varying the power input to the two furnaces.

DSC measurements using a heat flux calorimeter. Both dynamic heating and step calorimetry experiments can be performed with a heat flux DSC. Dynamic heating experiments are highly routine and discussed only briefly. The primary emphasis is placed on using a heat flux calorimeter to obtain quantitative heat capacity measurements using step calorimetry.

A brief notational comment: The heat capacity of a substance is the amount of heat required to changes its temperature by one degree. It is an extensive property that is typically in units of J/K. The specific heat capacity is the quantity being measured with calorimetry. The specific heat capacity is an intensive property that is the heat capacity per unit mass. This quantity is in units of J/g-K. The specific heat capacity is measured at constant volume or constant pressure, giving rise to the subscript p for constant pressure or v for constant volume. The heat capacity is correctly written with an uppercase C when the quantity is per mole, and lower case c when its not, though this convention is widely misused. The discussion here pertains to calorimetry measurements of the specific heat capacity at constant pressure, which will be written as C_p, and reported in units of J/g-atom·K. This quantity will be referred to (incorrectly) as the heat capacity.

B.1.1 Heat Flow Calorimeters

Heat flow calorimeters are also called power-compensation calorimeters, and are considered the 'real DSC.' This approach uses a double-furnace, power controlled technique to measure heat flow. Two furnaces, one containing a sample and the other a reference, are coupled with a feedback loop. The instrument maintains the sample at a set temperature while measuring the power needed to do this against the reference furnace. Because these systems are power controlled, they are able to maintain temperature precisely without drift and heat and cool rapidly without overshoot or undershoot. This direct measurement of heat flow usually gives highly accurate specific heat and enthalpy measurements.

Figure B.2 shows a schematic of the two furnace design of heat flow calorimeters. The temperature in each furnace is measured underneath the sample and reference pans and the two furnaces are thermally isolated from each other and controlled independently. When performing the measurement, the temperature difference between the sample and reference pans is maintained at zero by varying the power input to the two furnaces. This provides the most straightforward measurement of heat flow; the difference in the amount of power required to maintain identical temperatures in the sample and reference is exactly the same as the amount of heat being absorbed or released by the sample.

Heat flow calorimeters are available commercially from several sources. The most common are Perkin Elmer and TA Instruments. These can be configured with refrigerated cooling system for measurements down to -120°C or -180°C with liquid nitrogen, and typically have a maximum temperature of 725°C.

B.1.2 Heat Flux Calorimeters

Heat flux calorimeters are more appropriately called differential thermal analyzers (DTA). While the temperature of the sample and reference are kept constant in heat flow calorimeters, in DTA it is the heat flow that is kept constant. The DTA dates back to the 1880s and early work in the ceramics industry in which temperature transitions in materials were studied by placing a thermometer into a

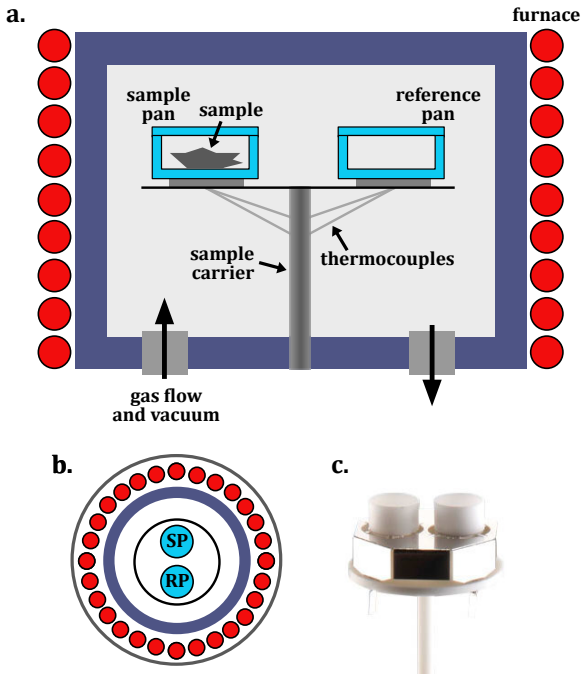

Figure B.2: (a) Schematic of a heat flux calorimeter. Sample and reference pans are both contained inside the same heating element. The pans rest on a sample carrier and thermocouples below the pans measure temperature. Ports for gas flow in and out of the chamber are shown schematically, but not positioned relative to the sample pans as drawn. (b) Top down view of the cylindrical furnace surrounding the sample pan (SP) and reference pan (RP) resting on the sample carrier. (c) Photo of the sample carrier with two alumina pans.

material and heating it in an oven. Comparing the temperature in the oven to the temperature of the thermometer in the sample was a crude estimate of heat capacity. As might be expected, this measurement was subject to poor reproducibility because variables including thermometer placement, oven convection, and sample mass were difficult to control. More modern versions continue to have a single furnace design and measure heat flux by quantifying the temperature difference and changes between a sample and a reference. Typically, heat flux DSCs are less sensitive to small transitions because they heat and cool at slower rates than heat flow DSCs, and thus give less accurate values for heat capacity and enthalpy. However, heat flux calorimeters are capable of measurements to higher temperatures than heat flow calorimeters.

Figure B.2 (a) shows a schematic of the single furnace design of heat flux calorimeters. Sample and reference pans are both contained inside the same heating element. The pans rest on a sample

carrier and thermocouples below the sample pans measure temperature. Ports for gas flow in and out of the chamber are shown schematically, but not positioned relative to the sample pans as drawn. Figure B.2 (b) gives a top down view of the cylindrical furnace surrounding the sample pan (SP) and reference pan (RP) resting on the sample carrier and (c) is a side view photo of the sample carrier with two alumina pans.

The most common commercial source for heat flux calorimeters is Netzsch. These can be configured with a furnace capable of measurement up to 2000°C. Most instruments are not capable of measurement below room temperature, but special configurations are available to measure to -150°C. Thermogravimetric Analysis (TGA) is another type of thermal analysis that uses the heat flux calorimetry technique. TGA provides simultaneous mass analysis by tracking changes in sample mass during heating and cooling. It may be possible to use a TGA when a DSC is not available, though the sample pan configuration and sample requirements differ slightly.

B.2 Heat Flux Calorimetry

B.2.1 Dynamic Calorimetry

In dynamic heating experiments, the sample is continuously heated or cooled with a constant heating or cooling rate, and the amount of energy absorbed during an endothermal event or released during an exothermal event is measured. This is the most common type of calorimetry, also called scanning calorimetry, and is useful for identifying the onset temperatures of glass transitions, phase transitions, melting, etc. During continuous heating, the sample is not at equilibrium and the measured onset temperature will vary as a function of the heating rate. The amount of heat absorbed or released during endothermic or exothermic transitions can provide quantitative information about the enthalpy and entropy of the transition.

Figure B.3 shows the typical results of a dynamic heating experiment. Before the sample is measured, the signal of the empty sample is measured, generating the correction signal (orange). Then the measurement is repeated with the sample (green). The differential signal (black) is obtained

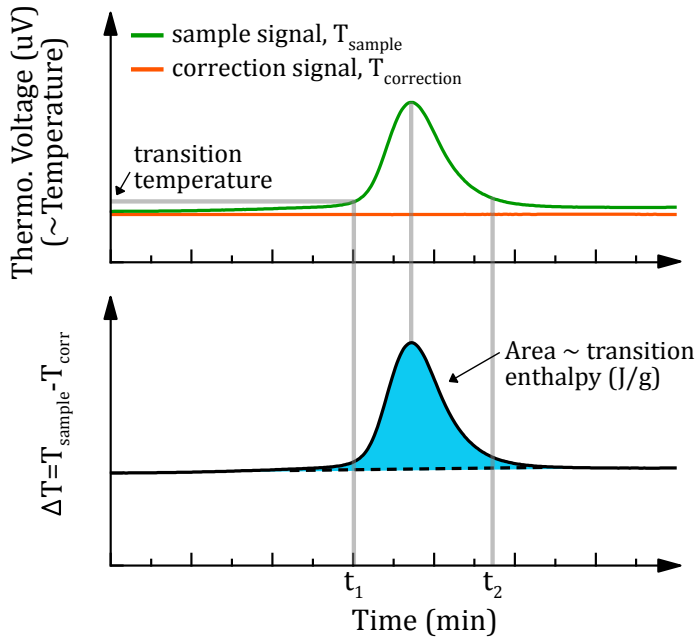

Figure B.3: Dynamic calorimetry in a heat flux calorimeter requires measurement of the sample (green) and measurement of the empty sample pans (orange). The differential signal (black) is obtained by subtracting the correction signal from the sample signal. The peak area (blue) is correlated with the heat content (enthalpy) of the transition in units of J/g.

by subtracting the correction signal from the sample signal. The peak area (blue) is correlated with the heat content (enthalpy) of the transition in units of J/g.

An example for amorphous $Cu_{50}Zr_{50}$ heated at 20 K/min is shown in Fig. B.4. The small endothermal peak around 690 K corresponds to the onset of the glass transition. This is followed by the sharp exothermic peak of crystallization in which heat is released from the sample. A phase transition to the B2 phase occurs at 990 K as indicated by the endothermal peak from an absorption of heat by the sample. Finally the sample melts at 1170 K producing two endothermal peaks.

To determine the heat released or absorbed during a phase transition, crystallization, or melting, the peak area can be determined. This integrated value corresponds to the enthalpy of the transition. The entropy can be obtained by dividing by the onset temperature of the transition. For the $Cu_{50}Zr_{50}$ sample in Fig. B.4, the entropy of formation of the B2 phase (T_{B2}) is 2.9 J/mol-K and the entropy of fusion of the B2 phase is 7.0 J/mol-K (T_s).

Dynamic calorimetry experiments cannot be used to perform accurate measurements of heat

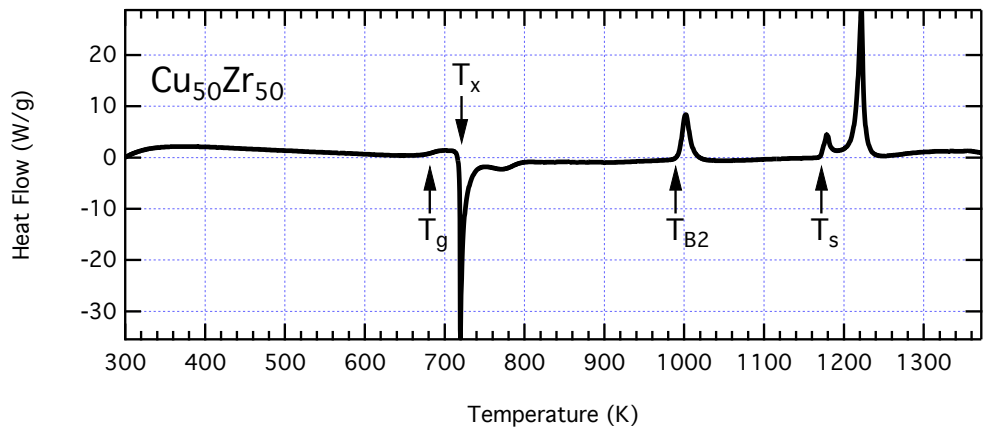

Figure B.4: Differential scanning calorimetry of amorphous $Cu_{50}Zr_{50}$ at a heating rate of 20K per min. The glass transition is characterized by an endothermic rise in heat capacity, followed by the sharp exothermic peak of crystallization. The glass transition and crystallization temperatures, T_g and T_x, are indicated by arrows. The temperatures of the endothermal B2 phase transition and melting , T_{B2} and T_s, are also indicated by arrows.

capacity. Simply converting y-axis units of W/g to J/g for a continuous heating scan is incorrect for determining the heat capacity at a given temperature. This can be demonstrated by measuring a standard sample during a continuous heating experiment and comparing the result to published heat capacity values. Figure B.5 provides an example of single crystal sapphire measured at a heating rate of 5 K/min between 25°-1100°C. Each colored curve represents a unique experiment, performed using standard procedures for dynamic heating experiments. The black curve is the standard values for the heat capacity of sapphire, plotted with error bars to represent ± 10% of the standard value. The terrible agreement with standard heat capacity values for sapphire show conclusively that dynamic calorimetry does not provide reliable values for specific heat capacity at a given temperature.

B.2.2 Step Calorimetry

Isothermal calorimetry or step calorimetry experiments are performed by heating the sample at a constant rate to a given temperature, and holding the sample isothermally for a given amount of time to allow the sample to come to equilibrium. This results in a step of heat flux dQ/dt from the combination of the ramp and isothermal hold. Heat capacity is the amount of heat per unit mass

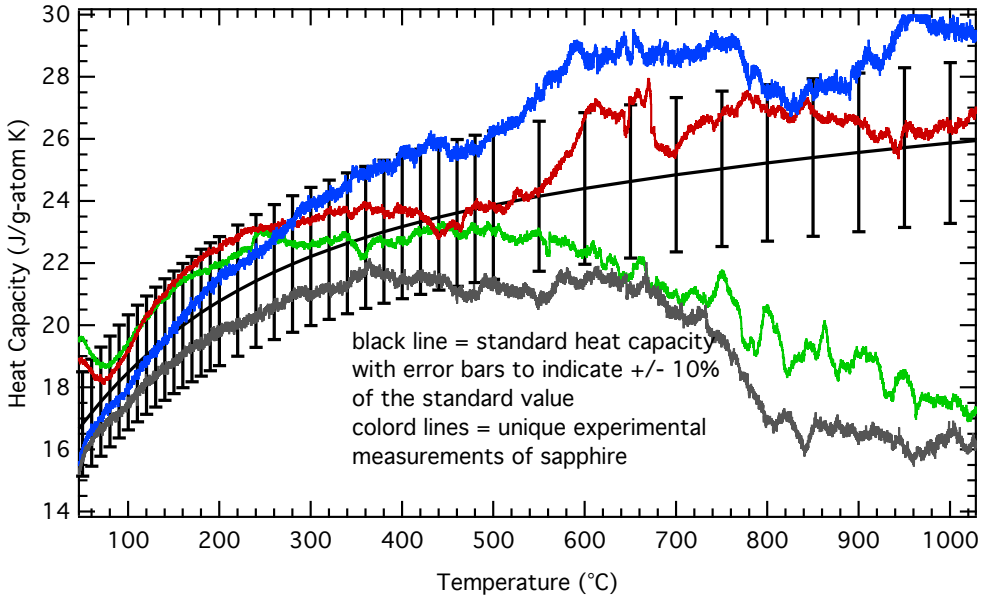

Figure B.5: Measurement of single crystal sapphire during continuous heating at 5 K/min between 25°-1100°C demonstrates that dynamics calorimetry gives terrible results for specific heat capacity. Each colored curve represents a unique experiment, performed using standard procedures for dynamic heating experiments. The black curve is the standard values for the heat capacity of sapphire, plotted with error bars to represent ± 10% of the standard value.

required to raise the temperature. Thus the heat flux resulting from the step in temperature can be related to the heat capacity. This type of calorimetry can be used for quantitative measurement of the heat capacity at a given temperature. However, its execution will vary based on whether a heat flux or heat flow calorimeter is used.

Heat capacity is obtained at a given temperature T by measuring the heat flow dQ for a step in temperature ΔT followed by an isothermal hold at that temperature over the time t:

$$\frac{dQ}{dt} = \left(\frac{dQ}{dt}\right)_{\Delta T \neq 0} - \left(\frac{dQ}{dt}\right)_{\Delta T = 0} = c \cdot \frac{dT}{dt}. \tag{B.1}$$

The first term when $\Delta T \neq 0$ is the power necessary to raise temperature of the sample and container ΔT and hold it at that temperature. The second term when $\Delta T = 0$ is the power required to maintain the sample and container at that temperature. Subtraction of the second term from the

first term, which is subtraction of the power required for the isothermal hold, gives the heat capacity c of the entire system.

The difficulty in solving Equation B.1 is in obtaining an accurate measurement of dQ/dt. This is done by measuring the heat flux of the sample relative to a sapphire standard of known heat capacity. Note that measurements with dynamic calorimetry are also performed against a sapphire standard; the 'sensitivity' calibration uses a sapphire measurement to establish the conversion from measured voltage to units of heat flow under the continuous heating conditions. The same is done for step calorimetry according to the following expression:

$$c_p(T)_{\text{sample}} = \frac{\left(\frac{dQ}{dt}\right)_{\text{sample}}}{\left(\frac{dQ}{dt}\right)_{\text{sapphire}}} \cdot \frac{m_{\text{sapphire}} \cdot \mu_{\text{sample}}}{m_{\text{sample}} \cdot \mu_{\text{sapphire}}} \cdot c_p(T)_{\text{sapphire}} \tag{B.2}$$

where m is the mass of the sample, μ is the molar mass, and $c_p(T)_{\text{sapphire}}$ is the specific heat capacity of sapphire at the temperature T. Implementation of equation B.2 experimentally differs whether a heat flux or heat flow calorimeter is used. The remainder of this appendix will pertain to measurements using a heat flux calorimeter. Examples of specific heat capacity measurements performed using a heat flow calorimeter can be found in the papers of Ralf Busch [73, 74, 131, 132]. Busch et al. have measured and reported the heat capacity of many metallic glasses using step calorimetry. His papers are a valuable resource for information about step calorimetry, in particular the 1998 paper on MgCuY metallic glasses [73].

An example of a step calorimetry measurement of a metallic glass through the glass transition and crystallization is shown in Fig. B.6. The left axis, temperature, indicates that the sample was heated continuously to 200°C, held at 200°C for 20 minutes, then heated with repeated steps of 10°C at 10 K/min followed by a 1 min isothermal hold. The right axis, heat flow, gives the measured heat flow from the sample. The bottom plot in Fig. B.6 shows a smaller region spanning five steps. During each constant increase in temperature, heat flow increases. During the isothermal hold, the heat flow relaxes. At higher temperatures, the heat flow appears to relax exponentially, reaching

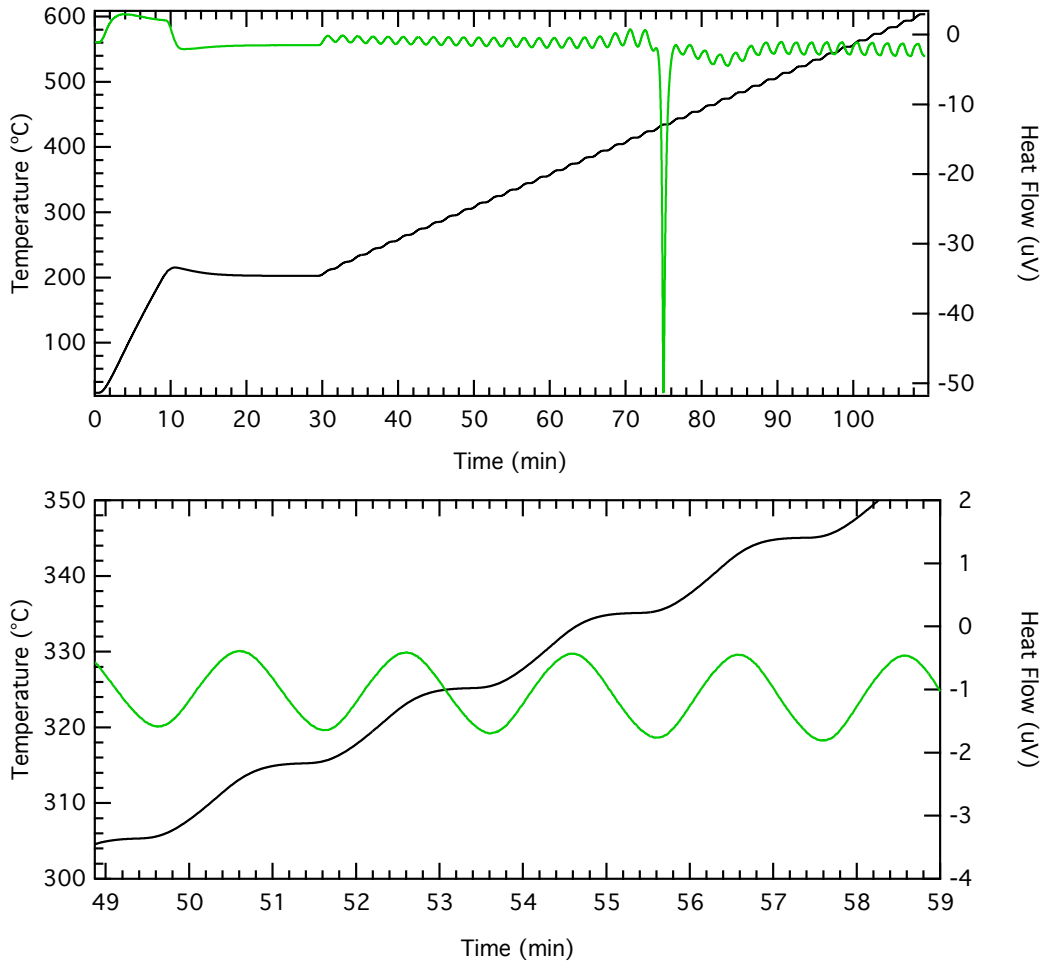

Figure B.6: Step calorimetry measurement of an amorphous sample through the glass transition and crystallization (top). The left axis, temperature, indicates that the sample was heated continuously to 200°C, held at 200°C for 20 minutes, then heated with repeated steps of 10°C at 10 K/min followed by a 1 min isothermal hold. The right axis, heat flow, gives the measured heat flow from the sample. The bottom plot shows a smaller region spanning five steps. During each constant increase in temperature, heat flow increases and during the isothermal hold, the heat flow relaxes.

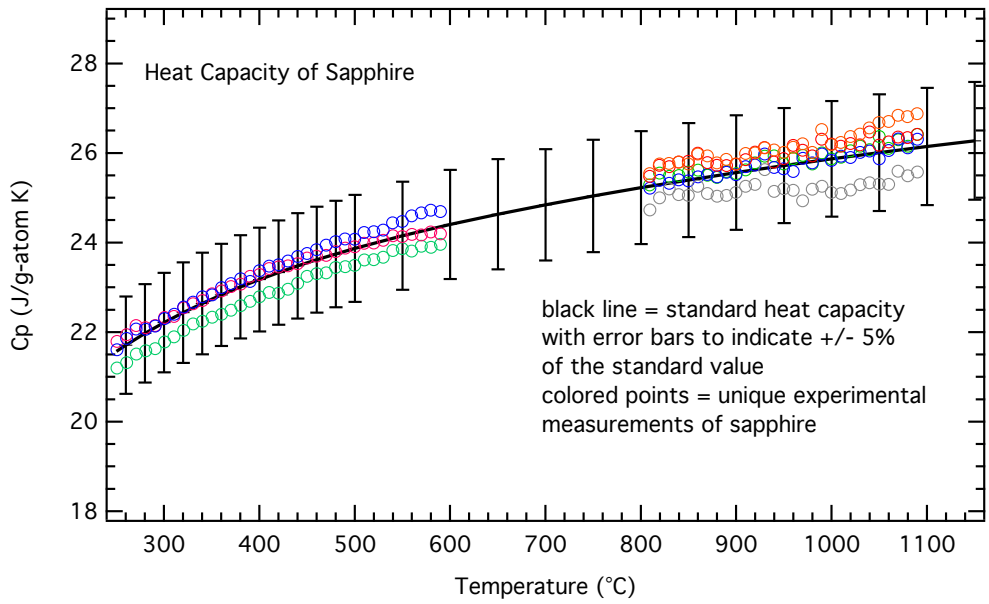

Figure B.7: Heat capacity of sapphire measured with step calorimetery over two temperature ranges, 250°-600°C and 800°-1100°C. Each set of colored circles represents a unique measurement. All of these data agree within ± 5% of the black curve, the standard values of heat capacity.

a plateau inside time period of the one-minute isothermal hold. A longer isothermal hold time at lower temperatures may allow the sample more time to relax, but this difference in heat flow is likely within the error of our measurement conditions.

In contrast to Figure B.5 which shows poor agreement of the heat capacity of sapphire obtained with scanning calorimetry, the heat capacity of sapphire obtained with step calorimetry is accurate to within ± 5% of standard values, as shown in Figure B.7. The data in Figure B.7 were obtained over two temperature ranges, 250°-600°C and 800°-1100°C, and each set of colored circles represents a unique measurement. All of these data agree within ± 5% of the black curve, the standard values of specific heat capacity of sapphire.

B.2.2.1 Background Correction

In dynamic heat capacity measurements, the heat absorbed/released from the sample is separated from the heat absorbed/released by the sample pan by performing an empty measurement or correction of the empty sample pan. The correction provides the heat flow from the sample and reference

pans under identical experimental conditions when no sample is present. This correction is then subtracted from the sample measurement in units of raw heat flow (voltage) before further data processing.

In step calorimetry, it is not necessary to perform a correction measurement. Figure B.8 shows the heat flow for a step calorimetry experiment as a function of (a) time and (b) temperature. Each plot gives an inset over a smaller range in x-axis units. During each temperature step, a maximum in heat flow occurs several seconds after the end of the constant heating, and a minimum in heat flow occurs several seconds at the end of the isothermal hold. The lag of several seconds is not important – it may result from the latent heat of the sample or from a delayed response of the furnace to the software instruction. The difference between this maximum and subsequent minimum directly corresponds to the flux in heat dQ during the step. The change in time dt and the change in temperature dT is determined from difference in the time and temperature at the maximum and minimum of the heat flow. Fig. B.8 (c) identifies the maxima and minima in heat from this step calorimetry experiment which will be used to extract dQ/dt.

B.2.2.2 Mass Condition

Repeated measurement of the sample sample with different masses will result in different values for C_p. An example is shown in Fig. B.9 for seven samples of amorphous $Cu_{50}Zr_{50}$ with varying mass and geometry. On closer inspection, it is obvious that C_p depends systematically on sample mass, with the less massive sample giving a higher value of C_p and the most massive sample giving the lowest C_p. This trend of Cp and sample mass can be seen more clearly in Fig. B.10. For the same sample of amorphous $Cu_{50}Zr_{50}$, the C_p is selected at a temperature between 370°-376°C. The heat capacity C_p and the product of m·C_p are plotted on the left and right y-axes as a function of the sample mass, resulting in a roughly linear increase in C_p with decreasing sample mass.

The specific heat capacity, C_p, that is being measured is the heat capacity per unit mass of material. However, this observation of a mass dependence indicates that there is an optimal sample mass at which the true value of C_p is determined. This is found to be valid when the product of the

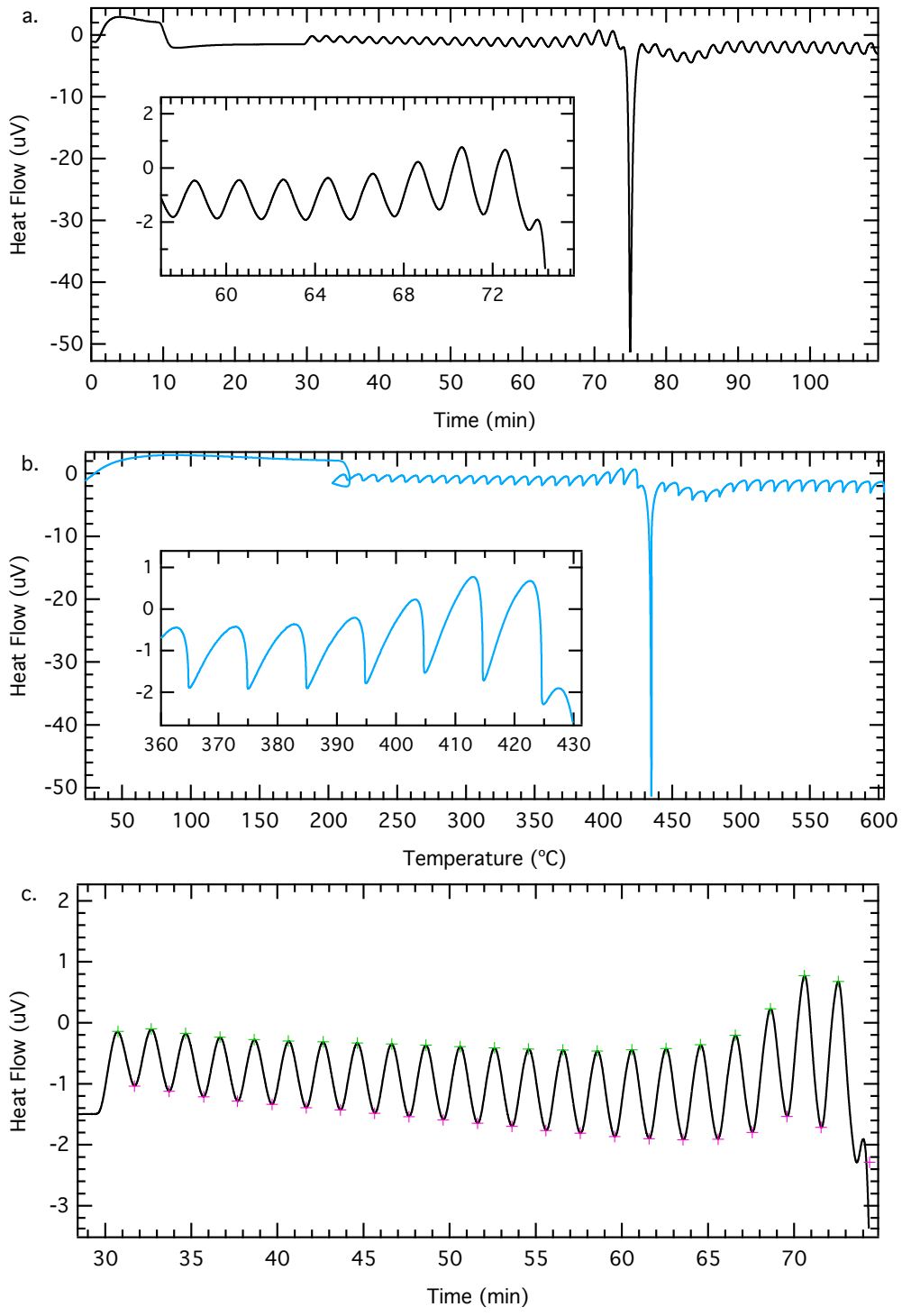

Figure B.8: Heat flow for a step calorimetry experiment as a function of (a) time and (b) temperature. Each plot gives an inset over a smaller range in x-axis units. During each temperature step, a maximum in heat flow occurs several seconds after the end of the constant heating, and a minimum in heat flow occurs several seconds at the end of the isothermal hold. The maxima and minima in heat flow are identified in (c) and each pair will result in a value of dQ/dt at the equilibrium (minimum) temperature.

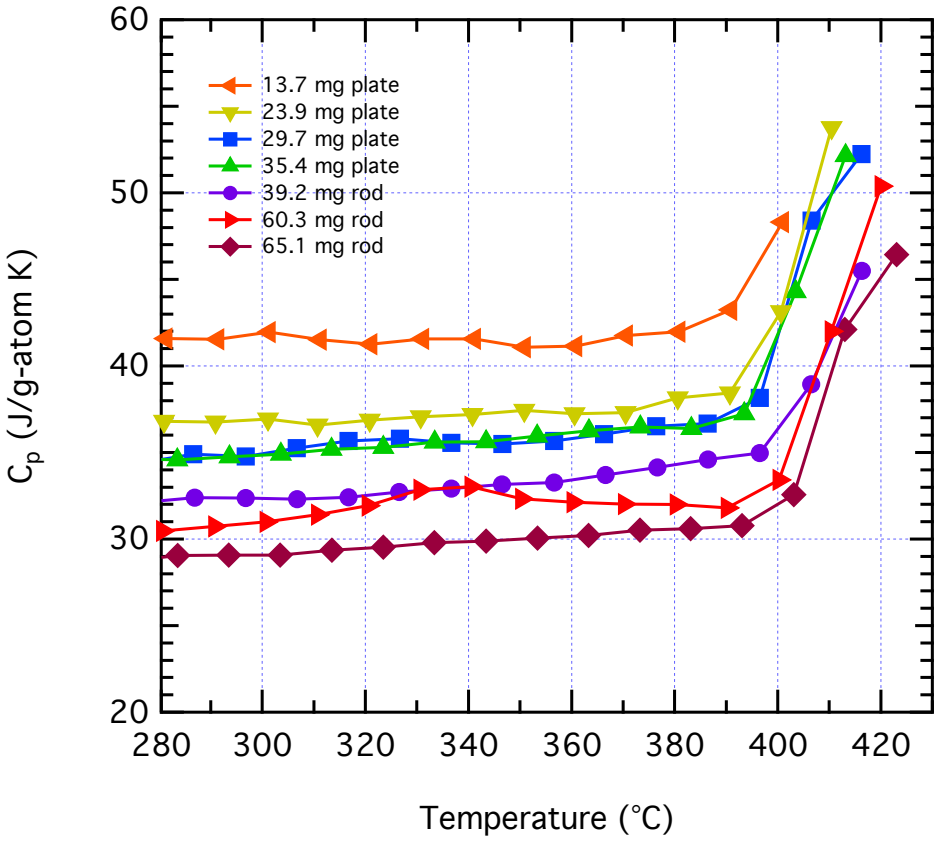

Figure B.9: Repeated measurement of the same amorphous $Cu_{50}Zr_{50}$ with step calorimetery yields different values for C_p. Each colored curve represent a different sample with its mass and geometry indicated on the plot.

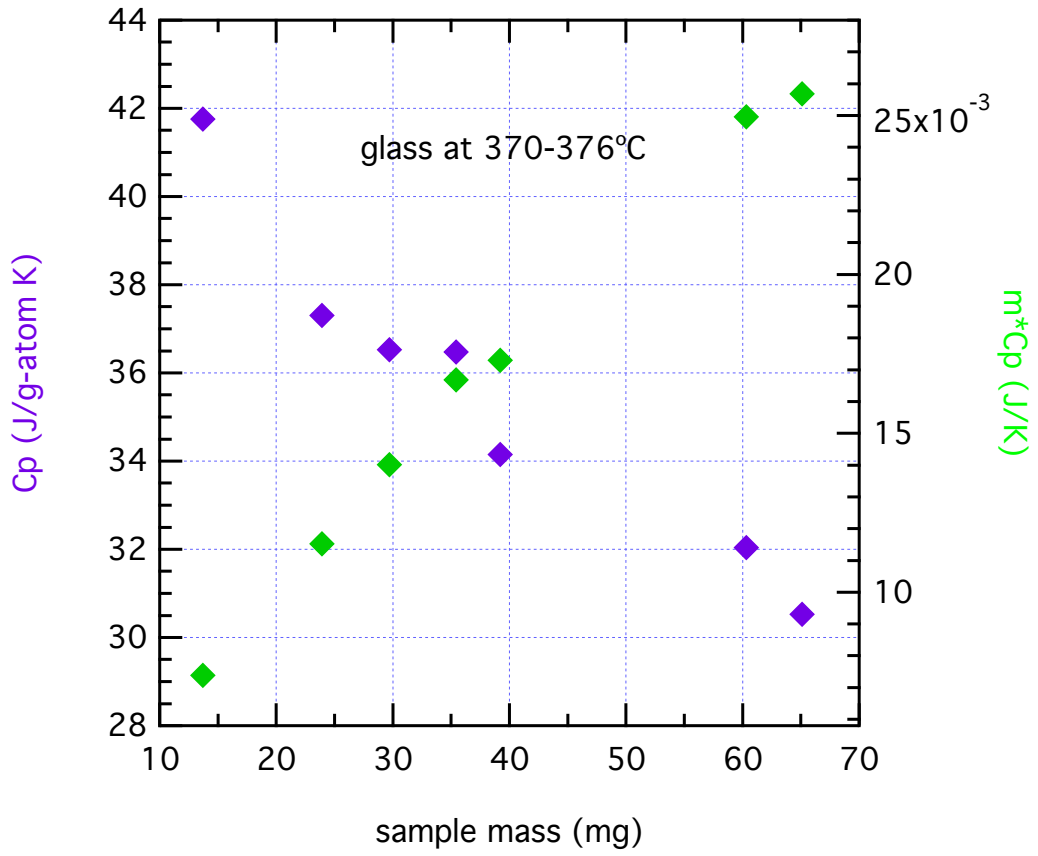

Figure B.10: For a sample of amorphous $Cu_{50}Zr_{50}$ measured with step calorimetry, the measured C_p is selected at a temperature between 370°-376°C. This value of C_p and the product of m·C_p are plotted on the left and right y-axes as a function of the sample mass, resulting in a roughly linear increase in C_p with decreasing sample mass.

sample mass m and its specific heat equals that of the calibration standard, in this case sapphire:

$$m_{\text{sample}} \cdot c_p(T)_{\text{sample}} = m_{\text{sapphire}} \cdot c_p(T)_{\text{sapphire}}. \tag{B.3}$$

The necessity of this relationship from an experimental standpoint is justified as follows. The thermocouples in contact with the sample pan and reference pan only sense the total heat capacity of the sample pan. When measuring the sapphire standard, the measured temperature of the pan (in uV) is calibrated to the power of the system (in mW) for the total heat capacity of that particular sapphire crystal. For a sample with the same total heat capacity as the sapphire crystal, this conversion will be valid. If the total heat capacities of the sapphire standard and the sample are different, then the calibration factor derived from the sapphire standard cannot accurately compensate for the system's response to the measured temperature of the sample.

B.3 Performing Measurements

The key factors in obtaining high quality heat capacity measurements are measurement repeatability, a highly routine sequence of actions, and careful calibration.

Measure repeatability is the most important factor in obtaining quality heat capacity measurements. This requires close monitoring of many (sometimes trivial) variables that have been observed to adversely effect measurement repeatability. Some of these variables inside the calorimeter include gas flow rate, precise positioning of the sample and reference pans and lids on the sample carrier, and the amount of contact between the sample and pan. Outside the calorimeter, the measurement may be influenced by changes in temperature and airflow in the room and by vibrations in the building or on the table where the instrument sits. Attention to all of these details will yield the best quality results.

B.3.1 Calibration

Acquiring and maintaining a set of high quality instrument calibrations is central to all data analysis. Poor calibration can influence entire data sets, even if the instrument appears to be performing correctly. The are three types of calibrations to be performed. These are (1) instrument calibration, (2) temperature calibration, and (3) sensitivity calibration.

Instrument calibration is performed on an empty calorimeter (no sample or reference pans) under gas flow. This calibration is used to test and correct for system bias related to the relative position of the sample carrier inside the furnace. While continuously heating the empty calorimeter, the DSC signal as a function of temperature should remain constant. If this baseline drifts more than 0.2 μV, the correction knobs should be used to adjust the slope of the signal to be zero. Note that ideally the magnitude of the signal should also be zero, indicating that the net heat flow is zero. However, if this value is non-zero but constant, it will be corrected for in the background correction performed for each sample measurement. Instrument calibration is a 'universal' calibration that, when performed over the entire accessible temperature range of the instrument, should remain constant for several weeks or months. It is independent of the sample pan, type of measurement (continuous heating or isothermal heating), heating rate, or temperature range.

Measured temperature values are related to the electromagnetic field generated at the thermocouples under the sample pans. Standard calibration charts are used by the software to convert temperature units, but the calibration can shift with time due to the aging of the thermocouple or other modifications to the system. Calibration of the temperature axis is performed by measuring substances with precisely known melting points. Table B.1 gives the calibration materials and melting points typically used for instrument calibration. Temperature calibrations are typically considered to be universal calibrations, although they are actually heating rate dependent. Where high precision is required (accuracy within $\pm$ 1K), a temperature calibration should be performed with conditions identical to those used in the experiment.

The sensitivity calibration provides the means for conversion of the measured voltage to heat, which varies as a function of temperature. The sensitivity calibration is highly dependent on the

Table B.1: Calibration standards used to perform calibration of the temperature axis [133].

Element	**Melting Point (°C)**
indium	156.6
tin	231.9
bismuth	271.4
zinc	419.5
aluminum	660.3
silver	961.8
gold	1064.2

individual measurement, and in fact must be repeated from each new set of sample pans. The calibration procedure produces a set of values for sensitivity as a function of temperature, so identical measurement conditions (sample pans, heating rate, gas flow, etc.) must be used for the sensitivity calibration measurements and sample measurements. Calibration is done by using a standard material with a well-known heat capacity, typically single-crystal sapphire. The procedure for producing a sensitivity file is as follows:

1. Measure the sapphire crystal using the exact conditions planned for the experiment. For dynamic calorimetry this means performing a correction before measuring the crystal. Repeat the measurement 3-4 times and select the file that appears to represent an 'average.' For step calorimetry measurements, this comparison should be done by reducing the step data to values of delta signal versus temperature.

2. Obtain the standard value of the specific heat capacity of sapphire at each temperature measured experimentally. This can be done by performing a fit to the standard heat capacity data (see Table B.2), then using the analytical function to obtain values of the heat capacity for temperatures in the measured data. An example of an analytic function used to fit the data is:

$$y = (P2 + P3 * z + P4 * z^2 + P5 * z^3) \exp(-z^2) \tag{B.4}$$

where $z = (T - P0)/P1)$, T is temperature and $P0, P1, P2, P3, P4$ and $P5$ are all parameters for the fit. For dynamics calorimetry data, the instrument software has a menu option to fit the measured sapphire data and extract a set of sensitivity values.

3. The sensitivity value at each temperature T is obtained by solving the following equation for every value of T:

$$\text{sensitivity(T)} = \frac{\left(\frac{\text{dQ}}{\text{dt}}\right)_{\text{sample}} - \left(\frac{\text{dQ}}{\text{dt}}\right)_{\text{correction}}}{m_{\text{sapphire}} \times c_p(T)_{\text{sapphire}} \times \text{HR}} \tag{B.5}$$

where the mass of the sapphire crystal is in units of mg, the heat capacity of the sapphire is in units of J/g-K, and the heating rate (HR) is in units of K/s. The measured signal $\left(\frac{dQ}{dt}\right)_{\text{sample}}$ is in units of μV and it must have the signal from the empty pan measurement $\left(\frac{dQ}{dt}\right)_{\text{correction}}$ subtracted. If the correction file was loaded before performing the sapphire measurement, this value will already have been subtracted. The sensitivity value has units of μV/mW.

B.3.2 Dynamic Calorimetry

A dynamic heating experiment is performed by continuously heating or cooling at a constant rate over a given temperature range. An example of a dynamic heating experiment performed at a heating rate of 20 K/min over the temperature range 300 - 1400 K is given in Fig. B.4. To use the dynamic heating curve to accurately determine the enthalpy or entropy formation or fusion, the following procedure should be followed.

The parameters for the measurement should be established first. This means selecting a heating rate and temperature range. Next, ensure that an instrument calibration has been performed recently and determine which files to use for temperature and sensitivity calibration. The temperature calibration file should cover the same temperature range to be used for the experiment, and ideally should be performed at the same heating rate as selected for the experiment. The sensitivity calibration file should also cover the temperature range to be used for the experiment and also must

be performed at the same heating rate and with the same type of sample pans.

With both the sample and reference pans empty, a measurement should be performed under identical experimental conditions, using the temperature and sensitivity files selected for this experiment. This serves as a 'correction' file for the experiment.

The sample is then loaded into the sample pan. Identical measurement conditions are used, and the correction file is identified in the software by first loading the correction file, then selecting the new measurement wizard, and setting the measurement type to 'Sample+Correction.' By identifying this correction file, the software will automatically subtract this file from the measured data. If this step is overlooked, it can be subtracted manually from the data by exporting the measured correction and data files to other software. The resulting measurement can then be converted from units of μV/mW to J/g for accurate determination of peak areas.

Note that it is important to accurately weigh the sample and input this value in the measurement setup. The sample mass is used to convert the y-axis units to J/g. It is also optimal to perform the correction and sample in immediate succession to minimize the environmental factors that influence quality measurements. Using a correction file from several days before the measurement is not likely to be accurate, especially if other measurements were performed in the interim. If all of these steps are followed, the data can be plotted in W/g or J/g as a function of time or temperature, and the integration of peak areas will provide accurate quantitative information.

B.3.3 Step Calorimetry

Step calorimetry experiments are considerably more time consuming than dynamic heating experiments. There are several considerations to be made when planning for these experiments:

- Temperature range: Determine the temperature range over which you wish to obtain quantitative heat capacity measurements. If the temperature range exceeds 300-400 K or is below 600 K, it may be necessary to perform the measurements in two or more smaller temperature ranges. This is because over large temperature ranges and below 600 K, the specific heat capacity of sapphire exhibits larger changes, and satisfying the mass condition will likely require

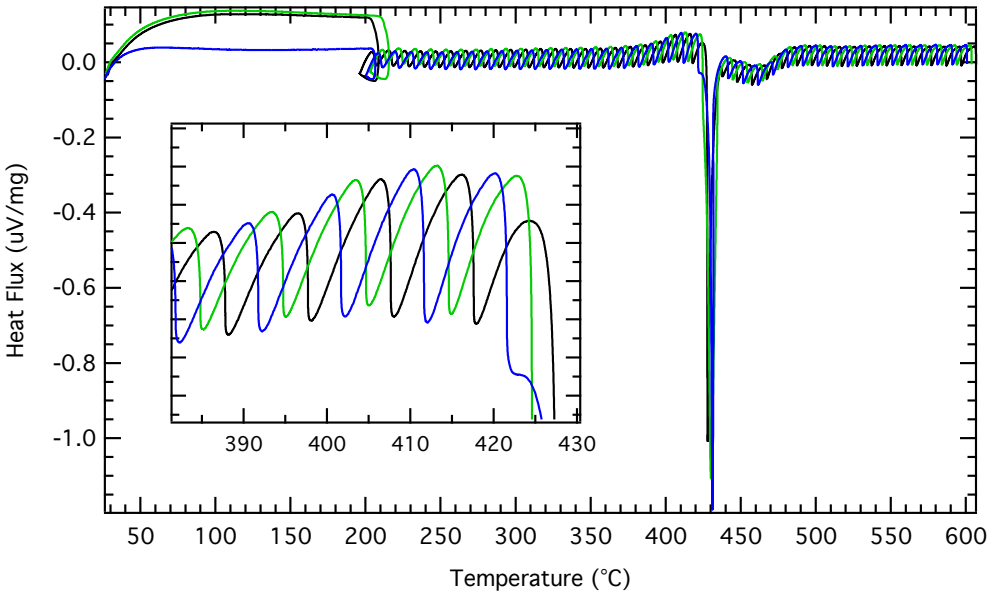

Figure B.11: Step calorimetry measurement performed in steps of 10 K with a one minute isothermal hold produces data points every 10 K. To obtain data in smaller steps, the same measurement can be performed three times with different isothermal hold temperatures. Each colored curve represents a unique measurement.

two samples with different masses. Likewise, a large change in specific heat capacity of the sample (such as in the supercooled liquid of a glass) will require multiple samples to determine the heat capacity in the glass and the supercooled liquid.

- Temperature step size: Determine how many data points are necessary. Typically steps are performed every 10 K, but other step sizes could be selected. The Netzsch software sets limitations for the number of procedural steps allowed, the length of the step, and the heating rate over a given temperature range. Not all combinations of step size and heating rate will be possible. This can usually be overcome by combining data sets from multiple measurements with different isothermal temperature values. Figure B.11 gives an example of three step calorimetry measurements performed in steps of 10 K with a one minute isothermal hold at different temperatures. By repeating this measurement three times, data points are then acquired every 3 K.

- Effective heating rate: The effective heating rate is calculated from the step in temperature

divided by the total time for the step, which includes the time for the temperature increase and time for the isothermal hold. As seen in Fig. B.6, the sample heat flow relaxes during the isothermal hold period. It is important that the isothermal hold time be long enough to allow the sample to relax to equilibrium. A larger temperature step will require a longer isothermal hold.

- Sample pan: Quantitative heat capacity measurements should be performed in a platinum pan and lid because platinum has superior thermal conductivity to alumina. To avoid the possibility of reaction between the sample and platinum pan, an alumina liner can be used that fits completely inside the platinum pan and lid. It was observed that using two lids, both an alumina and platinum lid, resulted in poor reproducibility, so a single platinum lid is advised.

- Samples: Because of the mass condition discussed in Section B.2.2.2, it will most likely be necessary to perform multiple measurements varying the mass of the sample before the correct measurement conditions are determined. If sample is in short supply, it may be useful to estimate the heat capacity from literature reports of similar materials, and use this value to estimate the mass necessary to meet the experimental requirements.

- Calibrations: Instrument and temperature calibrations should be completed prior to beginning measurements. These calibrations will be used throughout for all subsequent measurements. The procedure for the sensitivity calibration will described below. This must be repeated each time a new sample pan is used.

After selecting the temperature range and temperature step size, the measurement protocol can be built in the software. The sensitivity calibration is performed next using the established measurement protocol. This is done by placing the reference sapphire crystal in the sample pan. Note that when setting up the measurement, a temperature calibration file should be selected, but the sensitivity calibration field should be left blank. All measurements should be configured as sample only. A correction file (resulting from a measurement of an empty pan) is never used for

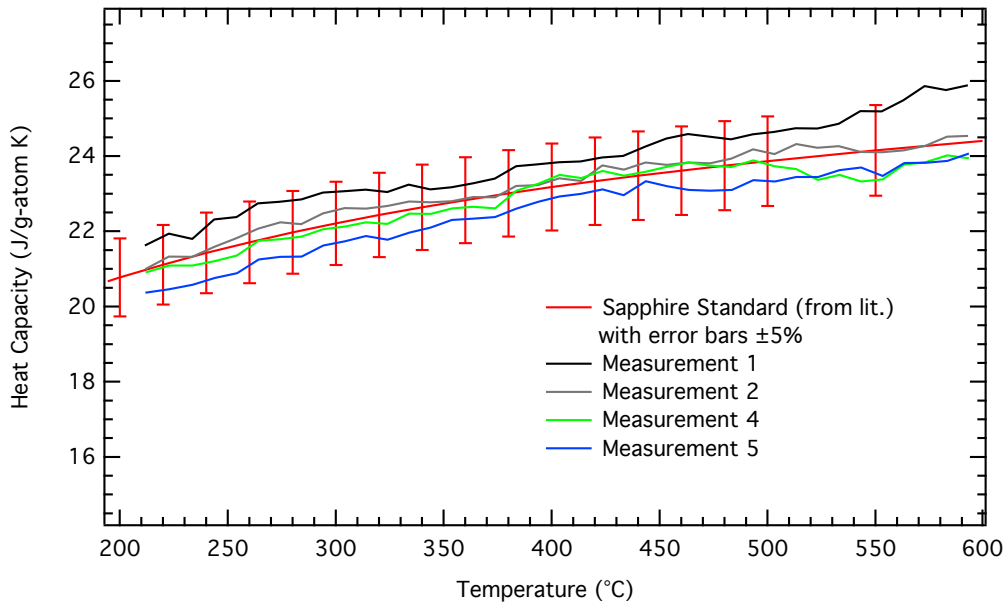

Figure B.12: Measurement of the sapphire crystal over a temperature range of 208 and 598°C. The sapphire standard, shown in red with error bars indicating ± 5%, is plotted with four unique measurements of a sapphire crystal. All four measurements agree within the error bars.

step calorimetry. The measurement of the sapphire crystal should be repeated 3-4 times to ensure that the measured values agree within ± 5%. Figure B.12 gives an example of the measurement of a sapphire crystal over a temperature range of 208 and 598°C. The sapphire standard, shown in red with error bars indicating ± 5%, is plotted with four unique measurements of a sapphire crystal. All four measurements agree within the error bars. Comparison of the sapphire crystal measurements should be performed after reduction of the data from heat flow to delta heat flow values. The procedure for this reduction process is described in Section B.4.

Finally, the sample can be measured. It is critical that the sample is measured using the same sample pans and measurement conditions used for the sensitivity calibration. The sample is placed in the sample pan and the measurement protocol selected. Note that the sensitivity calibration will be introduced when post-processing the data, so the sensitivity calibration field should be left blank for the sample measurement. The resulting file is then reduced to delta heat flow values (see Section B.4). If the measured values meet the mass condition, then the measurement is complete. If the measured values fail this condition, then the sample measurement must be repeated for a

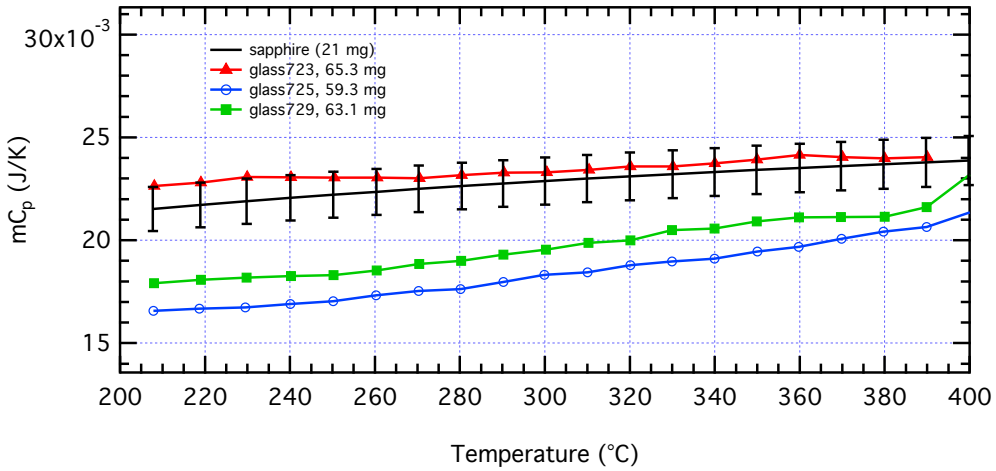

Figure B.13: The m·C_p for three measurements of the same sample, each with different masses, is plotted with the m·C_p of the sapphire standard. The only valid measurement is the curve labeled 'glass723' (red) because it meets the mass condition for agreement with the sapphire standard within ± 5%.

different sample mass. The same sample pan and sensitivity calibration can be used as long as the sample pan remains in pristine condition. However, if the sample pan is not able to be reused, as is sometimes the case in measurements of the melting temperature, then a new pan must be used and the sensitivity calibration performed again.

Figure B.13 shows an example of the same amorphous sample measured three times, each time with a different sample mass as indicated in the plot legend. The resulting data was reduced to C_p and the quantity m·C_p is plotted as a function of temperature. Also plotted is the m·C_p of the sapphire crystal used for the sensitivity measurement (black curve) with error bars representing ± 5%. For these three data sets, the only measurement that meets the mass condition (see Section B.2.2.2) is the measurement labeled 'glass723' with the 65.3 mg sample (red) because its m·C_p agrees with the m·C_p of the sapphire.

B.4 Data Reduction and Analysis for Step Calorimetry

Data collection results in measurements of heat flow as a function of time, similar to what is shown in Fig. B.8 (a) and (b). The first step in data reduction is identifying the minima and is done in

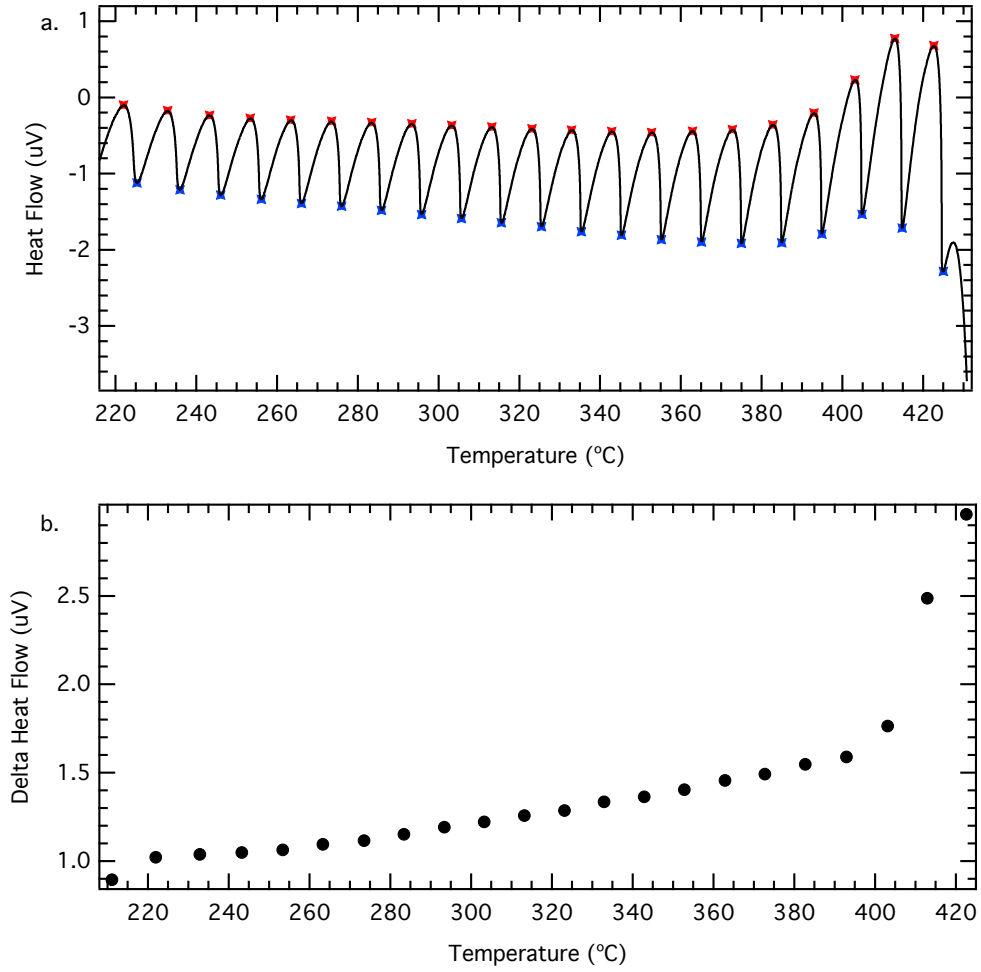

Figure B.14: (a) The heat flow from a step calorimetry experiment is plotted as a function of temperature. The first step in data reduction is identifying the maxima and minima, which are marked here with colored symbols. The value for dQ for each step is then determined by

Fig. B.8 (c) and Fig. B.14 (a). Each maximum and the subsequent minimum represents one step dQ/dt at the equilibrium temperature (at the minimum heat flow value). The change in heat flow (labeled delta heat flow) for the data in Fig. B.14 (a) is plotted in (b).

The values of delta heat flow, dQ/dt extracted from the sample measurement can then be converted to heat capacity by using Equation B.2. The measured delta heat flow value provides the $\left(\frac{dQ}{dt}\right)_{\text{sample}}$ and the initial sensitivity calibration provides $\left(\frac{dQ}{dt}\right)_{\text{sapphire}}$. An approach that more closely mimics the data reduction for dynamic heating data is to determine instrument sensitivity using the sapphire standard. In that case, Equation B.2 reduces to:

$$c_p(T)_{sample} = \frac{\left(\frac{dQ}{dt}\right)_{\text{sample}}}{\text{sensitivity}(T)} \cdot \frac{\mu_{\text{sample}}}{m_{\text{sample}} \cdot HR}. \tag{B.6}$$

where the heating rate (HR) is in units of K/s and the sensitivity is in units of μV/mW. The expression for the sensitivity is given in Equation B.5 for continuous heating. Since step calorimetry does not require an empty pan measurement, the equation becomes simply:

$$\text{sensitivity}(T) = \frac{\left(\frac{dQ}{dt}\right)_{\text{sample}}}{m_{\text{sapphire}} \times c_p(T)_{\text{sapphire}} \times \text{HR}} \tag{B.7}$$

where the mass of the sapphire crystal is in units of mg, the heat capacity of the sapphire is in units of J/g-K, and the heating rate (HR) is in units of K/s. The measured signal $\left(\frac{dQ}{dt}\right)_{\text{sample}}$ is in units of μV. This results in a sensitivity value with units of μV/mW.

Typically, heat capacity values are reported in J/mol-K, which may be more accurately labeled as J/g-atom·K. To obtain units of J/g-K, which is used in Equation B.6, the typical value in J/mol·K should be divided by molar mass of sapphire, μ_{sapphire}:

$$c_p(T)_{\text{sapphire}}\left[\frac{\text{J}}{\text{g} \cdot \text{K}}\right] = \frac{c_p(T)_{\text{sapphire}}\left[\frac{\text{J}}{\text{mol} \cdot \text{K}}\right]}{\mu_{\text{sapphire}}} \tag{B.8}$$

where $\mu_{\text{sapphire}} = 101.96/5$, which is the atomic mass of sapphire (Al_2O_3) divided by the number of gram-atoms.

To solve Equation B.6 for the heat capacity of the sample at temeprature T in units of J/g-atom·K, input $\left(\frac{dQ}{dt}\right)_{\text{sample}}$ in units of μV, sample mass m_{sample} in mg, the heating rate (HR) in K/s, and the sensitivity at T in μV/mW. The molar mass of the sample μ_{sample} is calculated from the molecular weight in g/mol, divided by the number of gram-atoms.

A Mathematica notebook is available with the thesis download that provides support for data analysis. The inputs necessary for this notebook are:

- standard specific heat capacity of sapphire in J/g-K and temperature (°C)
- sapphire measurement data reduced to delta heat flow as a function of temperature by extracting the difference between the maximum and minimum heat flow in each step (max value minus next min value) at the temperature of the minimum
- sample measurement data also reduced to delta heat flow and temperature (°C)

The Mathematica notebook fits the standard specific heat capacity of sapphire to Eq. B.4, then uses the function to extract specific heat capacity values for the temperatures at which the sapphire measurement was performed. Next, these standard values are used along with the measured sapphire data to generate sensitivity values using Eq. B.7. Finally, the sample measurement is inputted and Eq. B.6 is used to obtain the specific heat capacity of the sample. The m·C_p of the sample is then plotted with m·C_p of the sapphire standard to check if the measurement satisfies Eq. B.3. The C_p and m·C_p of the sample are exported for further processing and plotting.

Table B.2: Sapphire Specific Heat Capacity Literature Values [134]

Temperature (°C)	Temperature (K)	C_p (J/g-K)	C_p (J/g-atom·K)
-200	73	0.051643546	1.05304288
-150	123	0.208694328	4.25540256
-100	173	0.40332769	8.2240936
-50	223	0.57839971	11.79391712
0	273	0.71794929	14.6394168
20	293	0.764202466	15.5825468
40	313	0.805705315	16.4288148
60	333	0.842967873	17.18862072
80	353	0.876450172	17.87134488
100	373	0.90652	18.48448671
110	383	0.92045	18.76852777
120	393	0.93368	19.03829541
130	403	0.94625	19.29460525
140	413	0.95821	19.53847683
150	423	0.96958	19.77031795
160	433	0.9804	19.99094424
170	443	0.99071	20.20117133
180	453	1.00054	20.40161092
190	463	1.00991	20.59267085
200	473	1.01884	20.7747589
220	493	1.03553	21.11507802
240	513	1.05077	21.42583076
260	533	1.06473	21.71048354
280	553	1.07756	21.97209494
300	573	1.08936	22.21270402
320	593	1.10027	22.43516546
340	613	1.11036	22.64090662
360	633	1.11974	22.83217044
380	653	1.12847	23.01018038
400	673	1.13662	23.17636377
420	693	1.14425	23.33194405
440	713	1.15143	23.47834856
460	733	1.15818	23.61598511
480	753	1.16457	23.74628104
500	773	1.17061	23.86944027
550	823	1.18447	24.15205398
600	873	1.19687	24.40489742
650	923	1.20812	24.63429167
700	973	1.21846	24.84513048
750	1023	1.22808	25.04128805
800	1073	1.2371	25.22521126
850	1123	1.2456	25.39853136
900	1173	1.25367	25.5630835
950	1223	1.26134	25.7194794
1000	1273	1.26863	25.86812688
1050	1323	1.27558	26.00984155
1100	1373	1.28218	26.14441951
1150	1423	1.28845	26.27226857
1200	1473	1.29439	26.39338873

Bibliography

[1] R Pynn. Neutron Scattering- A Primer. *Los Alamos Science*, 19:1–32, August 1990.

[2] Chen Li. *Phonon Anharmonicity of Ionic Compounds and Metals.* PhD thesis, California Institute of Technology, May 2012.

[3] B Fultz. *Inelastic Scattering Guide.* Springer, New York, July 2012.

[4] Hongjin Tan. *A Study of the Thermodynamics and Kinetics of Li_xFePO_4 as a Cathode Material for Li Batteries* . PhD thesis, California Institute of Technology, 2012.

[5] Wolfgang Sturhahn. Nuclear resonant spectroscopy. *J Phys-Condens Mat*, 16(5):S497–S530, January 2004.

[6] M S Lucas, L Mauger, J A Munoz, I Halevy, J Horwath, S L Semiatin, S O Leontsev, M B Stone, D L Abernathy, Yuming Xiao, Paul Chow, and B Fultz. Phonon densities of states of face-centered-cubic Ni-Fe alloys. *Journal of Applied Physics*, 113(17):17A308, 2013.

[7] G Shen, W Sturhahn, E E Alph, J Zhao, T S Tollenner, V B Prakapenka, Y Meng, and H R Mao. Phonon density of states in iron at high pressures and high temperatures. *Physics and Chemistry of Minerals*, 31(6), July 2004.

[8] G L Squires. *Introduction to the theory of thermal neutron scattering.* Dover Publications, New York, May 1978.

[9] The 1994 Nobel Prize in Physics, http://www.nobelprize.org/nobelprizes/physics/laureates/1994/press.html.

[10] Neutron scattering lengths and cross sections, http://www.ncnr.nist.gov/resources/n-lengths/.

[11] M Kresch. *Temperature Dependence of Phonons in Elemental Cubic Metals Studied by Inelastic Scattering of Neutrons and X-Rays*. PhD thesis, California Institute of Technology, December 2008.

[12] JYY Lin, A A Aczel, D L Abernathy, and S E Nagler. Using Monte Carlo ray tracing simulations to model the quantum harmonic oscillator modes observed in uranium nitride. *Phys Rev B*, 2014.

[13] B Fultz. Mossbauer Spectrometry. In Elton Kaufmann, editor, *Characterization of Materials*. John Wiley, New York, October 2011.

[14] Dominic P E Dickson and Frank J Berry, editors. *Mossbauer Spectroscopy*. Cambridge Univ Press, Great Britain, April 1986.

[15] K S Singwi and A Sjolander. Resonance absorption of nuclear gamma rays and the dynamics of atomic motions. *Phys Rev*, 120(4):1093, 1960.

[16] William M Visscher. Study of lattice vibrations by resonance absorption of nuclear gamma rays. *Annals of Physics*, 9(2):194–210, 1960.

[17] R Röhlsberger. *Nuclear Condensed Matter Physics with Synchrotron Radiation*. Springer, Hamburg, June 2008.

[18] M Seto, Y Yoda, S Kikuta, X Zhang, and M Ando. Observation of Nuclear Resonant Scattering Accompanied by Phonon Excitation Using Synchrotron Radiation. *Phys Rev Lett*, 74(19):3828–3831, May 1995.

[19] W Sturhahn, TS Toellner, EE Alp, X Zhang, M Ando, Y Yoda, S Kikuta, M Seto, CW Kimball, and B Dabrowski. Phonon density of states measured by inelastic nuclear resonant scattering. *Phys Rev Lett*, 74(19):3832–3835, 1995.

[20] A I Chumakov, R Rüffer, H Grünsteudel, H F Grünsteudel, G Grübel, J Metge, O Leupold, and H A Goodwin. Energy dependence of nuclear recoil measured with incoherent nuclear scattering of synchrotron radiation. *EPL (Europhysics Letters)*, 30(7):427, 1995.

[21] EE Alp, W Sturhahn, TS Toellner, J Zhao, M Hu, and DE Brown. Vibrational dynamics studies by nuclear resonant inelastic x-ray scattering. *Hyperfine Interact*, 144(1):3–20, 2002.

[22] EE Alp, W Sturhahn, and TS Toellner. Lattice dynamics and inelastic nuclear resonant x-ray scattering. *Hyperfine Interact*, 135(1):295–310, 2001.

[23] W Sturhahn. CONUSS and PHOENIX: Evaluation of nuclear resonant scattering data. *Hyperfine Interact*, 125(1-4):149–172, 2000.

[24] D W Johnson and J C H Spence. Determination of the single-scattering probability distribution from plural-scattering data. *Journal of Physics D: Applied Physics*, 7(6):771, 1974.

[25] B Fultz. Vibrational thermodynamics of materials. *Prog Mater Sci*, 55(4):247–352, 2010.

[26] Y Tsunoda, Y Kurimoto, M Seto, S Kitao, and Y Yoda. Phonon density of states of γ-Fe precipitates in Cu. *Phys Rev B*, 66(21):214304, 2002.

[27] W Damgaard Kristensen, EJ Jensen, and RMJ Cotterill. Thermodynamics of small clusters of atoms: A molecular dynamics simulation. *Journal of Chemical Physics*, 60(11):4161–4169, 1974.

[28] A Tamura, K Higeta, and T Ichinokawa. Lattice-vibrations and specific-heat of a small particle. *J. Phys. C*, 15(24):4975–4991, 1982.

[29] A Tamura, K Higeta, and T Ichinokawa. The size dependence of vibrational eigenfrequencies and the mean-square vibrational displacement of a small particle. *J. Phys. C*, 16(9):1585–1592, 1983.

[30] B Fultz, CC Ahn, EE Alp, W Sturhahn, and TS Toellner. Phonons in nanocrystalline Fe-57. *Phys Rev Lett*, 79(5):937–940, 1997.

[31] AB Papandrew, AF Yue, B Fultz, I Halevy, W Sturhahn, TS Toellner, EE Alp, and HK Mao. Vibrational modes in nanocrystalline iron under high pressure. *Phys Rev B*, 69(14):144301, 2004.

[32] HN Frase, B Fultz, and JL Robertson. Phonons in nanocrystalline Ni3Fe. *Phys Rev B*, 57(2):898–905, 1998.

[33] E Bonetti, L Pasquini, E Sampaolesi, A Deriu, and G Cicognani. Vibrational density of states of nanocrystalline iron and nickel. *Journal of Applied Physics*, 88:4571, 2000.

[34] L Pasquini, A Barla, A I Chumakov, O Leupold, R Rüffer, A Deriu, and E Bonetti. Size and oxidation effects on the vibrational properties of nanocrystalline α-Fe. *Phys Rev B*, 66(7):73410, 2002.

[35] Beatriz Roldan Cuenya, JR Croy, LK Ono, A Naitabdi, H Heinrich, W Keune, J Zhao, W Sturhahn, EE Alp, and M Hu. Phonon density of states of self-assembled isolated Fe-rich Fe-Pt alloy nanoclusters. *Phys Rev B*, 80(12):125412, 2009.

[36] Abdelkader Kara and Talat S Rahman. Vibrational dynamics and thermodynamics of surfaces and nanostructures. *Surface Science Reports*, 56(5):159–187, January 2005.

[37] S Stankov, M Sladecek, T Ślezak, J Lażewski, R Röhlsberger, B Sepiol, G Vogl, AI Chumakov, R Rüffer, and N Spiridis. Phonons in iron monolayers. *Journal of Physics: Conference Series*, 217:012144, 2010.

[38] Beatriz Roldan Cuenya, W Keune, R Peters, E Schuster, B Sahoo, U von Hoersten, W Sturhahn, J Zhao, T S Toellner, E E Alp, and S D Bader. High-energy phonon confinement in nanoscale metallic multilayers. *Phys Rev B*, 77(16):165410, 2008.

[39] Beatriz Roldan Cuenya, A Naitabdi, J Croy, W Sturhahn, JY Zhao, EE Alp, R Meyer, D Sudfeld, E Schuster, and W Keune. Atomic vibrations in iron nanoclusters: Nuclear resonant inelastic x-ray scattering and molecular dynamics simulations. *Phys Rev B*, 76(19):195422, 2007.

[40] S Stankov, M Miglierini, A I Chumakov, and I Sergueev. Vibrational thermodynamics of $Fe_{90}Zr_7B_3$ nanocrystalline alloy from nuclear inelastic scattering. *Phys Rev B*, 2010.

[41] K Suzuki and K Sumiyama. Control of Structure and Formation of Amorphous and Nonequilibrium Crystalline Metals by Mechanical Milling. *Mater T Jim*, 36(2):188–197, 1995.

[42] J Trampenau, K Bauszus, W Petry, and U Herr. Vibrational behaviour of nanocrystalline Ni. *Nanostruct Mater*, 6(5-8):551–554, 1995.

[43] B Fultz, JL Robertson, TA Stephens, LJ Nagel, and S Spooner. Phonon density of states of nanocrystalline Fe prepared by high-energy ball milling. *Journal of Applied Physics*, 79(11):8318–8322, 1996.

[44] U Stuhr, H Wipf, KH Andersen, and H Hahn. Low-frequency modes in nanocrystalline Pd. *Phys Rev Lett*, 81(7):1449–1452, 1998.

[45] R Meyer, LJ Lewis, S Prakash, and P Entel. Vibrational properties of nanoscale materials: From nanoparticles to nanocrystalline materials. *Phys Rev B*, 68(10):104303, 2003.

[46] Paul Derlet, R Meyer, LJ Lewis, U Stuhr, and H Van Swygenhoven. Low-frequency vibrational properties of nanocrystalline materials. *Phys Rev Lett*, 87(20):205501, 2001.

[47] Paul Derlet and H Van Swygenhoven. High-Frequency Vibrational Properties of Metallic Nanocrystalline Grain Boundaries. *Phys Rev Lett*, 92(3):35505, 2004.

[48] B Fultz, L Anthony, LJ Nagel, R M Nicklow, and S Spooner. Phonon Densities of States and Vibrational Entropies of Ordered and Disordered Ni3Al. *Phys Rev B*, 52(5):3315–3321, 1995.

[49] S Stankov, Y Z Yue, M Miglierini, B Sepiol, I Sergueev, A I Chumakov, L Hu, P Svec, and R Rueffer. Vibrational properties of nanograins and interfaces in nanocrystalline materials. *Phys Rev Lett*, 100(23):235503, 2008.

[50] B Roldan Cuenya, L K Ono, J R Croy, K Paredis, A Kara, H Heinrich, J Zhao, E E Alp, A T DelaRiva, A Datye, E A Stach, and W Keune. Size-dependent evolution of the atomic vibrational density of states and thermodynamic properties of isolated Fe nanoparticles. *Phys Rev B*, 86(16):165406, October 2012.

[51] K Thompson, D Lawrence, D J Larson, J D Olson, T F Kelly, and B Gorman. In situ site-specific specimen preparation for atom probe tomography. *Ultramicroscopy*, 107(2-3):131–139, February 2007.

[52] L A Giannuzzi. Reducing FIB Damage Using Low Energy Ions. *Microscopy and Microanalysis*, 12(S02):1260, July 2006.

[53] Jonathan M Hyde and Colin A English. An Analysis of the Structure of Irradiation induced Cu-enriched Clusters in Low and High Nickel Welds. *MRS Proceedings*, 650:R6.6.1–R6.6.12, 2000.

[54] E C Svensson, B N Brockhouse, and J M Rowe. Crystal dynamics of copper. *Phys Rev*, 155(3):619, 1967.

[55] HN Frase, LJ Nagel, JL Robertson, and B Fultz. Vibrational density of states of nanocrystalline Ni_3Fe. *Philos Mag B*, 75(3):335–347, 1997.

[56] S Bein, C Colinet, and M Durand-Charre. CVM calculation of the ternary system Co–Cu–Fe. *Journal of Alloys and Compounds*, 313(1):133–143, 2000.

[57] LB Hong and B Fultz. Two-phase coexistence in Fe-Cu alloys synthesized by ball milling. *Acta Mater*, 46(8):2937–2946, 1998.

[58] HN Frase, B Fultz, and JL Robertson. . *J. Appl. Phys.*, 85:7097, 1999.

[59] HN Frase, B Fultz, JL Robertson, and S Spooner. . *Philos. Mag. B*, 80:1545, 2000.

[60] B Fultz and HN Frase. Grain boundaries of nanocrystalline materials. In RS Mishra, SL Semiatin, C Suryanarayana, NN Thadhani, and TC Lowe, editor, *Ultrafine Grained Materials*, pages 3–12, Warrendale, PA, 2000. Minerals Met & Mat Soc, MPMD Div, TMS.

[61] D Wolf, J Wang, SR Philpot, and H Gleiter. Phonon-Induced Anomalous Specific Heat of a Nanocrystalline Model Material by Computer Simulation. *Phys. Rev. Lett.*, 74:4686, 1995.

[62] T Egami, S Poon, Z Zhang, and V Keppens. Glass transition in metallic glasses: A microscopic model of topological fluctuations in the bonding network. *Phys Rev B*, 76(2):024203, July 2007.

[63] P W Anderson. Through a Glass Lightly. *Science*, 267:1615, March 1995.

[64] C Austen Angell. Formation of glasses from liquids and biopolymers. *Science*, 267(5206):1924–1935, 1995.

[65] Edgar Dutra Zanotto. Do cathedral glasses flow? *Am. J. Phys.*, 66(5):392, 1998.

[66] WL L Johnson, G Kaltenboeck, M D Demetriou, J P Schramm, X Liu, K Samwer, C P Kim, and D C Hofmann. Beating Crystallization in Glass-Forming Metals by Millisecond Heating and Processing. *Science*, 332(6031):828–833, May 2011.

[67] C Austen Angell. Thermodynamic aspects of the glass transition in liquids and plastic crystals. *Pure Appl Chem*, 63(10):1387–1392, 1991.

[68] WL L Johnson, Marios D Demetriou, John S Harmon, Mary L Lind, and Konrad Samwer. Rheology and ultrasonic properties of metallic glass-forming liquids: A potential energy landscape perspective. *MRS Bull.*, 32(08):644–650, 2007.

[69] Srikanth Sastry. Glass-forming liquids and the glass transition: The energy landscape approach to dynamics and thermodynamics. *J. Indian Inst. Sci*, 86:731–749, 2006.

[70] M Shell and Pablo Debenedetti. Thermodynamics and the glass transition in model energy landscapes. *Phys Rev E*, 69(5):051102, May 2004.

[71] Frank H Stillinger. A topographic view of supercooled liquids and glass formation. *Science*, 267(5206):1935–1939, 1995.

[72] Francesco Sciortino. Potential energy landscape description of supercooled liquids and glasses. *Journal of Statistical Mechanics: Theory and Experiment*, 2005(05):P05015, 2005.

[73] R Busch, W Liu, and WL L Johnson. Thermodynamics and kinetics of the MgCuY bulk metallic glass forming liquid. *Journal of Applied Physics*, 83:4134, 1998.

[74] R Busch, Y J Kim, and WL L Johnson. Thermodynamics and kinetics of the undercooled liquid and the glass transition of the ZrTiCuNiBe alloy. *Journal of Applied Physics*, 77:4039, 1995.

[75] Gerold Adam and Julian H Gibbs. On the temperature dependence of cooperative relaxation properties in glassforming liquids. *Journal of Chemical Physics*, 43:139, 1965.

[76] Frans Spaepen and David Turnbull. Metallic glasses. *Annual Review of Physical Chemistry*, 35(1):241–263, 1984.

[77] Pablo G Debenedetti and Frank H Stillinger. Supercooled liquids and the glass transition. *Nature*, 410(6825):259–267, 2001.

[78] R J Highmore and A L Greer. Eutectics and the formation of amorphous alloys. *Nature*, 1989.

[79] Ioannis M Kalogeras and Haley E Hagg Lobland. The Nature of the Glassy State: Structure and Glass Transitions. *Journal of Materials Education*, 34(3):69, 2012.

[80] M D Ediger, C A Angell, and Sidney R Nagel. Supercooled liquids and glasses. *The journal of physical chemistry*, 100(31):13200–13212, 1996.

[81] GF Syrykh, MG Zemlyanov, and SN Ishmaev. Experimental study of partial vibrational spectra in amorphous alloys. *Physica B*, 234:450–451, 1997.

[82] GF Syrykh, SN Ishmaev, MG Zemlyanov, and IL Sashin. Concentration dependence of partial vibrational spectra in Ni-Nb and Cu-Zr metallic glasses. *J Non-Cryst Solids*, 250:642–644, 1999.

[83] JB Suck, H Rudin, HJ Guntherdot, H Beck, J Daubert, and W Glaser. Dynamical structure factor and frequency-distribution of the metallic-glass $Cu_{46}Zr_{54}$ at room-temperature. *J Phys C Solid State*, 13(8):L167–L172, 1980.

[84] D L Abernathy, M B Stone, M J Loguillo, M S Lucas, O Delaire, X Tang, J Y Y Lin, and B Fultz. Design and operation of the wide angular-range chopper spectrometer ARCS at the Spallation Neutron Source. *Rev. Sci. Instrum.*, 83(1):015114, 2012.

[85] E L Gjersing, S Sen, and B G Aitken. Vibrational entropy near glass transition in a chalcogenide glass and supercooled liquid. *J Non-Cryst Solids*, 355(10-12):748–752, May 2009.

[86] W A Phillips, U Buchenau, N Nücker, A-J Dianoux, and W Petry. Dynamics of glassy and liquid selenium. *Phys Rev Lett*, 63(21):2381, 1989.

[87] Martin Goldstein. Statistical Thermodynamics of Configurational Properties. In *The Glass Transition and the Nature of the Glassy State*, pages 68–77. Annals of the New York Academy of Sciences, October 1976.

[88] Martin Goldstein. Viscous liquids and the glass transition. V. Sources of the excess specific heat of the liquid. *J. Chem. Phys.*, 64(11):4767, 1976.

[89] Mary L Lind. *Ultrasonic investigation of the elastic properties and liquid fragility of bulk metallic glasses in the supercooled liquid region.* PhD thesis, California Institute of Technology, October 2007.

[90] Mary Laura Lind, Gang Duan, and WL L Johnson. Isoconfigurational Elastic Constants and Liquid Fragility of a Bulk Metallic Glass Forming Alloy. *Phys Rev Lett*, 97(1):015501, July 2006.

[91] DRCS, http://danse.us/trac/DrChops, October 2010.

[92] M Kresch, M Lucas, O Delaire, J Lin, and B Fultz. Phonons in aluminum at high temperatures studied by inelastic neutron scattering. *Phys Rev B*, 77(2):024301, January 2008.

[93] D C Wallace. *Statistical Physics of Crystals and Liquids.* World Scientific, Singapore, January 2002.

[94] J-M Tarascon and Michel Armand. Issues and challenges facing rechargeable lithium batteries. *Nature*, 414(6861):359–367, 2001.

[95] Xianxiz Yuan, Hansan Liu, and Jiujum Zhang. *Lithium-Ion Batteries: Advanced Materials and Technologies.* Green Chemistry and Chemical Engineering. CRC Press, December 2011.

[96] Jordi Cabana, Laure Monconduit, Dominique Larcher, and M Rosa Palacín. Beyond Intercalation-Based Li-Ion Batteries: The State of the Art and Challenges of Electrode Materials Reacting Through Conversion Reactions. *Adv Mater*, 22(35):E170–E192, August 2010.

[97] Hajime Arai, Shigeto Okada, Yoji Sakurai, and Jun-ichi Yamaki. Cathode performance and voltage estimation of metal trihalides. *J Pow Sou*, 68(2):716–719, 1997.

[98] F Badway, N Pereira, F Cosandey, and GG Amatucci. Carbon-metal fluoride nanocomposites - Structure and electrochemistry of FeF3 : C. *J Electrochem Soc*, 150(9):A1209–A1218, 2003.

[99] F Badway, F Cosandey, N Pereira, and GG Amatucci. Carbon metal fluoride nanocomposites - High-capacity reversible metal fluoride conversion materials as rechargeable positive electrodes for Li batteries. *J Electrochem Soc*, 150(10):A1318–A1327, 2003.

[100] H Li, G Richter, and J Maier. Reversible Formation and Decomposition of LiF Clusters Using Transition Metal Fluorides as Precursors and Their Application in Rechargeable Li Batteries. *Adv Mater*, 15(9):736–739, May 2003.

[101] Manabu Nishijima, Irina D Gocheva, Shigeto Okada, Takayuki Doi, Jun-ichi Yamaki, and Tetsuaki Nishida. Cathode properties of metal trifluorides in Li and Na secondary batteries. *J Pow Sou*, 190(2):558–562, May 2009.

[102] T Li, L Li, YL Cao, XP Ai, and HX Yang. Reversible Three-Electron Redox Behaviors of FeF3 Nanocrystals as High-Capacity Cathode-Active Materials for Li-Ion Batteries. *The Journal of Physical Chemistry C*, 114(7):3190–3195, 2010.

[103] Linsen Li, Fei Meng, and Song Jin. High-Capacity Lithium-Ion Battery Conversion Cathodes Based on Iron Fluoride Nanowires and Insights into the Conversion Mechanism. *Nano Lett.*, 12(11):6030–6037, November 2012.

[104] Naoko Yamakawa, Meng Jiang, and Clare P Grey. Investigation of the Conversion Reaction Mechanisms for Binary Copper(II) Compounds by Solid-State NMR Spectroscopy and X-ray Diffraction. *Chemistry of Materials*, 21(14):3162–3176, July 2009.

[105] Raju Prakash, Ajay Kumar Mishra, Arne Roth, Christian Kübel, Torsten Scherer, Mohammad Ghafari, Horst Hahn, and Maximilian Fichtner. A ferrocene-based carbon–iron lithium fluoride nanocomposite as a stable electrode material in lithium batteries. *J Mater Chem*, 20(10):1871, 2010.

[106] G G Amatucci, N Pereira, F Badway, M Sina, F Cosandey, M Ruotolo, and C Cao. Formation of lithium fluoride/metal nanocomposites for energy storage through solid state reduction of metal fluorides. *Journal of Fluorine Chemistry*, 132(12):1086–1094, December 2011.

[107] Peng Liao, R A Dunlap, and J R Dahn. In Situ Mössbauer Effect Study of Lithium Intercalation in LiFe[sub 2]F[sub 6]. *J Electrochem Soc*, 157(10):A1080, 2010.

[108] Ping Liu, John J Vajo, John S Wang, Wen Li, and Jun Liu. Thermodynamics and Kinetics of the Li/FeF 3Reaction by Electrochemical Analysis. *The Journal of Physical Chemistry C*, 116(10):6467–6473, March 2012.

[109] Robert E Doe, Kristin A Persson, Y Shirley Meng, and Gerbrand Ceder. First-Principles Investigation of the LiFeF Phase Diagram and Equilibrium and Nonequilibrium Conversion Reactions of Iron Fluorides with Lithium. *Chemistry of Materials*, 20(16):5274–5283, August 2008.

[110] Peng Liao, Jing Li, and J R Dahn. Lithium Intercalation in LiFe[sub 2]F[sub 6] and LiMgFeF[sub 6] Disordered Trirutile-Type Phases. *J Electrochem Soc*, 157(3):A355, 2010.

[111] H Guerault, Y Labaye, and JM Grenèche. Recoilless Factors in Nanostructured Iron-Based Powders. *Hyperfine Interact*, 136(1):57–63, 2001.

[112] H Guerault, M Tamine, and J M Greneche. Mössbauer study of nanostructured iron fluoride powders. *J Phys-Condens Mat*, 12(45):9497, 2000.

[113] R F Butler and S K Banerjee. Single-domain grain size limits for metallic iron. *Journal of Geophysical Research*, 80(2):252–259, 1975.

[114] S Mørup. Mössbauer effect in small particles. *Hyperfine Interact*, 60(1):959–973, 1990.

[115] Mingjiong Zhou, Liwei Zhao, Ayuko Kitajou, Shigeto Okada, and Jun-ichi Yamaki. Mechanism on exothermic heat of FeF3 cathode in Li-ion batteries. *J Pow Sou*, 203:103–108, April 2012.

[116] C Austen Angell. Formation of glasses from liquids and biopolymers. *Science*, 267(5206):1924–1935, 1995.

[117] R Busch, J Schroers, and W H Wang. Thermodynamics and kinetics of bulk metallic glass. *MRS Bull.*, 32(08):620–623, 2007.

[118] K J Zeng, M Hamalainen, and H L Lukas. A New Thermodynamic Description of the Cu-Zr System. *J Phase Equilib*, 15:577, May 1994.

[119] M Wakihara and O Yamamoto, editors. *Lithium ion batteries: fundamentals and performance.* Wiley-VCH, New York, May 1998.

[120] J Vetter, P Novák, M R Wagner, C Veit, K C Möller, J O Besenhard, M Winter, M Wohlfahrt-Mehrens, C Vogler, and A Hammouche. Ageing mechanisms in lithium-ion batteries. *J Pow Sou*, 147(1-2):269–281, September 2005.

[121] Anna S Andersson, Beata Kalska, Lennart Häggström, and John O Thomas. Lithium extraction/insertion in LiFePO 4: an X-ray diffraction and Mössbauer spectroscopy study. *Solid State Ionics*, 130(1):41–52, 2000.

[122] JB Goodenough, editor. *Fast Ion Transport in Solids.* North Holland, May 1973.

[123] Neeraj Sharma and Vanessa K Peterson. In situ neutron powder diffraction studies of lithium-ion batteries. *J Solid State Electrochem*, 16(5):1849–1856, October 2011.

[124] Xun-Li Wang, Ke An, Lu Cai, Zhili Feng, Stephen E Nagler, Claus Daniel, Kevin J Rhodes, Alexandru D Stoica, Harley D Skorpenske, and Chengdu Liang. Visualizing the chemistry and structure dynamics in lithium-ion batteries by in-situ neutron diffraction. *Nature Scientific Reports*, 2, 2012.

[125] Lu Cai, Ke An, Zhili Feng, Chengdu Liang, and Stephen J Harris. In-situ observation of inhomogeneous degradation in large format Li-ion cells by neutron diffraction. *J Pow Sou*, 236(c):163–168, August 2013.

[126] Haodong Liu, Christopher R Fell, Ke An, Lu Cai, and Ying Shirley Meng. In-situ neutron diffraction study of the xLi2MnO3*(1-x)LiMo2 (x=0,0.5; M=Ni, Mn, Co) layered oxide compounds during electrochemical cycling. *J Pow Sou*, 240(C):772–778, October 2013.

[127] Naoko Yamakawa, Meng Jiang, Baris Key, and Clare P Grey. Identifying the Local Structures Formed during Lithiation of the Conversion Material, Iron Fluoride, in a Li Ion Battery: A Solid-State NMR, X-ray Diffraction, and Pair Distribution Function Analysis Study. *J Am Chem Soc*, 131(30):10525–10536, 2009.

[128] Jeanette E Owejan, Jon P Owejan, Steven C DeCaluwe, and Joseph A Dura. Solid Electrolyte Interphase in Li-Ion Batteries: Evolving Structures Measured In situ by Neutron Reflectometry. *Chemistry of Materials*, 24(11):2133–2140, June 2012.

[129] J. Y. Y. Lin, M. A. Aivazis, and B. Fultz. MCViNE.

[130] ASTM E474: Standard Method for Evaluation of Temperature Scale for Differential Thermal Analysis, 1980.

[131] Benjamin A Legg, Jan Schroers, and Ralf Busch. Thermodynamics, kinetics, and crystallization of $Pt_{57.3}Cu_{14.6}Ni_{5.3}P_{22.8}$ bulk metallic glass. *Acta Mater*, 55(3):1109–1116, 2007.

[132] S C Glade, R Busch, D S Lee, WL L Johnson, R K Wunderlich, and H J Fecht. Thermodynamics of $Cu_{47}Ti_{34}Zr_{11}Ni_8$, $Zr_{52.5}Cu_{17.9}Ni_{14.6}Al_{10}Ti_5$ and $Zr_{57}Cu_{15.4}Ni_{12.6}Al_{10}Nb_5$ bulk metallic glass forming alloys. *Journal of Applied Physics*, 87(10):7242–7248, 2000.

[133] P J Lindstrom and W G Mallard. *NIST Chemistry WebBook*. NIST Standard Reference Database. Gaithersburg.

[134] D A Ditmars, S Ishihara, S S Chang, G Bernstein, and E D West. Enthalpy and Heat-Capacity Standard Reference Material - Synthetic Sapphire (Alpha-Al_2O_3) from 10 to 2250 K. *Journal of Research of the National Bureau of Standards*, 87(2):159–163, 1982.